Politecnico di Milano

DIPARTIMENTO DI ELETTRONICA, INFORMAZIONE E BIOINGEGNERIA

Doctoral Programme in Information Technology - Telecommunications

Radio-relaying over Optical Fiber for Cloud Radio Access Networks

Doctoral Dissertation of:

Lorenzo Combi

Supervisor:

Prof. Umberto Spagnolini

Tutor:

Prof. Andrea Virgilio Monti Guarnieri

Coordinator of the Doctoral Program:

Prof. Barbara Pernici

Cycle XXXI - November 2015

“ Obstacles don’t have to stop you.
If you run into a wall, don’t turn around and give up.
Figure out how to climb it, go through it, or work around it.”
Michael J. Jordan

Abstract

The focus of this Thesis is on analog signal transport and processing for future mobile radio access networks, and its content can be broadly divided into four macro-areas:

a) proposal and experimental validation of optical pulse width modulation (PWM) for analog fronthaul;

b) analysis of space-frequency multiplexing of fronthaul signals without channel equalization;

c) hybrid beamforming for the mmWave radio access, with analog optical signal processing and transport;

d) signaling to support analog optical signal processing at the remote antennas.

Fig. 1 is meant to provide a graphical summary of these macro-areas, which are introduced in the following.

Starting from the top (Fig. 1a), analog optical PWM is suitable for analog fronthauling as it combines the best features of digital and analog transmission. Indeed, the 2-level waveform involves a relaxation of the linearity requirements, still allowing for an analog signal transport that avoids the bandwidth expansion of digital fronthauling. PWM is experimentally validated for different optical architectures. Besides the conventional optical network layout (that can be summarized in the cascade of a laser, fiber and photodiode and is omitted in Fig. 1), here an innovative architecture is proposed, based on reflection. In this reflective PWM the transmitter (at the remote antennas) is equipped with a modulated reflective semiconductor optical amplifier (RSOA) that receives, modulates and reflects back a continuous waveform (CW) from an optical source located at the receiver (at the centralized baseband unit, BBU). The modulated reflected signal which is the uplink fronthauling is polarization-separated from the CW seeding signal.

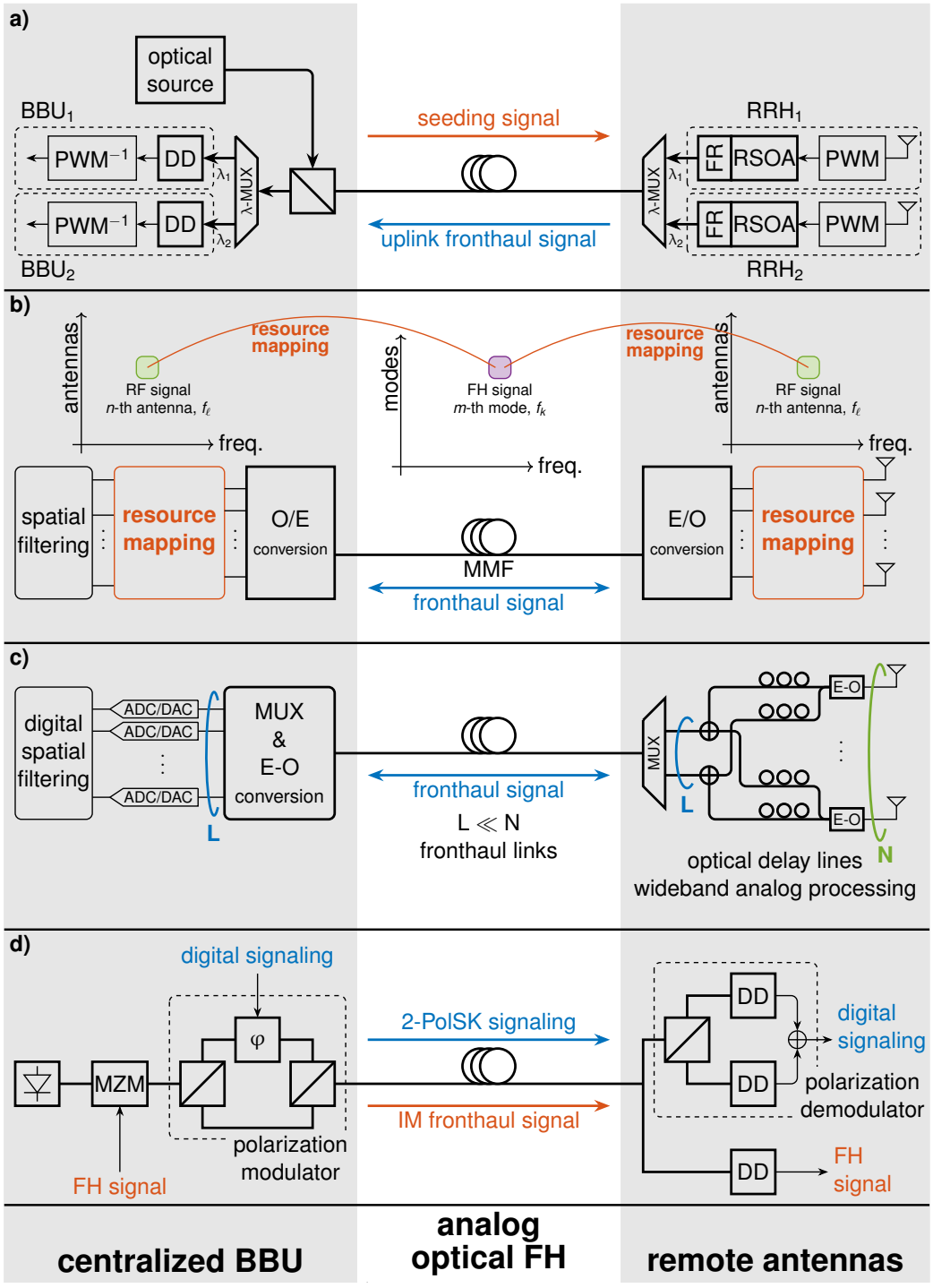

Figure 1: Graphical representation of the aspects related to fronthauling and radio access networks analyzed in the Thesis.

PWM analog fronthauling effectively avoids the bandwidth expansion related to digitization of fronthaul signals in state-of-the-art systems, but massive antenna arrays and larger signal bandwidth may call for additional capacity of the fronthaul link. Mode division multiplexing is considered in this Thesis to provide an additional multiplexing dimension and, to ensure the cost-effectiveness of the proposed solution, modal multiplexing is all-optical and passive. To cope with the arising intermodal interference, the mapping between radio resources and optical fronthauling resources, represented in Fig. 1b, is studied and it is shown that appropriate resource assignment can almost overcome the limitations introduced by intermodal interference. In particular, the resources available on the two channels (wireless link antennas-users and wired fronthaul link) are defined in a space-frequency domain, the space being defined by the antenna array for the radio signal and by the propagation modes for the optical fronthaul.

Massive antenna arrays and larger signal bandwidth are key features of millimeter wave radio communication, and hybrid beamforming has been proved in literature to provide a valid mean to overcome the channel limitations (mainly the increased path loss) while keeping a reasonable hardware complexity and energy consumption. In this Thesis, the integration of hybrid beamforming and analog fronthauling in Fig. 1c is tackled. In particular, realistic analog signal processing techniques in the optical domain are considered in order to provide wideband analog processing via tunable delay lines. Tunability is shown to be essential in dealing with a fast-changing radio environment and with time division multiplexing (TDM) of users, but the speed of typical optical tunable elements in achieving a time-varying delay response is not enough. This causes a transient in system performance with degradation of the first transmitted symbol of the TDM frame. To counteract this effect, this Thesis proposes a technology-aware scheduling of time division multiplexed users, together with a digital precompensation of the transient in delay response.

Tuning the analog processing at the remote antennas requires a signaling channel parallel to the fronthauling. The proposed solution is in Fig. 1d, and it is based on joint A-RoF fronthaul transmission of the radio signals paired with a binary polarization shift keying (PolSK). This provides a low-cost, low-complexity parallel channel between the BBU and the RRH that can be used, e.g., to control the analog beamformer at the RRH and to feed back CSI from the radio channel.

Contents

Chapter 1

Introduction

The evolution towards 5G is revolutionizing the mobile radio access networks, with the aim of reaching extremely high data rates and enforcing diverse stringent requirements depending on the application scenario, such as utmost reliability and extremely low latency. On top of such demanding constraints, operators' profitability needs to be ensured, thus adding an economical requisite to an already complex technical puzzle. These challenging demands motivated the adoption of a centralized radio access network (C-RAN), also known as cloud or cooperative RAN, together with the employment of higher carrier frequencies at the millimeter waves (mmWaves) to take advantage of the huge bandwidth availability in the uncrowded spectrum around 30 and 60 GHz. In this context, the present Thesis concerns optical analog fronthauling for the C-RAN, spatial multiplexing of fronthaul signals, and hybrid beamforming with optical wideband analog processing for the radio access network at the mmWaves, as detailed in the following.

1.1 Towards a Centralized Radio Access Networks: Opportunities and Challenges

C-RAN, first proposed in 2011 [1] and thoroughly described in [2], is based on the split of base stations (BSs) into remote radio heads (RRHs) and baseband units (BBUs), and on the centralization of BBUs in common facilities. Centralization enables cloud computing, i.e., the sharing of physical resources among different BSs, as well as the joint management of the radio environment, e.g., for interference management. Indeed, C-RAN empowers energy efficiency, cost savings on baseband resources and, from the performance point of view, it allows the improvement of network capacity through load balancing and cooperative processing.

The price to be paid for such improvements is an increased stress on the wired fronthaul (FH) connections between the centralized BBUs and the RRHs: apart from niche applications, FH is primarily based on digital transmission of in-phase and quadrature samples of the radio signals according to the Open Base Station Architecture Initiative (OBSAI) [3] or Common Public Radio Interface (CPRI) [4] protocols. Of these protocols, CPRI is the most commonly used by vendors [5], and it is therefore considered in this work as reference for digital fronthauling: in CPRI the radio frequency (RF) signal is harmonically sampled, each sample is digitized with 16-bits resolution, and the digital stream is then passed to a coding stage. Multiplexing of different signals is performed in the time domain. Digital fronthaul results into a bandwidth expansion of the RF signal (e.g., 20-MHz LTE signals in 2x2 MIMO require 2.5 Gbit/s on the digital FH link [6]) primarily related to quantization.

Compression of digital FH signals is a viable manner to alleviate the bandwidth expansion issue: it relies on some digital signal processing (DSP) at the RRHs to achieve a different split of BS functionalities between RRHs and BBUs [7]. The result is a trade-off between required bit rate on the digital fronthauling and complexity at the RRH, and several different functional splits are included in an updated version of the CPRI protocol itself (eCPRI) [8].

Taking to the extremes the concept of functional split towards maximal centralization of the hardware brings to the idea of analog fronthauling: transport of analog signals on the FH link and digital-analog conversion at the centralized BBUs eliminate the obstacle posed by bandwidth expansion.

1.1.1 Analog Radio-over-Fiber

Among the physical communication media employed in fronthauling, optical fiber dominates the scene due to the capability of passive optical networks (PONs) to provide large transmission bandwidths at a reasonable cost. This is the reason why CPRI signals are mostly transported through digital radio-over-fiber (D-RoF), where the binary FH signal modulates the transmitted lightwave, e.g., exploiting intensity modulation / direct detection (IM/DD) for cost-effectiveness. However, the high data rates required by digital FH involve the need for expensive high-speed electronics.

The transmission of analog signals through analog radio-over-fiber (A-RoF) [9], by contrast, enables the use of low-speed components, with acceptable performance also for low cost optical devices. Beside the avoidance of digitization-induced bandwidth expansion, this reflects onto a cost reduction by at least one order of magnitude of the fronthauling link [10].

Nevertheless, A-RoF systems still need to overcome the reluctance of operators and vendors to favor analog communication over the industry standard CPRI, which is mainly due to technical and economical reasons. From the technical viewpoint, the reduced bandwidth requirements and the lower cost of A-RoF come at a price, that price being signal degradation [11] related to an increased impact of propagation issues such as chromatic dispersion, self phase modulation (SPM), stimulated Brillouin scattering (SBS) and limited power budget [12].

1.1.2 Analog Pulse Width Modulation

There is, however, an intermediate class of modulation schemes that combines the best features of digital and analog techniques: pulse time modulation. This modulation family includes pulse frequency modulation (PFM), pulse position modulation (PPM) and pulse width modulation (PWM). Optical PWM was proposed and validated in the 1980s [13,14], and more recently proposed for analog fronthauling [15]. In PWM, information is encoded onto the duration of a sequence of rectangular pulses of fixed amplitude: the result is a two-level waveform (as in D-RoF) carrying analog information (as in A-RoF).

The frequency spectrum of a pulse width modulated signal fundamentally consists in a number of replica of the spectrum of the modulating signal, located at the harmonics of the sampling frequency [16]. Demodulation of PWM signals involve filtering the signal to isolate one of those replica, meaning that linearity of the system is actually required only within a bandwidth equal to that of the RF signal.

Analog PWM fronthauling is the subject of Chapter 2, with experimental results regarding both an innovative optical architecture, based on the reflection and modulation at the RRH of an optical carrier generated at the centralized BBU, and a multilevel PWM to increase signal dynamics. In particular, effective transmission is proven up to 20 km, and aggregation of up to 16 LTE-like 20-MHz channels is demonstrated.

Aggregation of multiple radio signals is mandatory when the RRH includes an array of antennas and leveraging on spatial diversity is indicated and/or necessary (as is the case for millimeter wave carrier frequencies).

1.1.3 Mode Division Multiplexing for Enhanced Analog Fronthauling

The evolution of access networks, indeed, relies on massive antenna arrays at the RRHs and on the use of high carrier frequencies to achieve higher

data rates. In this context, even analog fronthauling could be insufficient in supporting the massive bandwidth requirement, calling for the proposal of additional multiplexing dimensions. Polarization division multiplexing (PDM), e.g., consists in the transmission of two orthogonally-polarized lightwaves, thus providing a two-fold multiplexing gain. Another possibility is to use another spatial characteristic of light, specifically the propagation modes.

Mode division multiplexing (MDM) has been recently proposed for the C-RAN [17]. The main issue with MDM is the introduced intermodal crosstalk, originated for the most part at the multiplexer and demultiplexer. Multimodal longhaul communication relies on coherent detection and optical-MIMO demultiplexing for intermodal interference management, at the price of an excessively high complexity and cost for the application to fronthauling. On the other hand, all-optical passive modal multiplexers and demultiplexers combined with direct detection do not provide the necessary robustness against intermodal crosstalk.

Chapter 3 deals with mode division multiplexing: the intermodal interference is not compensated by any means, but an appropriate mapping between radio and optical resources is shown to effectively reduce the impact of such spatial interference. Radio and optical resources are defined in space and frequency: radio signals received by the array at the RRH are defined by the antenna element and the occupied frequency band, while FH signals on the optical link are defined by the propagation mode and the frequency band. Performance evaluation is for beamforming at the BBU, transparent to the interference introduced by the MDM fronthaul channel, to separate the uplink signals generated by different users on the scene.

1.2 Millimeter Waves Radio Access

A straightforward solution for higher data rates is to increase the communication bandwidth to serve the data-hungry wireless applications of the future, and 5G new radio (NR) envisages bandwidths up to 400 MHz per carrier at the millimeter waves (mmWaves) spectrum above 28 GHz. Although these frequencies are less spectrally crowded than those below 6 GHz, they experience different propagation effects such as higher free-space path loss and atmospheric attenuation, weak indoor penetration, and poor diffraction around objects [18].

The decrease in wavelength, however, enables packing a large number of antennas into small form factors, so that physically small arrays with hundreds of antennas can provide the beamforming gain needed to overcome these undesired propagation effects.

Conventionally, beamforming is performed digitally at the baseband and requires one analog/digital converter per antenna element, which is unfeasible for cost, dissipation and energy consumption when the number of radiating elements N is too high (say $N > 100$). Hybrid analog-digital precoding/combining has been proposed to address these issues [19], making use of phase shifters [20], delay elements such as optical ring resonators (ORRs) [21] or lenses [22] for analog processing to reduce the number of required digital streams. Hybrid beamforming leverages on the spatial sparsity of the mmWave radio channel, efficiently modeled by a few-rays channel: analog spatial filtering allows to reduce the number of RF chain (i.e., downconversion to the baseband and digitization) from N (number of antenna elements) to $L \ll N$ with little performance degradation.

1.2.1 Hybrid Beamforming Split in mmWaves Access

Traditional use of the mmWaves is for point-to-point links, so that in hybrid beamforming (HBF) analog and digital processing is at the same physical location. The proposed use of mmWave frequencies for the access networks compels the integration between HBF and C-RAN and integration between analog fronthauling and hybrid beamforming suggests a beamforming split between an analog processing stage at the RRH and a digital processing at the centralized BBU. In this way the required fronthaul capacity is further reduced thanks to the spatial compression provided by analog beamforming.

Beamforming split between digital processing at the BBU and analog processing at the RAU is addressed in Chapter 4, with a narrowband analog processing based on the phase-only approximation of the dominant eigenvectors of the spatial covariance of the radio signal at the antenna array.

1.2.2 Wideband Optical Signal Processing for Hybrid Beamforming

The wide spread of optical fronthauling and the alluring possibility of seamless integration of analog fronthauling and hybrid beamforming invite to employ optical analog processing at the remote unit to achieve an all-optical analog processing and fronthauling in the context of hybrid beamforming split. In particular, optical signal processing (OSP) allows the design of an optical processing system with compact delay lines that in turn empower the wideband analog beamforming that avoids the beam squint issue incurred when using RF phase shifters for analog processing.

In this way, OSP provides an analog wideband spatial filtering at the remote antennas, while narrowband digital processing at the centralized BBU

completes the beamforming. Wideband analog processing for the HBF has been proposed in literature, but never studied against the fast-changing radio scenario, that requires the update of the optical delay lines with the time dynamics of the radio channel.

In Chapter 5 the need for an adaptive analog processing is highlighted and tunability in the context of 5G NR specifications is considered, emphasizing the necessity of proper ways to manage the limited speed of typical and cost-effective optical solutions. In particular, optical ring resonators (ORRs) with thermo-optic phase shifters are considered for the compact and tunable delay lines, a matching-pursuit approach based on statistical channel knowledge is used in the design of the hybrid beamformer and both a suitable scheduling of users and a time-varying digital processing are proposed to compensate the performance degradation arising from the limited tunability speed of optical components.

1.3 Exploiting the Polarization Dimension for Fronthaul Signaling

The urge to employ adaptive analog processing at the remote antennas calls for a signaling channel between the centralized BBUs and the remote antenna units, to frequently update the settings of the analog beamformer. This signaling channel, parallel to the fronthaul, needs to involve a minimal increase in complexity (in hardware and software) and to avoid the introduction of additional impairments on the FH transmission. A possible cost-effective solution is offered by polarization shift keying (PolSK) [23], which consists in controlling the state of polarization (SOP) of the transmitted lightwave according to a predefined constellation defined in the three-dimensional domain of the Stokes parameters S_1, S_2, S_3. PolSK can be effectively combined with intensity modulation (be it D-RoF or A-RoF) and direct detection of the optical polarization-intensity modulated signal is almost polarization-agnostic, thus guaranteeing the orthogonality between the two channels (FH and signaling). Furthermore, the PolSK receiver itself can be based on direct detection [24], thus guaranteeing cost-effectiveness of the solution. For commercial deployment, the bit stream transmitted via PolSK can be compliant with standardized transport protocols, such as those in the Ethernet family.

In Chapter 6, binary PolSK is considered to transparently augment A-RoF FH based on intensity modulation of the transmitted lightwave. Experimental results proves the effectiveness of the proposed approach: the quality of the A-RoF fronthauling is negligibly impaired by the polarization

modulation, which in turn provides a highly reliably digital link to support BBU-RRH signaling.

1.4 Organization and Contributions

Summarizing, the present Thesis is organized as follows. In Chapter 2 PWM for analog fronthauling is addressed, with experimental results regarding both an innovative optical architecture, based on the reflection and modulation at the RRH of an optical carrier generated at the centralized BBU, and a multilevel PWM to increase signal dynamics. Chapter 3 deals with mode division multiplexing: the intermodal interference is not compensated by any means, but an appropriate mapping between radio resources (antenna elements and frequency bands) and optical resources (mode and frequency) is shown to effectively reduce the impact of such spatial interference. Beamforming split between digital processing at the BBU and analog processing at the RAU is first addressed in Chapter 4, and optical signal processing for wideband analog spatial filtering at the RRH is in Chapter 5: the need for an adaptive analog processing is assessed and tunability in the context of 5G NR specifications is considered. Chapter 6 proposes the use of a binary polarization shift keying (2-PolSK) of intensity-modulated optical signal to provide a signaling channel between BBUs and RRHs, maximally transparent to the transport of fronthauling signals. Last but not least, precise pulse width modulation based on the Sigma-Delta paradigm is dealt with in Chapter 7, and in particular its robustness against timing jitter is shown.

1.5 Publications

The publications corresponding to each chapter are the following:

- Chapter 2: [25–31];
- Chapter 3: [32,33];
- Chapter 4: [34];
- Chapter 5: [35], submitted for publication;
- Chapter 6: [36], submitted for publication;
- Chapter 7: [37].

Chapter 2

Optical PWM for Analog Fronthauling

Contributions

In this Chapter pulse width modulation for analog fronthauling is proposed and experimentally validated as a feasible alternative to digital fronthauling. Two different innovative optical architectures are employed, based on reflection to avoid the need for an optical source at the remote antennas. Last, a multilevel pulse width modulation is demonstrated to be effective in the transport of up to 16 aggregated 20-MHz LTE-like channels.

Organization

This Chapter is organized as follows: Section 2.1 motivates and introduces the use of pulse width modulation for analog fronthauling, introducing the optical architectures that are proposed, described and experimentally validated here. Such optical architectures, based on reflection, are described in Section 2.2. The experimental setup is in Section 2.3 and results in Section 2.4. In Section 2.5 a multi-level pulse width modulation is proposed and validated.

2.1 Introduction

The use of pulse width modulation (PWM) for transmission over optical fibers allows for analog FH with the advantages of a two-level optical waveform as in digital FH with on-off keying (OOK). Optical PWM dates back to the early stages of optical communications [13,14], and it has been recently proposed for analog fronthauling in [15] as the PWM of IQ streams avoids the

bandwidth expansion of CPRI. The PWM is a non-linear modulation that encodes the analog sample amplitudes at the RRH (at BBU in downstream) onto durations of a two-levels on/off optical signal. In spite of the broader spectrum of PW modulated waveforms with respect to the modulating signal, PWM has several benefits in terms of simplicity and tolerance to the optical communication impairments, as it relies on fixed-amplitude pulses. The rationale for PWM analog fronthauling is that bandwidth expansion of digital IQ streaming is mainly due to quantization, thus sampling and quantization are split between RRH and BBU with analog encoding in between (in uplink). In downlink, on the other hand, the digital signal is converted to analog at the BBU, PW modulated and transmitted towards the RRH, where it is PW-demodulated, upconverted to RF and transmitted over the air link. PWM fronthauling then represents an intermediate functional split between the fully centralized architecture of [38] (i.e., CPRI-based D-RoF fronthauling) and A-RoF [10], where the whole analog-digital conversion is at the BBU.

It is to be noticed that PWM for optical FH can be exploited to provide transparent transport of CPRI digital streams: digital PWM can be used, with quantization of the pulse widths, to transport CPRI-encoded IQ samples across the FH link.

Experimental validation of analog PWM FH in [15] is on a standard PON setup consisting in a directly modulated laser for signal generation and a PIN photodiode for optical-to-electrical conversion of the received signal. In this Thesis PWM is proposed and experimentally validated in different optical setups and with different modulation formats, in particular (i) a standard passive optical network with three-level PWM (Fig. 2.1a) (ii) a reflective architecture with broadband optical source and (iii) a reflective architecture with coherent optical source with 2-level PWM (Fig. 2.1b) are investigated.

The first two architectures, represented in Fig. 2.1b, are peculiar because of the location of the optical source, which is at the receiver side of the link together with the photodiode for optical-to-electrical conversion of the received signal. The transmitter is equipped with a modulated reflective semiconductor optical amplifier (RSOA) that receives the seeding signal coming from the optical source, modulates it and reflects it back. This kind of architecture is suitable especially for the uplink, as it allows to simplify the hardware at the RRH: in a WDM PON in which one WDM channel is assigned to each RRH the same hardware is deployed at each antenna site. Indeed, the RSOA response is independent from the wavelength of the incoming seeding signal in a band of about 20 nm, so that the working wavelength is imposed by the channel of the optical multiplexer. Following the same rationale of shifting the complexity toward the centralized BBUs, this reflective PWM

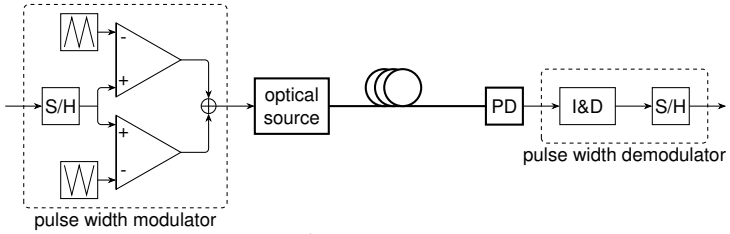

(a) Block diagram of 3-level PWM analog fronthauling in standard PON architecture.

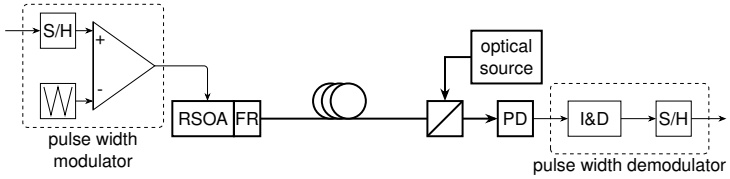

(b) Block diagram of PWM analog fronthauling in reflective PON architecture.

Figure 2.1: Sketch of proposed PWM analog fronthauling.

architecture is not envisioned for the downlink, where a standard PON deployment with a laser source at the BBU and a photodiode at the the RRH is preferred. This is the optical architecture used in the last experimental setup, with a three-level PWM to double the available dynamic range for signal representation.

2.1.1 PWM Analog Fronthauling

The PWM transmission scheme for uplink is sketched in Fig. 2.2a: the radio signal received at the RRH is down-converted to a suitable intermediate frequency (IF), harmonically sampled (similarly to CPRI protocol), PW-modulated by comparison with a triangular waveform and transmitted through an optical network. At the BBU the signal is PW-demodulated to retrieve an estimate of the I/Q samples of the radio signal. Thus the fronthauling chain gives ideally the same output of a CPRI-based FH link, avoiding the need of any update of the rest of the network: at the RRH the sample amplitudes are mapped onto pulse durations instead of being digitized, at the BBU pulse widths are mapped back onto amplitudes by the inverse PWM (PWM^{-1}), digitized and further processed. An example of the involved signals is in Fig. 2.2b: the IF signal $x(t)$ is sampled and its amplitude x_k is mapped onto the duration τ_k of a fixed-amplitude rectangular pulse with maximum duration equal to the sampling interval. This

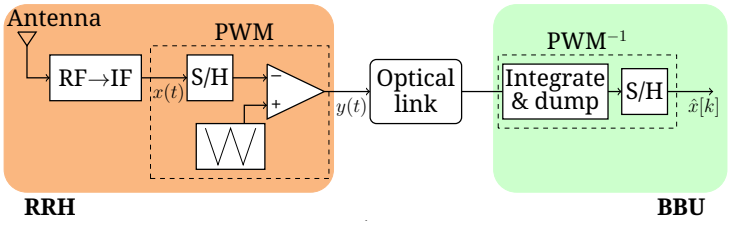

(a) Block diagram of PWM uplink.

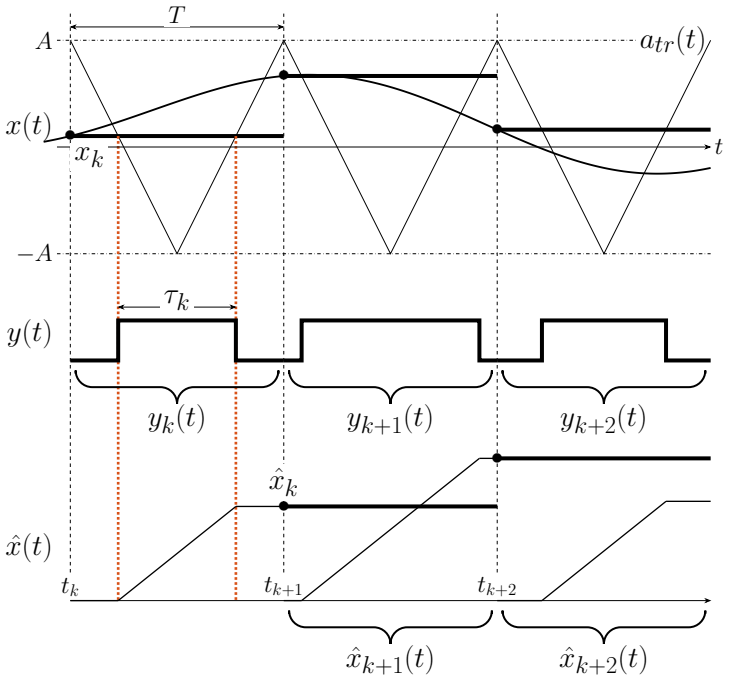

(b) Example of involved signals.

Figure 2.2: PWM fronthauling (uplink), block diagram and involved signals.

is obtained as $\tau_k = \Gamma[x_k] = T(x_k + A)/2A$ through the comparison of the sampled-and-held signal with a triangular wave of period T and amplitude A as in Fig. 2.2b:

$$y(t) = \sum_{k=-\infty}^{+\infty} y_k(t) = \sum_{k=-\infty}^{+\infty} \text{rect}\left(\frac{t - t_k - T/2}{\tau_k}\right) \tag{2.1}$$

The amplitude of the triangular waveform used for modulation sets an amplitude limit above which the signal is distorted. Inverse mapping is obtained integrating the PW-modulated signal over a sampling interval by means of an integrator which is periodically reset: the integrator output at the end of each sampling period gives an estimate of the pulse duration, hence of the sample

amplitude of the original signal. Distortion-free mo-demodulation is obtained either through uniform sampling PWM and integrate-and-dump (I&D) demodulation, or with natural sampling PWM paired with LPF [16,39]. Here the first option is explored for its better integrability with digital signal generation and processing in the experimental setup.

2.1.2 Spectral Characteristics of PWM Signals

A thorough analysis of the spectral characteristics of pulse width modulated signals can be found in [16]: the spectrum $Y(f)$ of the PWM signal is composed by a spectrum $K(f)$, replicated onto each carrier harmonics. Such spectrum $K(f)$ is $K(f) = X(f)$ in case of natural sampling, and a nonlinear function of $X(f)$ in case of uniform sampling. In both cases the baseband portion of the signal is sufficient for correct demodulation, so that, even if the spectral occupancy of the PWM signal is much larger, the whole communication system needs only to have a bandwidth similar to that of the modulating signal $x(t)$ for correct demodulation.

2.2 Reflective PWM Analog Fronthauling

The proposed CRAN fronthauling architecture based on reflective PWM is shown in Fig. 2.3. It relies on a PON exploiting wavelength division multiplexing (WDM) in order to support multiple RRH-to-BBU links as virtual point-to-point connections based on the wavelength resource. In a conventional optical link (essentially a cascade of E/O converter - fiber - O/E converter), the conversion from electrical to optical signal is performed by means of a laser as in [15], where the PWM signal directly modulates a DFB laser. Here we propose a change in perspective: the reflective fronthauling

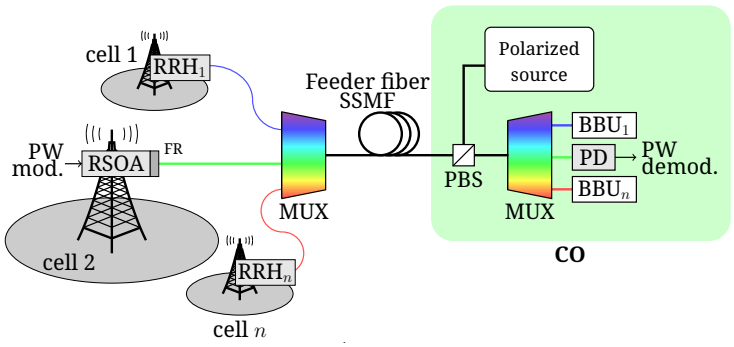

Figure 2.3: Reflective PWM analog FH in C-RAN.

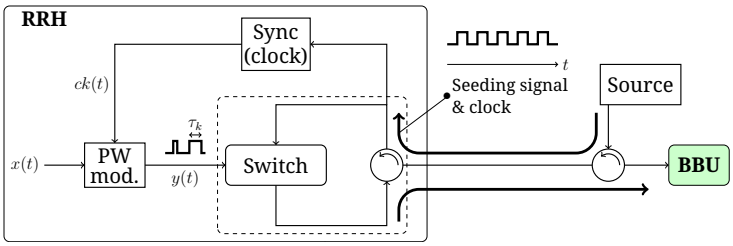

Figure 2.4: Reflective PWM for analog FH, scheme and optical implementations.

architecture proposed in this work is based on reflection controlled by the PWM signal to avoid any optical source at the RRH.

The transmission scheme is reported in Fig. 2.4: a seeding signal is generated at the central office (CO) that hosts all the BBUs and transmitted towards the RRH, possibly with a timing signal for the RRH superimposed. This seeding signal is both processed to retrieve the clock signal – which is used to synchronize the RRH – and fed to the switch, controlled by the PWM signal $y(t)$. The output of the switch is then a PW-modulated signal. Seed and modulated signals can be separated, e.g., by means of a circulator as in Fig. 2.4 both at the RRH and BBU side. The PWM signal of the proposed architecture in Fig. 2.4 is conceptually the same as in Fig. 2.2b with remarkable benefits in terms of cost and adaptability of the reflective transmitter to (virtually) any wavelength and any transmission mean.

The reflective fronthauling allows to synchronize all the RRHs to the clock signal distributed by the BBU as proposed in [40]. The seeding signal is composed by a constant-amplitude part and a superimposed timing signal (e.g., a square wave). At the RRH, the timing signal is used to retrieve a clock signal $ck(t)$ by a phase-locked loop and synchronize all the RRHs (e.g., the S/H and the waveform generator in the PW modulator). In this way, the need of high-quality local oscillators in RRHs is avoided, with great benefits in terms of system complexity and cost. Beside that, a great advantage in terms of robustness to clock jitter lies in the fact that RRHs are synchronized to the broadcasted clock signal distributed by the BBUs through this master-slave synchronization procedure. In this way the clock-stability is up to the BBU with impairments to each RRH. As in [15], at this stage the clock-accuracy is not considered to be the limiting factor for system performances. In fact, it is estimated to be approximately around 10 ppm – well below RAN synchronization requirements [41] – assuming an rms time-jitter of the optical link over 20 km in the range of $10 \div 15$ ps or less and an RF signal with 100 MHz bandwidth (T=5ns). The synchronization procedure, as well as the impact of clock-jitter on system performances, is not analyzed here. Bearing

in mind that the reflective fronthauling architecture paired with PWM can be ideally applied to any communication medium (e.g., copper), this thesis considers the application to an optical network, in which the seeding and PWM signals are transmitted over optical fiber.

The proposed reflective PWM analog fronthauling is experimentally validated with two different optical architecture, one with a broadband source seeding all the RRHs, the other with a bank of coherent sources, each one seeding one RRH. The two architectures, summarized in Fig. 2.3 are detailed in the experimental setup of Fig. 2.5 and described in the following sections.

2.2.1 Reflective PWM with Broadband Seed

In the present architecture the modulated switch functions at the RRH side are implemented by a Reflective Semiconductor Optical Amplifier (RSOA), which simultaneously reflects, amplifies and PW-modulates the incoming seeding signal, and seeding and modulated signals are polarization-separated thanks to the Faraday rotator at the RRH.

To sustain multiple RRH-BBU connections we propose to employ a WDM PON which exploits an external broadband seed to avoid wavelength management of a plurality of seeding sources. The wavelength of the specific connection is determined by the channel of the optical multiplexer/demultiplexer (MUX), that slices the broadband source distributing different slices to different RRHs.

Since the high-power broadband source has to propagate over tens of kilometers of standard single-mode fiber, the Rayleigh Scattering (RS) phenomenon could arise and induce an additive noise to the uplink signal. In order to mitigate the RS noise effect, the specific architecture proposed in Fig. 2.5 can be exploited. In particular, the simultaneous exploitation of a Polarization Beam Splitter (PBS), a low-polarization-dependent-gain (LPDG) RSOA at the RRH side and of a Faraday Rotator (FR) placed at the ONU RSOA leads to a 3-dB reduction of the RS, since seed and signal present orthogonal polarization states.

The proposed reflective PON fronthauling has several benefits: longer feeder fiber are allowed and the employment of an optical circulator (for separating seed and uplink signal) is avoided when employing a polarization-based separation of seeding signal and modulated FH signal. In order to maximize the transmission of the seeding broadband source, a high-polarization-dependent-gain RSOA can be exploited, which can be totally coupled to the feeder fiber thus avoiding any optical loss. Moreover, the optical equipment at the RRH can be hosted in a small form-factor pluggable (SFP) transceiver suitable for the antenna site. Finally, the reflector is colorless and self-tuning

(since its response is independent from the wavelength of the incoming seeding signal in a band of about 20 nm, the working wavelength is imposed by the channel of the optical multiplexer). Thus a self-organized wavelength network qualified for the mobile fronthauling is achieved.

2.2.2 Reflective PWM with Coherent Seed

A second architecture for reflective PWM analog FH is presented here, based on a coherent seed at the CO by means of a bank of laser diodes, one per WDM channel (i.e., one per RRH-BBU connection). While in the architecture presented in Section 2.2.1 the wavelength multiplexer (MUX) at the remote node (RN) slices the broadband source, in this second architecture the MUX separates the seeding signals according to their wavelengths so that each ONU-RRH is seeded by a different WDM channel. Both architectures take advantage of a polarization retracing circuit, which forces the seed and the upstream PWM signals to display orthogonal states of polarization. Although both architectures are colorless externally seeded WDM PONs, the wavelength selection by the seed source influences the FH transmission. In particular, the different coherence characteristics of the seeding sources determine the performance in terms of relative intensity noise (RIN) and tolerance toward chromatic dispersion. More than 20 dB, in fact, differentiates the RIN of the two sources: with coherent seeding a RIN very close to that of the DFB is obtained, i.e., -141 dB/Hz, whereas with a -9 dBm, 50 GHz broadband seed a RIN around -115 dB/Hz is observed [42].

2.3 Reflective PWM Experimental Setup

The two experimental setups exploited to demonstrate reflective PWM FH with broadband or coherent sources are in Fig. 2.5. The PWM signals are prepared via Matlab® and generated by a Tektronix 50 GS/s arbitrary waveform generator with 14-GHz electrical bandwidth. The arbitrary-waveform generator emulates the PW modulated signal that directly drives the RSOA current via a bias-Tee, which adds a variable DC current I_{bias} to bias the chip. The C band ONU RSOA presents an E/O bandwidth of about 3 GHz.

The ONU RSOA is seeded either by a sliced polarized broadband source or by a coherent source. The former is obtained by amplifying the polarized ASE generated by another RSOA with high PDG as described in Section 2.2.1. The coherent sources are obtained by combining an array of DFB lasers using an arrayed waveguide grating (AWG); the lasers have a linewidth of 1 MHz and an output power of 13 dBm as in Section 2.2.2.

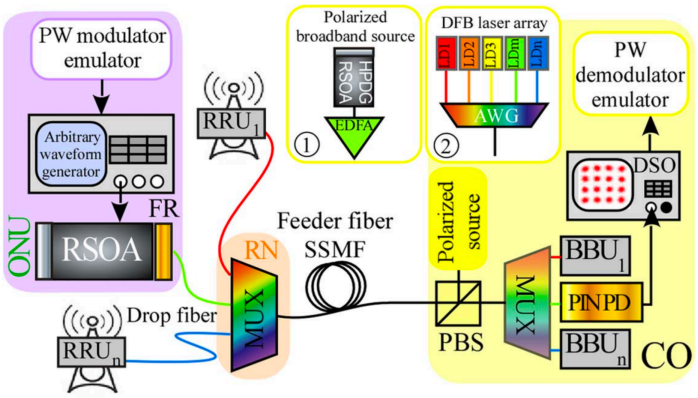

Figure 2.5: Experimental setup for reflection-based optical PWM fronthauling.

The RN MUX is emulated by a wave-shaper filter, which allows to test different MUX channel (identified by their full width at half maximum, FWHM). The optical PWM signal travels back to the MUX and propagates up to 20 km of SSMF. Thanks to the FR its polarization allows the signal to pass through the PBS and to be directly detected by a PIN photodiode (PD) with 1-GHz bandwidth. The received signal is acquired by a Tektronix digital storage oscilloscope (DSO) with 8 bits vertical resolution, 40 GS/s sampling and 12-GHz electrical bandwidth. The 40 GS/s sampled PWM signal is then processed off-line to perform PW-demodulation and measure the overall system performance.

2.4 Experimental and Numerical Results

The transmitted signal is a calibration sequence that samples the duration domain for the rectangular pulses in order to build the amplitude-calibration map by integrating the received signal and mapping back the pulse widths onto sample amplitudes. This measure can fully characterize the deterministic link distortion and the random noise of the optical PWM link. To avoid pulse-broadening-induced inter-symbol interference (still not considered at this stage), the transmitted PWM uses half of the sampling interval $T = 5$ns (equivalent to that of a 100-MHz bandwidth real signal, or a 50-MHz bandwidth I/Q modulated signal) up to $T/2 = 2.5$ns. The estimated pulse width is $\hat{\tau}_k = \tau_k + \Delta\tau_k$, where $\Delta\tau_k$ represents the FH noise. The dispersion of the estimated pulse widths around the mean values is shown in Fig. 2.6 together

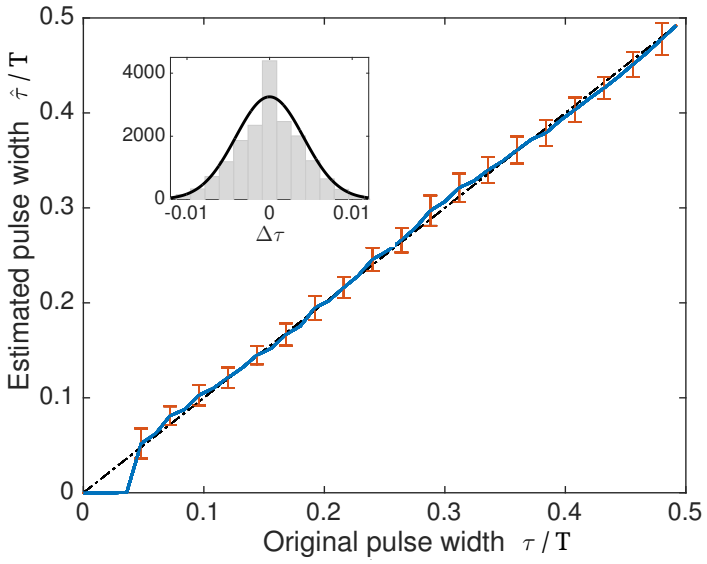

Figure 2.6: Average calibration curve with error bars ($\pm 3\sqrt{\mathrm{E}[\Delta\tau_k^2]}$) for a broadband source at the CO, the histogram of the pulse width errors is in the box.

with the calibration curve. On the same figure is shown the histogram of the PWM noise to highlight that it can be approximated as Gaussian.

The experimental results in Fig. 2.6 shows that the dispersion around the mean calibration curve is approximately constant with respect to pulse width as expected. Due to the low SNR values and the distortion experienced by short pulses, a suitable interval for PWM is evaluated from the experiment at hand to be $\tau \in [0.1T\ ,\ 0.9T]$.

Remark PW-demodulation of received data consists in numerical integration after thresholding the signal. This to reduce the influence of the noise introduced by the optical link (e.g., shot noise), at the expense of a reduced available dynamics as the shortest pulses are not detected. In this way the system behaves as if the analog signal received by the PD is thresholded before being integrated by an analog circuit: the residual noise component is due to a jitter on the position of pulses edges.

2.4.1 Operating Point for the Reflective PON

A preliminary evaluation has been performed in order to determine the best operation conditions of the RSOA-based optical network in terms of RSOA bias current, MUX FWHM and power output of the seed source. The

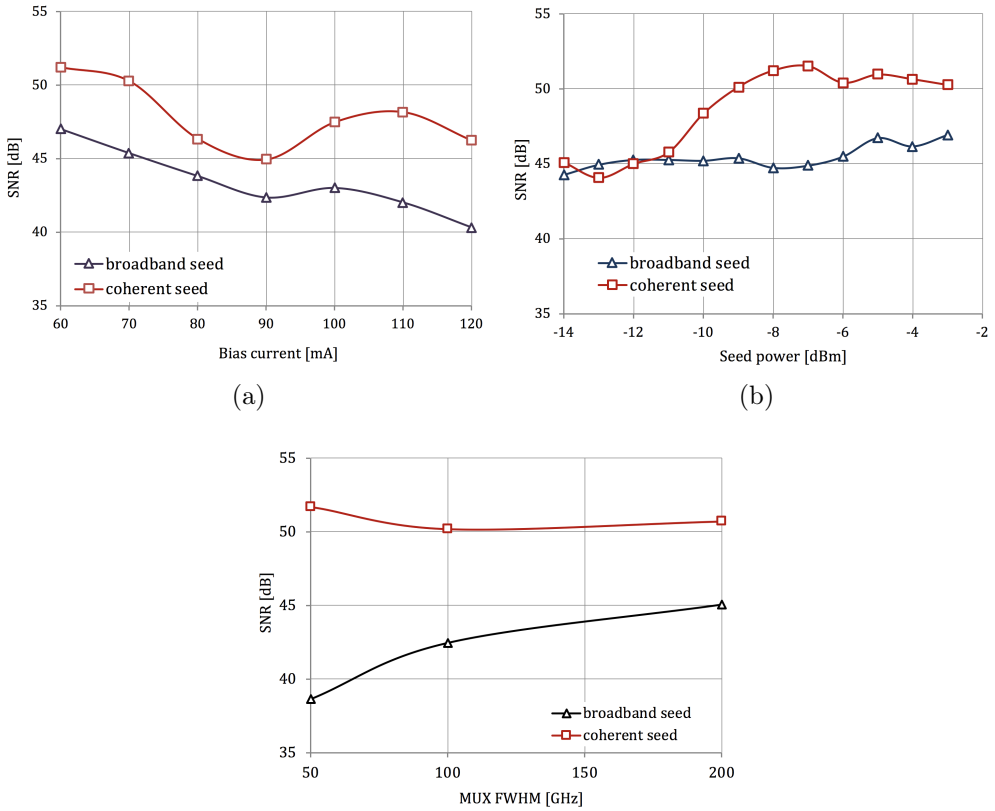

Figure 2.7: Average SNR versus bias voltage (a), seed power (b) and FWHM of the WDM channel (c).

performance comparison between the reflective architectures with broadband or coherent source at the CO is in Fig. 2.7 in terms of average SNR to evaluate the impairment introduced by the optical network.

In order to maximize the transmitted signal extinction ratio mid range bias currents should be chosen, but an excessive lowering would reduce the RSOA gain and the link power budget, thus 60-mA bias has been selected for the final experimental tests. Moreover, wider MUX FWHM are associated with lower source relative intensity noise (RIN) and thus higher transmission SNR, but at the expenses of a lower number of WDM channels supported by the system; as the best trade-off we have chosen a 100-GHz FWHM MUX. Finally, higher seeding levels allow to obtain a better compression of the RIN associated with the sliced source [42]. A seeding power of -9 dBm has been chosen as compromise between performance (in Fig. 2.7b there is no substantial gain in SNR with a seed power greater then -9 dBm) and allowed ODN losses (22dB), that include propagation, optical filters and splitters.

2.4.2 Performance Analysis of CRAN System

The impact of reflection-based PWM fronthauling is evaluated in terms of EVM by means of numerical simulations relying on the FH channel characterization in Section 2.4.1. To gain insight on the system, the signal transmitted over the radio channel is assumed to stem from a M-QAM constellation: the received signal at the antenna is:

$$x(t) = \sum_k a_k h(t - kT) + n(t) \tag{2.2}$$

where $a_k \in \{\pm 1 \pm j, \pm 3 \pm 3j, \dots\}$, $h(t)$ is the air-link waveform (here it is assumed to be a root-raised-cosine filter with 0.2 roll-off) and $n(t)$ is the RF additive white Gaussian noise (AWGN) introduced by the radio channel. At the RRH, after some filtering to suppress out-of-band noise, the signal is sampled at the Nyquist rate, PW-modulated and a noise contribution is added to account for transmission through the optical link. At the BBU, after PW demodulation, matched filtering by $h^*(-t)$ is performed to obtain the sample amplitudes of the decision variable:

$$\hat{a}_k = a_k + \sum_\ell (n(\ell T) + w_\ell) h((k - \ell)T) \tag{2.3}$$

where w_ℓ is the FH noise introduced by the optical link after PW demodulation and perfect gain control is assumed. Overall, a complete connection from mobile user to BBU is simulated in which the signal is shaped at the radio transmitter through a root-raised-cosine filter, transmitted through the radio channel, PW-modulated at the radio receiver and relayed towards the BBU, where matched filtering is performed.

Performances are evaluated in terms of average error vector magnitude (EVM) of the overall (radio and optical) noise at the decision variable, simulated by varying the received optical power and the radio-link SNR for 64-QAM. The EVM is a function of two variables, namely the received optical power and the radio-link SNR. Results are shown in Fig. 2.8 for different lengths of the feeder fiber (back-to-back, 10 and 20 km). At low radio-link SNR the fronthauling noise is negligible, whereas at large SNR values it gives a floor in EVM and in error probability (not shown here). EVM values are in all cases below the 8% that is limit for LTE air-link [41]. The region where EVM<3.5% (the 3GPP limit for 256-QAM in LTE) is highlighted in Fig. 2.8c, where the contour lines of EVM as function of both radio-link SNR and received optical power are shown.

To summarize the performance of all the considered PWM optical architectures, the EVM evaluated on the whole connection between the UE

and the BBU pool is considered for all the three choices: the standard PON in [15] and the two reflective PWM C-RAN proposed here. Results are in Fig. 2.9.

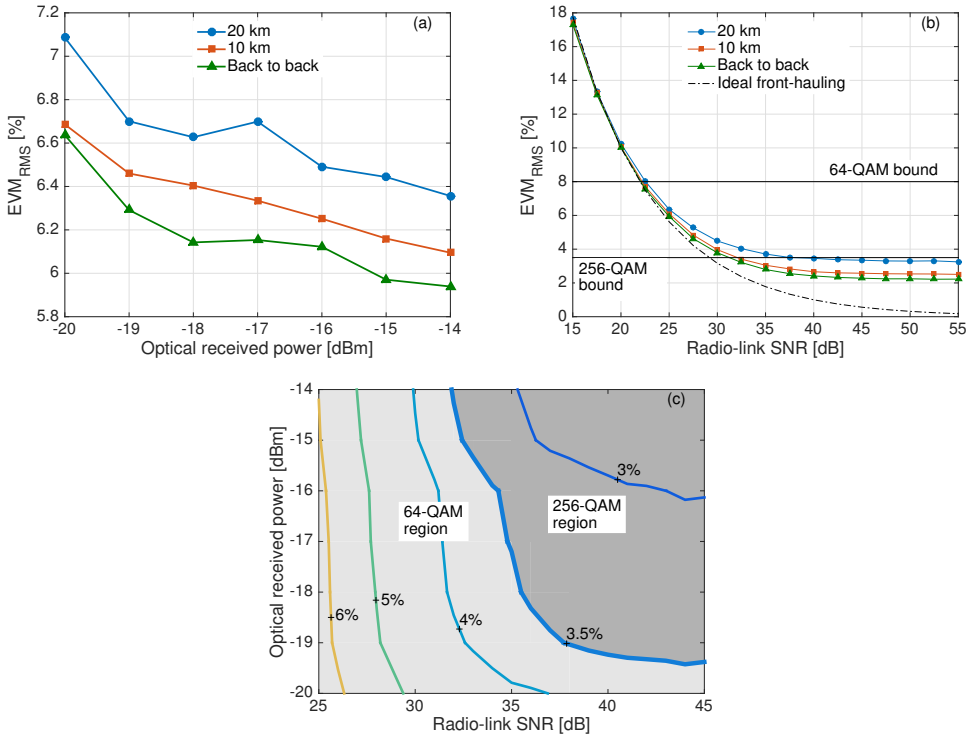

Figure 2.8: Simulation results for 64-QAM transmission and broadband source at the CO. EVM as function of: (a) received optical power at 25-dB radio-link SNR, (b) radio-link SNR at -14dBm received optical power. Contour lines (c) for EVM vs radio-link SNR and optical received power for 10km link.

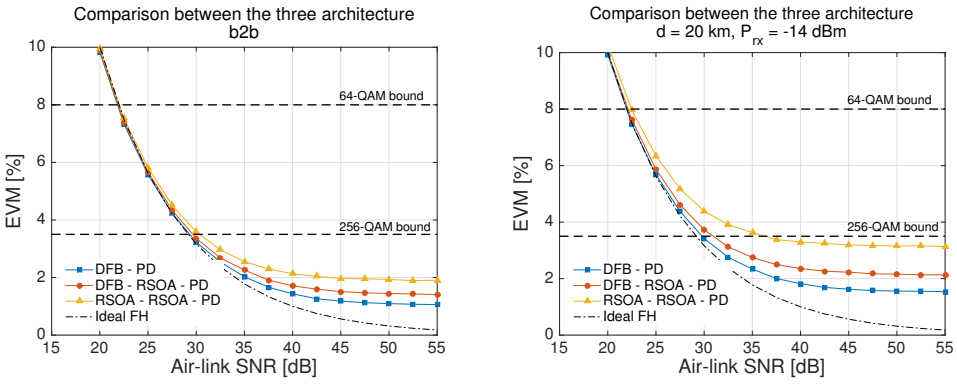

(a) (b)

Figure 2.9: EVM versus air-link SNR for the three optical architectures considered.

2.5 Three-level PWM for Analog Fronthauling

Differently from previous work in which the transmitted optical signal is a PW-modulated two-level waveform, here a three-level pulse width modulation is proposed. This is a specific case of multilevel PWM (M-PWM), which is a mixed amplitude-duration modulation. In particular, in 3-level PWM the representation of signal $x(t)$ is by means of both pulse duration τ and a binary variable (positive or negative amplitude). In this way the dynamic range for signal representation is effectively doubled. Fig. 2.10 shows the proposed PWM architecture and the involved signals are depicted in Fig. 2.11. Even though Fig. 2.10 refers to the uplink transmission from RRU to BBU, the M-PWM system is envisioned for the downlink as well, with minor adaptation of the following description.

With reference to Fig. 2.10, the received RF signal is down-converted to a suitable intermediate frequency (IF) and it is harmonically sampled.

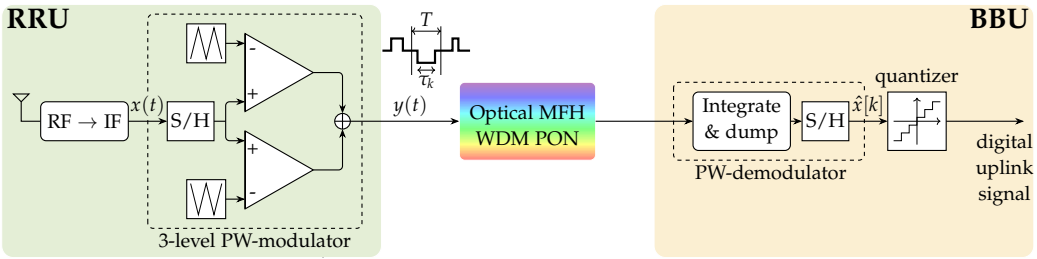

Figure 2.10: 3-level PWM mo-demodulation scheme with reference to the uplink..

Differently from the conventional 2-levels PWM [15], the sampled signal $x[k]$, input to the PW-modulator, is compared to two different triangular waves, respectively red and blue in Fig. 2.11. The two triangular waves, combined, cover the whole amplitude dynamic of the input signal: the red one in $[0, A]$ and the blue one in $[-A, 0]$. The output signals of the two comparators are then summed to obtain the modulated 3-levels PWM signal $y(t)$. The sampled signal is then encoded into pulses of duration $\tau_k = |x_k|/A$ and amplitude $\text{sign}(x_k/A)$:

$$y(t) = \sum_{k=-\infty}^{\infty} y_k(t) = \sum_{k=-\infty}^{\infty} \text{sign}(x_k/A) \cdot \text{rect}\left(\frac{t - t_k - T/2}{\tau_k}\right) \quad , \qquad (2.4)$$

where T is the sampling interval. Demodulation is performed by an integrator that is periodically reset at the end of each sampling interval to obtain the estimated sampled signal $\hat{x}[k]$. In case of M-PWM with more than three amplitude levels, the integrator needs to be preceded by a decision on the received amplitude level. This is to avoid the amplitude-duration ambiguity that would arise from straightforward integration of the received signal.

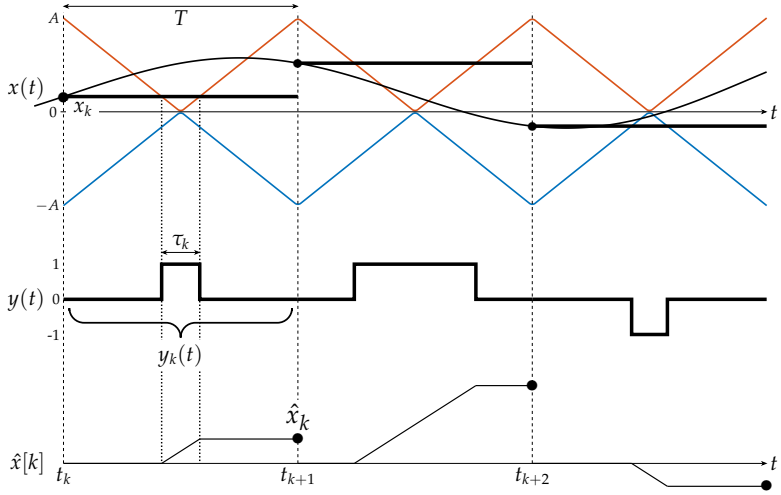

Figure 2.11: Examples of 3-level PWM signals. From top to bottom: input signal $x(t)$ together with the two triangular reference waveforms, the M-PWM signal $y(t)$, and the estimated sample amplitude $\hat{x}_k$ after PW demodulation..

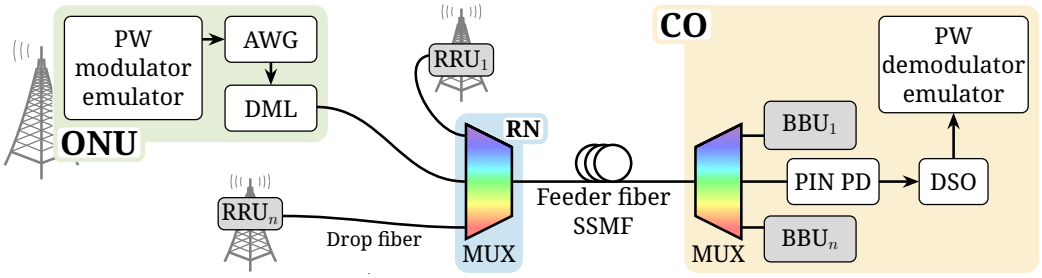

Figure 2.12: WDM PON PWM fronthauling and experimental setup..

2.5.1 M-PWM FH architecture and experimental setup

The transmission scheme of Fig. 2.10 is used to transport LTE-like signals aggregated via frequency division multiplexing (FDM) in a WDM PON, as the one in Fig. 2.12. The samples of the I and Q components are mapped onto the duration and (binary) amplitude of the transmitted rectangular pulses as previously described. In particular, the pulse duration is $\tau_{min} < \tau < \tau_{max}$, where τ_{min} depends on the electro-optic bandwidth of the fibre-optic network devices and $\tau_{max} \leq T$. In this work, $\tau_{max} = 0.9T$ to avoid intersample interference that may arise due to pulse broadening. Moreover, to fairly compare conventional 2-level PWM and the 3-level PWM, the multilevel option is evaluated both taking advantage of the full duration dynamic, i.e., $\tau \in [\tau_{min}, \tau_{max}]$, and with halved dynamic to compensate for the doubling deriving from the binary amplitude. The halved dynamic is $\tau \in [\tilde{\tau}_{min}, \tilde{\tau}_{max}]$, where $\tilde{\tau}_{min} > \tau_{min}$ and $\tilde{\tau}_{max} < \tau_{max}$, so that $\tau_{max} - \tau_{min} = 2 \cdot (\tilde{\tau}_{max} - \tilde{\tau}_{min})$. At the BBU, after detection, the demodulator transforms the M-PWM signal into amplitude samples by an integrator that is periodically reset every sampling interval T, as in conventional PWM. In this work either 8 or 16 aggregated 20-MHz LTE-like signals are transmitted, so that the sampling interval is either $T = 2$ ns or $T = 1$ ns respectively.

The experimental setup in Fig. 2.12 describes the WDM PON that supports the PWM FH transmission. At the optical network unit (ONU), the M-PWM (uplink) signal drives a directly modulated laser (DML) with 15-GHz bandwidth. Such M-PWM signal is prepared via Matlab and generated by a Tektronix 50 GS/s arbitrary waveform generator (AWG) with 14-GHz bandwidth. After propagation through the drop fiber, signals coming from different ONUs are combined at the remote node (RN) via wavelength multiplexing and coupled to the SSMF feeder fiber. In particular, the MUX is a 32-channel athermal arrayed waveguide grating, which, if necessary, could be replaced by a power splitter in order to support TWDM-PON compliant

optical distribution networks. At the central office (CO), the different RRUs signals are separated by the wavelength demultiplexer and sent to the corresponding receiver. Each receiver consists in a PIN photodiode (PD) with 12-GHz bandwidth that performs direct detection, followed by a pulse width demodulator. PW demodulation is performed via offline signal processing: the PD output signal is acquired by a Tektronix digital storage oscilloscope (DSO) with 8 bits vertical resolution, 50 GS/s sampling and 23-GHz electrical bandwidth. Offline processing via Matlab delivers pulse width demodulation consisting in signal thresholding and integration, together with the performance evaluation of the FH link. Thresholding helps reducing the noise level of the received signal, by comparing the received signal $y_{rx}(t)$ with a fixed value $\bar{y}_{th}$ and assigning to the received signal a value $+1$ when $y_{rx}(t) > \bar{y}_{th}$, a value -1 when $y_{rx}(t) < -\bar{y}_{th}$ and a value 0 when $-\bar{y}_{th} < y_{rx}(t) < \bar{y}_{th}$.

2.5.2 Experimental results

System performance is assessed, after 7.5-km SSMF transmission, in terms of error vector magnitude (EVM) to characterize the signal degradation introduced by the FH segment.

Calibration procedure

The performance assessment is preceded by a calibration procedure in which a sequence of pulses is transmitted, so that their duration values cover the whole pulse width dynamic. This allows to determine both the optimal threshold level $\bar{y}_{th,opt}$ before integrating the received PWM signal and the amplitude-width correspondence of the entire link. An in-field unit would have to repeat the calibration procedure according to the aging dynamics of the optical and electronics devices. An example of the results of the calibration stage is presented in Fig. 2.13: Fig. 2.13a shows the calibration curve obtained for the cases of full and halved duration dynamics. All the received instances of the calibration pulse of duration $\tau = 0.27 \cdot T$ are displayed in Fig. 2.13b, together with the optimal threshold level $\bar{y}_{th,opt}$. Such optimal threshold is chosen so as to minimize the average noise level of the received calibration signal.

EVM measurements

After the calibration step the M-PWM architecture can be employed for the transmission of LTE-like mobile signals. Fig. 2.14 presents the results for a received optical power $P_{rx} = -8$ dBm, when a 3-level PWM signal with full

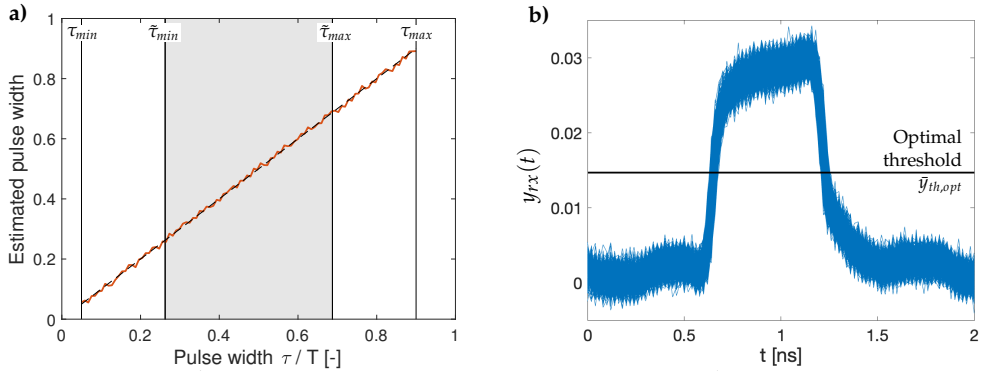

Figure 2.13: (a) calibration curve with highlighted duration domains: full (τ_{min}, τ_{max}) and halved ($\tilde{\tau}_{min}$, $\tilde{\tau}_{max}$) dynamics; (b) superimposition of the received instances obtained during the calibration stage for the pulse of duration $\tau = 0.27 \cdot T$..

duration dynamic is used for the MFH. In particular, Fig. 2.14a shows the EVM per subcarrier for $N_{ch} = 8$ aggregated LTE-like 20-MHz signals: each 20-MHz OFDM signal is composed of 1200 15-kHz subcarriers with 64-QAM modulation, plus 848 15-kHz guard subcarriers. Fig. 2.14a shows similar EVM levels for all the 15-kHz subcarriers, thus in the following results the average EVM is considered as performance metric. Fig. 2.14b shows the received 64-QAM constellation per subcarrier.

The mean EVM after averaging along all the $1200 \cdot N_{ch}$ subcarriers is in Fig. 2.15 for $N_{ch} = 8$ (Fig. 2.15a) and $N_{ch} = 16$ (Fig. 2.15b). Fig. 2.15a compares the performance of the two codes with equal representation

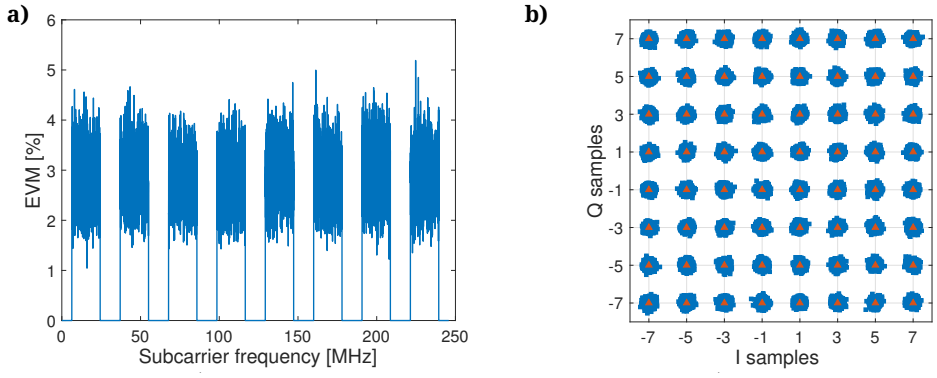

Figure 2.14: Percentage EVM against subcarrier frequency (a), and received constellation (b) for 3-level PWM with full dynamic, 8 aggregated 20-MHz LTE-like channels, 64-QAM, $P_{rx} = -8$ dBm..

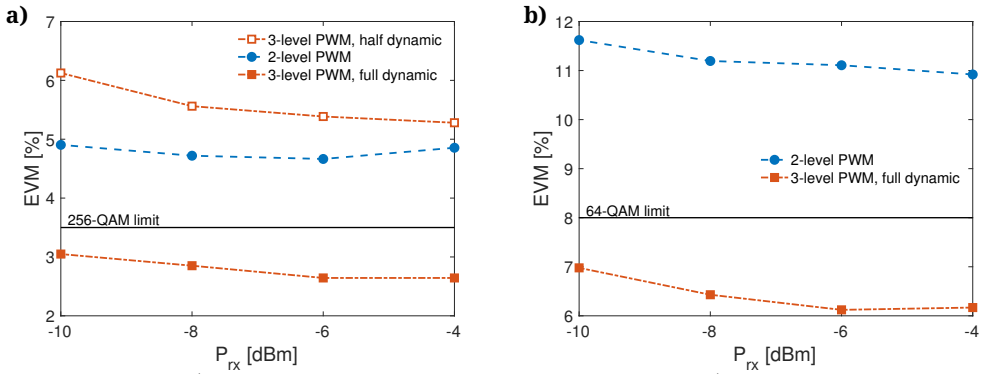

Figure 2.15: Average percentage EVM against received optical power P_{rx}, $N_{ch} = 8$ (a) and $N_{ch} = 16$ (b) aggregated 20-MHz LTE-like channels, 64-QAM..

dynamics: as expected the conventional 2-level PWM (full blue circles) performs slightly better than the half-dynamic 3-level PWM (open red squares). Anyways, both modulation formats guarantee an EVM level well below the 8% that is the LTE limit for 64-QAM. A full-dynamic 3-level PWM, on the other hand, results in an average EVM below the 256-QAM limit (3.5%), thus allowing the higher modulation format at least for some of the subcarriers. The difference in performance between 3-level and conventional PWM is even more apparent when considering 16 aggregated channel, as in Fig. 2.15b. In this case, indeed, conventional 2-level PWM cannot satisfy the EVM specifications for 64-QAM, while 3-level PWM achieves an average EVM around 6%.

2.6 Concluding Remarks

In this Chapter analog 2-level pulse width modulation fronthauling is experimentally validated with two different reflective PON architectures, employing either a coherent or a sliced broadband source to generate the seeding signal and a RSOA for modulating and reflecting the optical signal. The result is a colorless self-tuning WDM PON supporting PWM FH with several advantages in terms of complexity and cost. For both the alternatives (coherent or broadband source), when considering a 100-MHz bandwidth of the fronthaul signal, the impact of PWM fronthauling is negligible for small SNR values on the radio link (SNR$<$25 dB) and at larger SNR values the systems meets the LTE requirements (EVM$<$8%) for 64-QAM after 20 km feeder fiber, giving a floor at EVM$\simeq$ 3%. LTE requirements for 256-QAM (EVM$<$3.5-4%) are met with 10 km optical link. To improve the FH capacity a 3-level PWM is also considered and proved to support up to 8 aggregated 20-MHz LTE-like channels while satisfying EVM requirements for 256-QAM, and up to 16 aggregated channels while satisfying EVM requirements for 64-QAM, for a 7.5-km connection and a standard PON setup.

Chapter 3

Mode-Frequency Multiplexing over Fiber for Analog Fronthauling

Contributions

This Chapter proposes a joint mode-frequency division multiplexing of optical signals for analog fronthauling. The solution is called Radio-over-Modes and it is based on all-optical passive mode (de)multiplexing. The architecture is evaluated against a realistic uplink radio scenario, and performances are assessed considering beamforming at the BBU to separate signals from different users. In particular, beamforming design is transparent to the intermodal interference. The only degree of freedom to counteract such interference is given by the mapping between the space-frequency resources of the air link and the space-frequency resources of the optical fronthauling. Dynamic mapping allows to approach the performance of ideal fronthauling, i.e., with no interference among FH channels.

Organization

Section 3.1 motivates and introduces joint space and frequency multiplexing of optical signals exploiting the mode dimension for spatial diversity. The analyzed system model is in Section 3.2, and the beamforming scenario used to evaluate the impact of the arising interference between the space-frequency FH channels is in Section 3.3. Simulation results are in Section 3.4 and the expansion to high-dimensionality problems (i.e., large antenna arrays) is in Section 3.5.

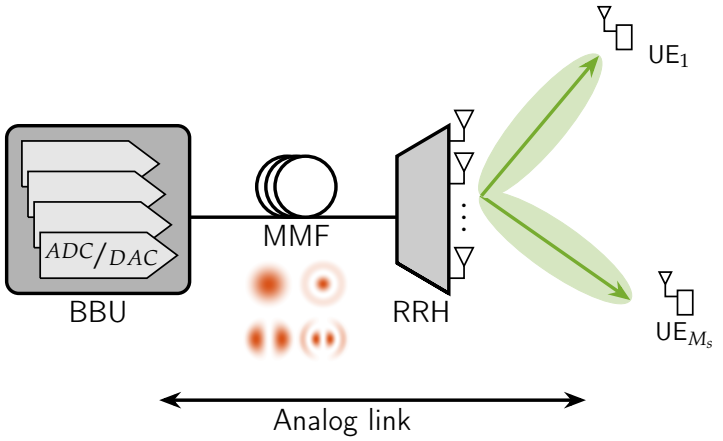

Figure 3.1: MDM-based C-RAN.

3.1 Introduction

To satisfy the bandwidth requirements on the fronthaul link due to massive antenna array and large bandwidths of the RF signals, the only viable solution appears to be the overtaking of conventional digital fronthauling in favor of a fully analog transmission [10,15,43,44]. This enables the reduction of the bandwidth requirements, the latency and the hardware cost, while improving the energy efficiency, since only analog signal relaying is performed at the RRH toward BBU (and viceversa). One possibility is to deploy an analog fronthaul based on the radio over fiber (RoF) paradigm, due to its capability to carry several Gbit/s [10,44] in terms of equivalent data rate. However, the required bandwidth scales with the number of antennas at the RRH that can be huge if considering the over-6GHz spectrum occupancy (say $\gg$ 10 GHz), thus rising the corresponding data-rate up to several tens of Gbit/s for RRH. In this scenario, the huge bandwidth provided by optical link could be even not enough, calling for the need of a new multiplexing dimension. Here we consider mode division multiplexing (MDM) to overcome the bandwidth limitations of RoF architecture by taking advantage of the different propagation modes of light on fiber.

The concept of MDM has old roots [45] and just nowadays it is proposed for longhaul communications thanks to coherent detection and optical-MIMO demultiplexing [46]. However, the application of MDM to C-RAN has relatively short history [17] and not much research effort has been devoted to its investigation. The main issue is represented by the severe crosstalk among different modes (intermodal crosstalk) introduced by commercial devices available on the market. In fact, the technologies employed in longhaul

communications present excessively high complexity and costs for the access network while the simple employment of all-optical passive modal multiplexer (MUX) and demultiplexer (DEMUX) combined with direct detection is not robust enough to cope with intermodal crosstalk.

In this Chapter we propose a radio over modes (RoM) mobile fronthauling (MFH) exploiting MDM and frequency division multiplexing (FDM) to serve a large number of antennas (>100), supported by low-cost and energy efficient direct detection and all-optical passive (de)multiplexers. In the characterization of the effects of intermodal crosstalk two different technologies are taken into account: photonic lanterns (PLs) [47] and multi-plane light converters (MPLCs) [48]. In particular, we show how to overcome the limitations due to the intermodal crosstalk through a dynamic antennas to mode/frequency mapping, where the optical channels defined in the mode-frequency dimensions are optimally allocated to the signals from/to the RRH antennas, based on the performance metric defined for the radio scenario using the principle that fronthauling should be transparent for RAN.

To have meaningful results, RoM performance evaluation is carried out for a sample scenario in which a beamforming is performed at the BBU to separate the useful uplink signal from interference arising from neighboring hot-spots. The optical channel is assumed to be maximally transparent to the beamformer that is designed based only on statistical knowledge of the radio channel (i.e., not instantaneous).

3.2 System Model

In this Chapter we consider a C-RAN based on RoF paradigm where optical fronthauling employs MDM and FDM to separate/aggregate signals from/to different antennas. In particular, we focus on beamforming to separate uplink signals from M_S users served by a specific cell, with interference coming from M_I users in a neighboring cell (downlink would be similar, not covered here). The analog signals received at the RRH by N antennas are directly relayed through a multimode fiber (MMF) link towards the BBU, where receiver processing is performed (e.g., beamforming). Therefore the estimated user signal $\hat{\mathbf{s}}$ at the BBU is described by

$$\hat{\mathbf{s}} = \mathbf{W}\mathbf{H}_{opt}(\mathbf{H}_r\mathbf{s} + \mathbf{n}), \tag{3.1}$$

where the matrices $\mathbf{W}$, $\mathbf{H}_{opt}$ and $\mathbf{H}_r$ are respectively the beamformer, the optical channel, and the radio channel shown in Fig. 3.2 and defined in the following sections. Vectors $\mathbf{s}$ and $\mathbf{n}$ contain the user signals and the noise at

the antenna array respectively, and optical noise is neglected (or accounted for in the noise vector $\mathbf{n}$).

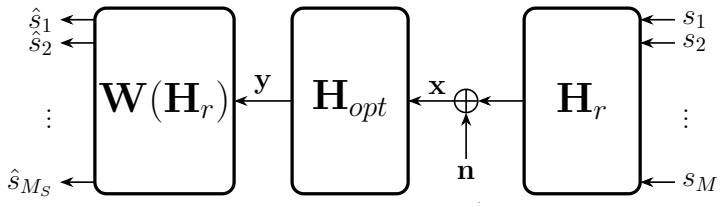

Figure 3.2: System model, uplink.

3.2.1 Radio Scenario

The signals received by the N antennas at the RRH, arranged in a vector, are:

$$\mathbf{x} = \mathbf{H}_r\mathbf{s} + \mathbf{n} \tag{3.2}$$

where $\mathbf{s} \in \mathbb{C}^M$ collects the signals with power σ_s^2 transmitted by all the $M = M_S + M_I$ users and assumed to be Gaussian distributed, i.e., $\mathbf{s} \sim \mathcal{CN}(\mathbf{0}, \sigma_s^2\mathbf{I})$. $\mathbf{H}_r \in \mathbb{C}^{N\times M}$ is the wireless channel matrix and $\mathbf{n} \sim \mathcal{CN}(\mathbf{0}, \mathbf{R}_n)$ is the $N \times 1$ noise vector. The wireless channel model is based on the far field approximation and it accounts for the directions of arrival (DoAs) of the signals:

$$\mathbf{H}_r = \begin{bmatrix} \beta_1\mathbf{a}(\theta_1) & \beta_2\mathbf{a}(\theta_2) & \cdots & \beta_M\mathbf{a}(\theta_M) \end{bmatrix} \tag{3.3}$$

where $\beta_i^2 = 1/d_i^2$ is the path loss attenuation related to the distance d_i from the i-th user to the array, $\mathbf{a}(\theta_i) \in \mathbb{C}^N$ is the steering vector for the direction of arrival (DoA) θ_i of the i-th user. Under the assumption of $\lambda/2$-spaced uniform linear array (ULA) at the RRH, the steering vector for the i-th user is:

$$\mathbf{a}(\theta_i) = \begin{bmatrix} 1 & e^{j\pi\sin(\theta_i)} & \ldots & e^{j\pi(N-1)\sin(\theta_i)} \end{bmatrix}^T. \tag{3.4}$$

For simplicity, no fading nor multipath propagation are considered but extension would just include a temporal processing. Furthermore, it is here assumed the presence of a single user to be served in the cell of interest ($M_S = 1$). The symbols transmitted by each user (including the interferers) are assumed to be normalized to have unit power ($\sigma_s^2 = 1$).

3.2.2 MDM-based Optical Fronthaul with Direct Detection

The (analog) radio signal $\mathbf{x}$ received at the RRH is directly forwarded over a fiber connection without any digitalization. Here we propose to employ multimode optical transmission for such fronthaul links and to have the signals from the different antennas multiplexed in the mode-frequency dimension, with simultaneous use of MDM and FDM. Let us first consider a simplified environment in which only MDM is used to aggregate few antennas, and let us consider optical channel matrices measured in the literature and described in the following. The signal $\mathbf{y} \in \mathbb{C}^N$ received at the BBU can be described as:

$$\mathbf{y} = \mathbf{H}_{opt}\mathbf{x} = \mathbf{H}_{opt}(\mathbf{H}_r\mathbf{s} + \mathbf{n}) \tag{3.5}$$

where $\mathbf{H}_{opt} \in \mathbb{R}^{N\times N}$ represents the multimodal channel model: the main diagonal elements $\left[\mathbf{H}_{opt}\right]_{ii}$ are the insertion losses and the off-diagonal terms $\left[\mathbf{H}_{opt}\right]_{ij}$ represent the intermodal coupling coefficients from the j-th to the i-th mode. A degree of freedom in the system management is given by the possibility to optimize the optical channel assignment, that is the optimal association between each of the N RRH antennas and fiber modes based on end-to-end performance metrics for radio link defined in Section 3.3.2. This can be modeled with an optical channel described by any permutation of a reference optical channel matrix as:

$$\mathbf{H}_{opt} = \mathbf{P}^T\mathbf{H}_{ref}\mathbf{P} \tag{3.6}$$

where $\mathbf{P}$ is a permutation matrix that is for a reference optical channel matrix $\mathbf{H}_{ref}$ which is the coupling matrix taken from the literature. The optical channel assignment is shown in Fig. 3.3, where the effect of the permutation matrix $\mathbf{P}$ is highlighted.

In particular, passive and all-optical devices are considered for mode multiplexing and demultiplexing just to minimize any architectural complexity and to avoid the use of coherent detection and optical-MIMO processing, thus reducing cost and power consumption. Among the different propagation modes, degenerate modes show the same propagation constant but orthogonal states of polarization, therefore in case of direct detection it is impossible to separate them without a suitable polarization control: in this case the pairs of degenerate modes constitute fully-coupled channels that remarkably impair the antennas array capability. Fiber propagation is on weakly-coupled few-mode fibers (FMFs), that show weak intermodal crosstalk, in the order of -30 dB/km for commercial 6-LP FMF allowing the propagation of 4 non-degenerate modes corresponding to 6 spatial modes [49]. Prototype 12-LP

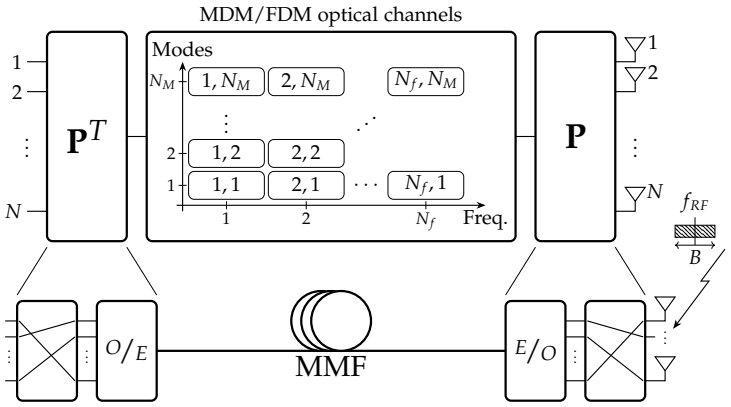

Figure 3.3: MDM/FDM optical channel assignment.

FMF (with 7 non-degenerate modes corresponding to 12 spatial modes) is currently a research matter. In a broader temporal horizon, 50-μm graded-index multi-mode fiber (MMF) can support 30 LP modes (55 spatial modes). As far as the mode (de)multiplexing is concerned, the actual crosstalk measurements for (de)multiplexers available on the market or described in the literature for out-of-coherence sources is taken into account here, to show the actual feasibility of the proposed RoM architecture. Two different technologies are considered: 6-LPs [50] and 10-LPs [51] non-mode selective PLs – emerging as the most promising and compact multiplexing solution in case of high number of modes and optical-MIMO-assisted demodulation – and MPLC-based solutions allowing commercial MUX/DEMUXs operating up to 10 modes [52].

3.3 Beamforming model

Beamforming, that is performed at the BBU side, is supposed to act on the signals received by the antenna array. This means that beamforming does not act directly on the RRH signal $\mathbf{x}$, but on the signal $\mathbf{y} = \mathbf{H}_{opt}\mathbf{x}$ received after the optical channel $\mathbf{H}_{opt}$, which is transparent to the beamforming design.

Minimum variance distortionless (MVDR) beamforming is adopted here to retrieve an estimate of the signal transmitted by the user from the overall signal $\mathbf{y}$ received at the BBU:

$$\hat{s} = \mathbf{w}_{\mathrm{MVDR}}^{H}(\theta_{UE})\,\mathbf{y} \tag{3.7}$$

where $\mathbf{w}_{\mathrm{MVDR}} \in \mathbb{C}^N$ is the spatial filter for the DoA of the user, indicated with $\mathbf{w}$ for compactness in the following. MVDR beamforming aims at min-

imizing the overall mean power after the spatial filtering with the constraint that for the DoA of interest θ_{UE} the beamforming response has unit-gain (distortionless constraint):

$$\mathbf{w} = \frac{\mathbf{R}_x^{-1}\mathbf{a}(\theta_{UE})}{\mathbf{a}^H(\theta_{UE})\mathbf{R}_x^{-1}\mathbf{a}(\theta_{UE})}. \tag{3.8}$$

The matrix $\mathbf{R}_x$ indicates the covariance matrix that contains both the signal of interest and the interference plus noise at the RRH (i.e., the signal on which beamforming is supposed to act). Since these contributions can be considered as mutually independent, and assuming the noise at the array to be spatially white, it is:

$$\mathbf{R}_x = \beta_{UE}^2\mathbf{a}(\theta_{UE})\mathbf{a}^H(\theta_{UE}) + \mathbf{R}_{n+i} \tag{3.9}$$

where β_{UE}^2 is the received power at the array from the user of interest; $\mathbf{R}_{n+i} = \mathbf{R}_I + \sigma_n^2\mathbf{I}$ is the interference ($\mathbf{R}_I$) plus noise ($\sigma_n^2\mathbf{I}$) spatial covariance matrix at the antenna array.

3.3.1 Interference Statistical Model

It is realistic to assume that, while the DoAs of the users in the served cell are known (or separately estimated), the interference coming from the neighboring cell is available in terms of spatial covariance for the beamforming design at the BBU. Therefore, the covariance matrix for a set of interferers, characterized by a power β_k^2 received by the array and a DoA θ_k each, is known only in its expected value:

$$\mathbf{R}_I = \mathrm{E}\left[\sum_{k=1}^{M_I}\beta_k^2\mathbf{a}(\theta_k)\mathbf{a}(\theta_k)^H\right] \tag{3.10}$$

where the expectation is taken with respect to the random variables $\{\beta_k^2\}_{k=1}^{M_I}$ and $\{\theta_k\}_{k=1}^{M_I}$ used to describe each interferer. The received power $\beta_k^2 = 1/d_k^2$ accounts for the path loss as in (3.3). To obtain the expected value in (3.10), the first step is to derive the joint probability density function (pdf) $f(\beta^2, \theta)$ of the received power β^2 and DoA θ for one interferer uniformly distributed over the service area (see Fig. 3.4).

Considering randomly and uniformly distributed users within the cells, the pdf of the position of a user inside the cell is $f(x, y) = 1/\pi r^2$ for (x, y) inside the cell. The pdf of the DoA is, from the geometry:

$$f(\theta) \propto c(\theta) \tag{3.11}$$

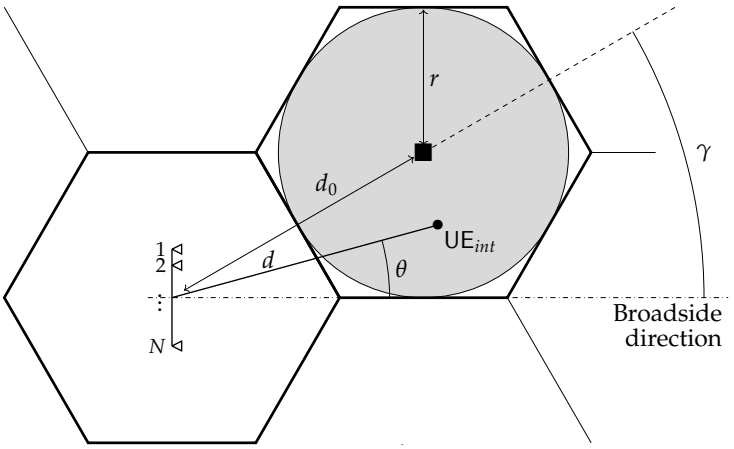

Figure 3.4: Geometric model for the statistical description of inter-cell interference.

where the chord $c(\theta)$ is

$$c(\theta) = 2r\sqrt{1 - \frac{d_0^2}{r^2}\sin^2(\gamma - \theta)} \tag{3.12}$$

The proportionality factor, to have $\int_\Theta f(\theta)d\theta = 1$ is

$$K = \frac{1}{\int_\Theta c(\theta)d\theta} \tag{3.13}$$

and Θ is the set of possible AoAs for the interferers, hence $\Theta = [\theta_{min}, \theta_{max}]$ where $\theta_{min}, \theta_{max} = \gamma \pm \arcsin(r/d_0)$. The conditional probability density function for the distance between the interferer and the array is:

$$f(\rho|\theta) = \frac{1}{c(\theta)} \tag{3.14}$$

Overall, the joint pdf for the distance and angular position is:

$$f(\rho, \theta) = f(\rho|\theta)f(\theta) = K = \frac{1}{\int_\Theta c(\theta)d\theta} \tag{3.15}$$

To obtain the joint pdf for received power and AoA, a change of variable is needed: $\beta^2 = g(\rho) = 1/\rho^2$. Therefore, since the transformation $g(\rho)$ is monotonic, the pdf is

$$f(\beta^2, \theta) = \left|\frac{\partial g^{-1}(\beta^2)}{\partial \beta^2}\right| f(g^{-1}(\beta^2), \theta) = \frac{1}{2\int_\Theta c(\theta)d\theta}\beta^{-3} = Z \cdot \beta^{-3} \tag{3.16}$$

The covariance matrix for M interferers is then:

$$[\mathbf{R}_I]_{m,n} = \mathrm{E}\left[\sum_{k=1}^{M} \beta_k^2 a_n(\theta_k) a_m^*(\theta_k)\right] \tag{3.17}$$

Under the assumption of $\lambda/2$-spaced uniform linear array, the expected value in (3.17) is:

$$[\mathbf{R}_I]_{m,n} = M \int_{\Theta} \int_{\beta^2_{min}(\theta)}^{\beta^2_{max}(\theta)} e^{j\pi(n-m)\sin(\theta)} Z\beta^{-1} d(\beta^2) d\theta \tag{3.18}$$

The first integral, in $d(\beta^2)$, is performed analytically, while the second, in $d\theta$, is solved numerically to obtain

$$\begin{aligned} &[\mathbf{R}_I]_{n,m} = \\ &2M \cdot Z \cdot \int_{\Theta} e^{j\pi(n-m)\sin(\theta)} \left[\frac{d^2_{max}(\theta) - d^2_{min}(\theta)}{d_{min}(\theta) d_{max}(\theta)}\right] d\theta \end{aligned} \tag{3.19}$$

where $\Theta = [\theta_{min}, \theta_{max}]$ is the support for the DoAs of the interferers, $d_{min}(\theta)$ and $d_{max}(\theta)$ are the minimum and maximum distances associated with a specific DoA and Z is the normalization factor in (3.16).

3.3.2 Performance Metrics

The performance degradation introduced by intermodal crosstalk is evaluated primarily in terms of SINR at the decision variable $\hat{s}$ for the user. SINR after beamforming, in the ideal case of transparent fronthauling, is:

$$\mathrm{SINR}_{ideal}(\theta_{UE}) = \frac{\sigma_s^2 |\mathbf{w}^H \mathbf{a}(\theta_{UE})|^2}{\mathbf{w}^H \mathbf{R}_{n+i} \mathbf{w}}. \tag{3.20}$$

For a non-ideal optical channel, the received signal at the beamformer is that of (3.5), and the optical channel matrix is included in the SINR expression accordingly:

$$\mathrm{SINR}(\theta_{UE}) = \frac{\sigma_s^2 |\mathbf{w}^H \mathbf{H}_{opt} \mathbf{a}(\theta_{UE})|^2}{\mathbf{w}^H \mathbf{H}_{opt} \mathbf{R}_{n+i} \mathbf{H}_{opt}^H \mathbf{w}}. \tag{3.21}$$

Performances are evaluated in terms of the wireless channel capacity

$$C(\theta_{UE}) = \log_2(1 + \mathrm{SINR}(\theta_{UE})). \tag{3.22}$$

Moreover, to gain insight into how the system performances scale with the antenna array dimension, an average capacity per user is also evaluated by averaging $C(\theta_{UE})$ over θ_{UE}.

3.4 Simulation Settings and Results

The performances of the proposed MDM/FDM-based fronthaul architecture are evaluated for the following scenario: uplink transmission is considered for a single user ($M_S = 1$), located in the area served by the antenna array ($\theta_{min} = -60°$, $\theta_{max} = 60°$). The cells have radius $r = 500$m and the interfering cell is at a distance $d_0 = 2r$, with angular position $\gamma = 30°$ with respect to the broadside direction of the array. Initially, the number of MDM channels is assumed to be equal to the number of antennas, i.e., no FDM is performed. First the SINR is evaluated varying the DoA of the user of interest to have a meaningful comparison with the performance offered by beamforming at the RRH (i.e., ideal fronthauling). In Fig. 3.5, the SINR(θ) is evaluated for all the possible permutations $\mathbf{P}$ in (3.6) of the reference optical channel $\mathbf{H}_{ref}$ (6 non-degenerate LP modes, PL MUX/DEMUX), highlighting the potential of optimal channel assignment. The SINR degradation experienced around $\theta = 30°$ is clearly due to the relative positions of antenna array, served user and interfering cell.

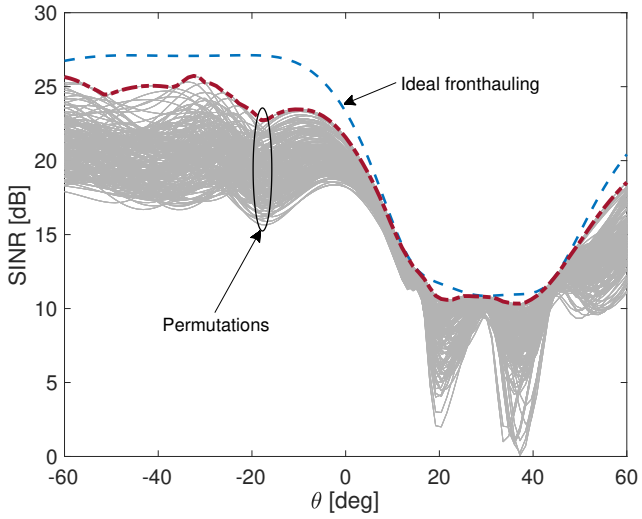

Figure 3.5: Effect of the optical channel assignment on the SINR.

The channel capacity $C(\theta)$, corresponding to SINR(θ), is then evaluated choosing the best optical channel assignment for each DoA. In Fig. 3.6, either only non-degenerate modes or all the available spatial modes are exploited in the MDM link. As explained in Section 3.2.2, pairs of degenerate modes result in fully-coupled channels: for this reason the channel matrix, if using all the available modes, presents reduced rank. Results in Fig. 3.6 confirm that the

use of a couple of degenerate modes makes the channel capacity comparable to the one obtained with a number of MDM channels equal to the matrix rank (and hence a lower number of antennas): the green dash-dotted line corresponding to eight MDM channels with two pairs of fully-coupled modes ($LP11_a$ - $LP11_b$ and $LP21_a$ - $LP21_b$) is close to the solid red line obtained using only the six non-degenerate modes out of the previous eight ($LP11_{a+b}$ and $LP21_{a+b}$).

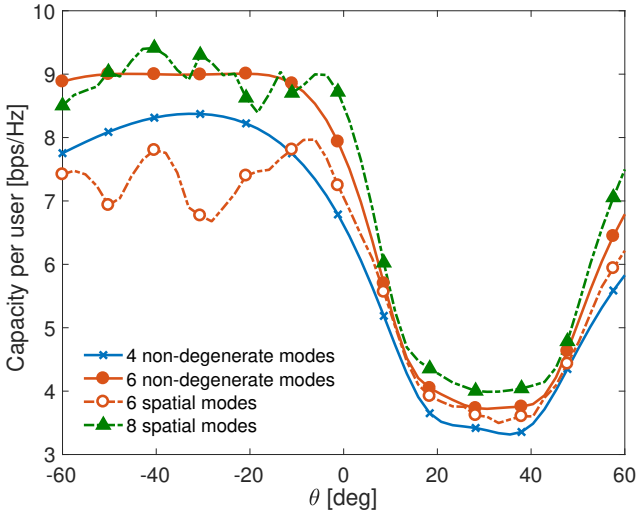

Figure 3.6: Capacity per user with MPLC MUX/DEMUX vs DoA θ_{UE} with non-degenerate modes (solid lines) and with spatial modes (dash-dotted lines).

It is therefore mandatory to implement an MDM system based only on non-degenerate modes to take full advantage of the spatial diversity provided by the RRH antennas. System performances are then evaluated considering only non-degenerate modes: LP01, $LP11_{a+b}$, LP02, $LP21_{a+b}$, $LP12_{a+b}$ and $LP31_{a+b}$. In Fig. 3.7 the two different technologies considered (MPLCs and PLs) are compared in terms of average capacity per user varying the number of antennas N. The solid lines are obtained without FDM, showing far better performances for MPLCs, approaching the ideal curves (dash-dotted) thanks to their higher mode selectivity with respect to PLs. Dashed lines refer to a joint MDM-FDM architecture with PL multiplexing, employing two frequency channels to serve the same number of antennas (i.e., $N/2$ modes per frequency), providing significant gain with respect to the single-frequency case and approaching the performance of ideal fronthauling.

So far, the average covariance matrix is considered in the SINR and in the

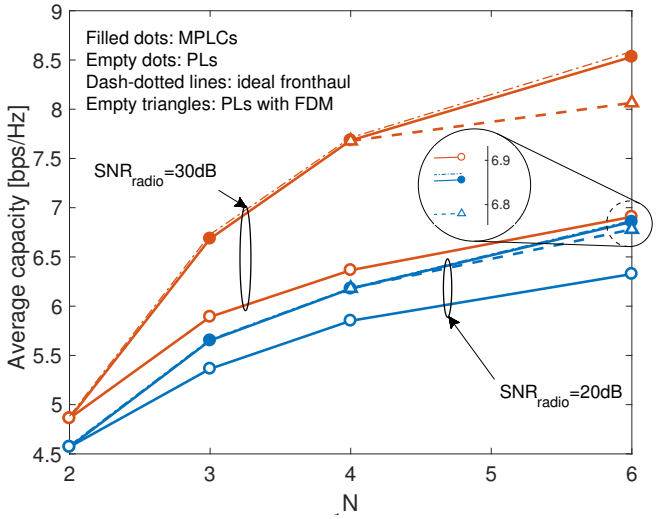

Figure 3.7: Average capacity vs number of antennas (modes) at 20dB and 30dB of radio-link SNR, 10-km fiber propagation.

corresponding capacity. It is however more realistic to assume asynchronous operation of the two neighboring cells in the considered scenario: instead of a fixed number of ever-active M_I interferers, the number of simultaneously active interfering users is a random variable, which is modeled as Poisson distributed with average M_I. In Fig. 3.8a (shown on the top of next page) the cumulative distribution function (CDF) for the capacity $C(\theta_{UE} = -40°)$ is shown for an average of $M_I = 6$ interfering users in the neighboring cell and the two considered multiplexing technologies after 1-km fiber propagation, together with the capacity obtained considering the average spatial interference covariance. Fig. 3.8b shows the capacity at 5% outage probability for all DoAs in the same settings.

Although the previous results are obtained for a single user and with a relatively small number of antennas (due to computational issues only), the model can be straightforwardly generalized to serve multiple users with a higher number of antennas. In this setting the size of the optimization problem for the optical resource allocation increases dramatically, following a $N!$ trend. Thus some more refined optimization technique based on integer programming needs to be developed. Since the optical FDM channels are mutually orthogonal, the overall channel matrix H_{opt} is sparse, as crosstalk is only between signal in the same FDM channel, which can be an advantage in terms of optimization efficiency. Moreover, in a realistic scenario multiple users are to be managed inside the cell: the resource allocation optimization

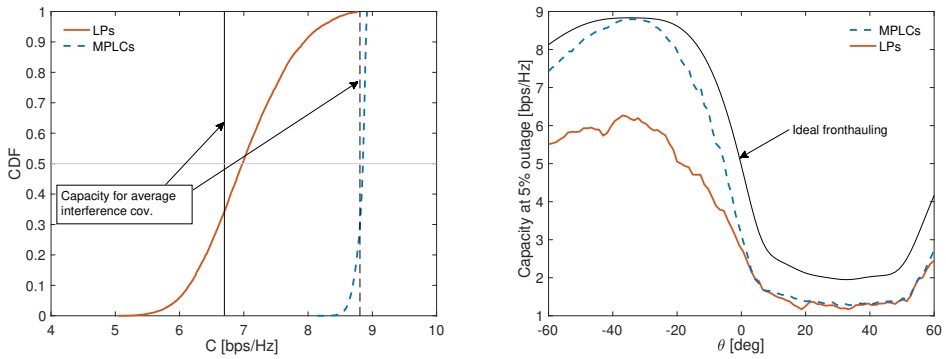

(a) Cumulative distribution function of $C(\theta_{UE} = -40°)$.

(b) Capacity at 5% outage probability vs θ.

Figure 3.8: CDF for $\theta_{UE} = -40°$ and capacity at 5% outage probability, $\text{SNR}_{\text{radio}} = 20\text{dB}$, $N = 6$ antennas and modes.

needs to be extended to multi-objective optimization, e.g., by considering the weighted sum rate or the minimum rate as objective function.

3.5 Resource Mapping for Massive Antennas Array

The optimal space-frequency to space-frequency (SF2SF) mapping of each antenna onto each mode and frequency can be found by solving a non-trivial integer programming optimization problem, whose complexity is $\mathcal{O}(N!)$. This is the number of possible permutations for a $N \times N$ matrix and the number of all possible SF2SF mappings. Exhaustive search is used in the previous results, but it is mandatory to adopt a sub-optimal but still effective resource allocation algorithm, especially when dealing with a massive number of antennas (say $N > 100$).

3.5.0.1 Hill-Climbing Approach for SF2SF Mapping

A suboptimal solution can be found through an iterative local search with relatively low computational cost. In general, the optimization problem set by the SF2SF mapping consists in defining an optimal mapping between the N radio signals from the antennas of the array and all the $N_s \cdot N_f \geq N$ available SF channels, where N_s is the number of space-defined channel (i.e., N_M in Section 3.2) and N_f the number of frequency bands. The problem is considered here in a simplified version, in which we assume that $N_s \cdot N_f =$

N and $N_s = 4$, to gain insight into the interplay between the crosstalk introduced by $\mathbf{H}_{SF}$ and the SF channel mapping. In particular, the hill-climbing approach [53] is used to find the (sub)optimal SF channel mapping based on a local search iterative algorithm, explained in the following and summarized in Algorithm 1. For any permutation, univocally defined by a vector $\mathbf{p} = [p_1, \ldots, p_N]^T$ as in Section 3.2, the set of all the neighboring permutations at a (integer) distance d_p is defined as the set of all vectors obtained permuting in any way all subset of d_p elements in $\mathbf{p}$, where the set of neighbors at distance d_p has cardinality $\binom{N}{d_p}$. The algorithm starts from an initial permutation $\mathbf{p}_0$ and updates the solution as follows: at the k-th step all the neighbors $\{\mathbf{p}_{near,k}\}$ at distance lower than or equal to d_p from the present solution $\mathbf{p}_{opt,k}$ are computed, together with the corresponding SINR values. The best neighbor $\mathbf{p}_{near,k}^{best}$ is compared to $\mathbf{p}_{opt,k}$ in terms of associated SINR: if the best neighbor has greater SINR with respect to $\mathbf{p}_{opt,k}$ the solution is updated to $\mathbf{p}_{opt,k+1} = \mathbf{p}_{near,k}^{best}$ and another iteration is performed, otherwise the final solution is $\mathbf{p}_{opt,k}$. The number of iterations N_{it} needed to reach the solution is proportional to the dispersion of the solution set (i.e., high dispersion means that there is room for channel assignment optimization), while the computational complexity needs also to take into account the fact that, at each iteration, an exhaustive search over the neighboring solutions is performed. The hill-climbing algorithm is clearly suboptimal as it will select as solution the first local maximum for the SINR, but the performances are close to the exhaustive $\mathcal{O}(N!)$ search as shown in [33,54].

Hill-Climbing Computational Complexity

The hill-climbing algorithm should be run for each UEs configuration, and its computational complexity can be measured by the total number of times, denoted by K, that the specific objective function (e.g., SINR in Algorithm 1) needs to be evaluated in order to reach the solution. In the case of the SF2SF multiplexing by exhaustive search, for example, it corresponds to the total number of possible reference channel permutations: $K_{\text{ex}} = N!$. The computational complexity of the hill-climbing algorithm needs to account for the fact that, for each of the N_{it} hill-climbing iterations, an exhaustive search over all the neighboring permutations must be performed according to the neighboring distance d_p and the cardinality of the neighboring permutations set K_{d_p}:

$$K_{d_p} = \sum_{n=2}^{d_p} \binom{N}{n} \cdot !n, \tag{3.23}$$

Algorithm 1 Iterative hill-climbing algorithm for (sub)optimal SF2SF mapping

1. Input: radio scenario parameters, MMF characteristics, max. neighbor distance d_p;
2. Initialize $\mathbf{p}_0$ and compute $\mathrm{SINR}(\mathbf{p}_0)$;
3. **while** $\mathrm{SINR}(\mathbf{p}_{best,k}) > \mathrm{SINR}(\mathbf{p}_{best,k-1})$
   (a) compute neighboring permutations $\{\mathbf{p}_{near,k}\}$ at distance $d \leq d_p$ from $\mathbf{p}_{best,k-1}$;
   (b) $\mathbf{p}_{best,k} = \arg\max_{\mathbf{p}} \mathrm{SINR}(\mathbf{p}_{near,k})$;
4. **end while**
5. Output: $\mathbf{p}_{best,k}$.

where $!n = n! \cdot \sum_{i=0}^{n} \frac{(-1)^i}{n!}$ is known as *derangement number* or *de Montmort number*, which is defined as the number of permutations of the elements of a set, such that no element appears in its original position. Then, the overall computational complexity is obtained as

$$K = K_{d_\pi} \cdot N_{\mathrm{it}}. \tag{3.24}$$

3.6 Concluding Remarks

The implementation of a joint MDM-FDM based fronthauling has been proposed to allow cost-effective and bandwidth-efficient connections between massive antenna arrays and centralized BBUs. Direct detection is the key for cost reduction and energy efficiency, at the price of a reduction in the number of available mode channels due to the presence of degenerate modes. Realistic measured performance of all-optical passive (de)multiplexers as PLs and MPLCs available on the market or described in literature have been taken into account, showing that the employment of degenerate LPxya and LPxyb modes (at the same propagation constant) does not assure extra capacity per user with respect to the exploitation of non-degenerate modes only. A statistical interference model has been developed to consider a realistic radio scenario, and MVDR beamforming (transparent to the optical channel) has been considered to evaluate the impact of intermodal crosstalk. Numerical results prove that the use of dynamic assignment for the mode-frequency optical resources allows to overcome the crosstalk limitations and to approach the ideal performances, thus enabling C-RAN based on the joint exploitation MDM-FDM even without conventional solution for intermodal crosstalk mitigation relying on coherent detection and optical- MIMO processing. Results are expanded also to multiple users and huge antenna arrays.

Chapter 4

Beamforming Split and Hybrid Beamforming

Contributions

The aim of this Chapter is the integration between hybrid beamforming for the mmWaves and analog fronthauling. In particular, analog processing is at the remote antenna site and digital spatial filtering is at the centralized baseband unit, with analog fronthauling based on analog radio-over-fiber. A method is provided to design the analog phase-only optical beamformer to be implemented at the remota antennas. The performance of the proposed architecture is evaluated considering a realistic uplink radio scenario.

Organization

The need for hybrid analog/digital beamforming processing for the millimeter wave radio channel is motivated in Section 4.1. Section 4.2 introduces the system model for the radio scenario and the beamforming strategy adopted here. Section 4.3 describes the rationale followed in the design of the analog and digital beamformers and numerical results are provided in Section 4.4. Concluding remarks are in Section 4.5.

4.1 Introduction

The ever-growing demand in network capacity is fueling the evolution of radio access networks towards higher carrier frequencies, and future generation networks (5G and beyond) will most likely exploit the millimeter wave (mmWave) spectrum above 30 GHz, to guarantee higher bandwidth and to avoid the crowded region below 6 GHz [18]. Massive number of antennas

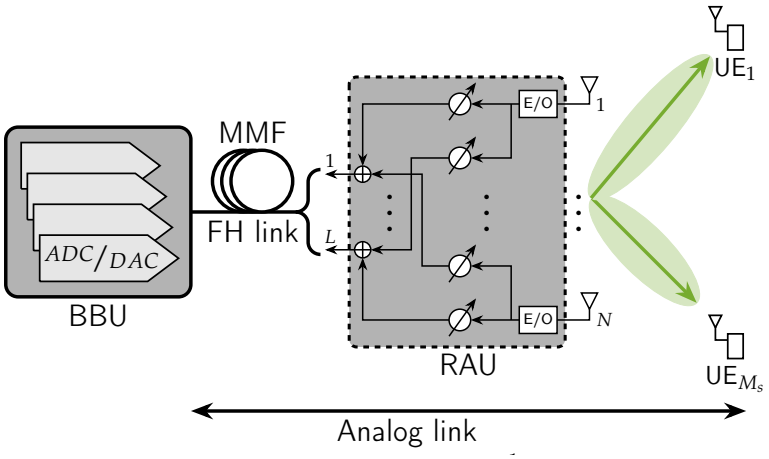

Figure 4.1: Beamforming split in MDM-based C-RAN.

is mandatory in mmWave communication mostly for power budget, as the high-frequency carriers employed in mmWave radio reflect onto an orders-of-magnitude increase in free-space loss. At the same time, the decrease in wavelength enables packing a large number of antennas (say > 100) into small form factors, so that physically small arrays with massive numbers of antennas can provide the beamforming gain needed to overcome the increased path-loss attenuation. Conventionally, beamforming is performed digitally at the baseband and this would require one analog/digital converter for each antenna element, which is unfeasible for cost and energy consumption. Hybrid analog-digital precoding/combining has been proposed to address these issues [19], making use of phase shifters or delay elements such as optical ring resonators (ORRs) for analog processing to reduce the number of required digital streams [20,21]. Analog beamforming is also suitable for providing a preliminary broadband processing, pivotal in a mmWave scenario with signal bandwidths around 800 MHz, before the narrowband completion of the spatial filtering in the digital domain.

In this Chapter we propose the integration of analog fronthauling and hybrid beamforming: the RAUs perform analog signal processing and signal relaying towards the BBUs, which provide analog/digital conversion and baseband digital processing. The whole link between the BBU and the mobile user equipments (UEs) is fully analog as in Fig. 4.1, mixing radio and optics.

Analog fronthaul can be based on the analog radio over fiber (A-RoF) paradigm, due to its capability to carry several Gbit/s in terms of equivalent data rate [10]. However, the required bandwidth scales with the number of antennas at the RAU that can be huge if considering the mmWave spectrum.

In this scenario, the huge bandwidth provided by the optical link could be even not enough, calling for the need of a new multiplexing dimension. In Chapter 3, we considered that mode division multiplexing (MDM) can overcome the bandwidth limitations of RoF architecture by taking advantage of the different propagation modes of light on fiber, with a key benefit lying in the colorlessness of an MDM-based architecture, that improves its cost effectiveness with respect to conventional wavelength division multiplexing (WDM).

In this Chapter, to gain insight into the effects of beamforming split, fronthauling is deemed to provide perfect transport of the fronthaul signal and narrowband processing is considered: analog processing is assumed to be performed by phase shifters. System performance evaluation is carried out for a sample scenario in which beamforming is performed jointly by a RAU and the corresponding BBU to separate the useful uplink signals of served users from interference arising from neighboring hot-spots or other users (e.g., those served by a different operator).

4.2 System Model

Here we consider a C-RAN based on all-analog fronthauling, and in particular we focus on beamforming to separate uplink signals of M users served by a specific RAU (downlink would be similar, not covered here). Beamforming is split between an analog processing at the RAU and a baseband digital processing at the BBU to achieve both a signal compression before the fronthauling and to reduce the number of necessary analog/digital converters at the BBU.

The analog signals received at the RAU by N antennas are partially processed by an analog combiner $\mathbf{\Phi}$ and then relayed through $L \leq N$ fronthaul channels (possibly mutually interfering) towards the BBU, where beamforming is completed by baseband digital processing. The estimated users' signals at every sample interval are collected in the $M \times 1$ vector $\hat{\mathbf{s}}$, described by

$$\hat{\mathbf{s}} = \mathbf{B}\mathbf{H}_{fh}\mathbf{\Phi}(\mathbf{H}_r\mathbf{s} + \mathbf{n}), \tag{4.1}$$

where the matrices $\mathbf{B} \in \mathbb{C}^{M\times L}$, $\mathbf{H}_{fh} \in \mathbb{C}^{L\times L}$, $\mathbf{\Phi} \in \mathbb{C}^{L\times N}$ and $\mathbf{H}_r \in \mathbb{C}^{N\times M}$ are respectively the digital baseband beamformer, the optical fronthaul channel (assumed to be $\mathbf{H}_{fh} = \mathbf{I}$ throughout this Chapter but not necessarily), the analog RF beamformer and the radio channel shown in Fig. 4.2 and detailed below. In particular, being analog beamforming performed by phase shifters or delay elements, each element of the matrix $\mathbf{\Phi}$ has unit amplitude: $[\mathbf{\Phi}]_{\ell,n} = \exp(j \cdot \alpha_{\ell,n})$. Vector $\mathbf{s}$ contains signals for the M users of interest,

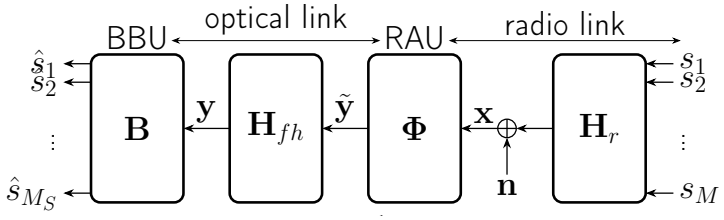

Figure 4.2: System model (uplink).

and $\mathbf{n}$ is the interference plus noise at the antenna array. Fronthauling noise is neglected (or small and included into the term $\mathbf{n}$).

4.2.1 Radio Channel

The base-band equivalent signals received by the N antennas at the RAU, arranged in a vector, are:

$$\mathbf{x} = \mathbf{H}_r \mathbf{s} + \mathbf{n} \tag{4.2}$$

where $\mathbf{s} \in \mathbb{C}^M$ collects the signals with power σ_s^2 transmitted by all the M users with single-antenna and assumed to be Gaussian distributed: $\mathbf{s} \sim \mathcal{CN}(\mathbf{0}, \sigma_s^2 \mathbf{I})$. $\mathbf{H}_r \in \mathbb{C}^{N \times M}$ is the wireless channel matrix and $\mathbf{n} \sim \mathcal{CN}(\mathbf{0}, \mathbf{R}_n)$ is the $N \times 1$ noise vector that is spatially structured according to the interference pattern. A spatially sparse channel is assumed for its suitability in modeling the mmWave propagation [18]. In particular, the channel model is based on the far field approximation and it accounts for the directions of arrival (DoAs) of the signals assuming only line-of-sight (LOS) propagation:

$$\mathbf{H}_r = \begin{bmatrix} \beta_1 \mathbf{a}(\theta_1) & \beta_2 \mathbf{a}(\theta_2) & \cdots & \beta_M \mathbf{a}(\theta_M) \end{bmatrix} \tag{4.3}$$

where $\beta_k \sim \mathcal{CN}(0, 1)$ accounts for Rayleigh fading (expansion to Rician fading [55] is straightforward) and $\mathbf{a}(\theta_k) \in \mathbb{C}^N$ is the steering vector for the direction of arrival (DoA) θ_k of the k-th user. Under the assumption of $\lambda/2$-spaced uniform linear array (ULA) at the RAU, the array response for the k-th user is $\mathbf{a}(\theta_k) = \begin{bmatrix} 1 & e^{j\pi \sin(\theta_k)} & \ldots & e^{j\pi(N-1 \sin(\theta_k)} \end{bmatrix}^T$. It is assumed here that the transmit power σ_s^2 is the same for all users, and normalized to one, so that the received power for the k-th user depends only on the Rayleigh fading, i.e., it is a chi-squared distributed random variable with two degrees of freedom $\beta_k^2 \sim \chi_2^2$. The signal covariance matrix is then

$$\mathbf{R}_s = \sum_{k=1}^{M} \beta_k^2 \mathbf{a}\left(\theta_k\right) \mathbf{a}^H\left(\theta_k\right) . \tag{4.4}$$

Here interference is assumed to come from M_I users, thus the structure of the covariance $\mathbf{R}_n$ is similar to (4.4).

4.2.2 MMSE Beamforming

Ideally, beamforming should act directly on the signals received by the antennas, to give

$$\hat{\mathbf{s}} = \mathbf{W}\mathbf{x}\,, \tag{4.5}$$

where $\mathbf{W} = \begin{bmatrix}\mathbf{w}_1 & \mathbf{w}_2 & \cdots & \mathbf{w}_M\end{bmatrix}^H$ is the beamforming matrix and $\mathbf{w}_k^H$ is the spatial filter for the k-th user. Linear minimum mean square error (MMSE) beamforming is considered here to separate the M uplink signals [56]. Assuming known channels for all the users according to (4.3), the MMSE beamformer can be written (up to a scale factor) as

$$\mathbf{W} = \mathbf{A}^H(\boldsymbol{\theta})\mathbf{R}_x^{-1}\,, \tag{4.6}$$

where $\mathbf{R}_x = \mathbf{R}_s + \mathbf{R}_n$ is the covariance matrix for the overall signal $\mathbf{x}$ received at the antennas and the columns of the matrix $\mathbf{A}(\boldsymbol{\theta}) = \begin{bmatrix}\mathbf{a}(\theta_1) & \mathbf{a}(\theta_2) & \cdots & \mathbf{a}(\theta_M)\end{bmatrix}$ contains the array responses for the DoAs of the users.

4.2.3 Performance Metrics

Signal to interference plus noise ratio (SINR) at the decision variable $\hat{\mathbf{s}}_k$ for the k-th user is given by:

$$\mathrm{SINR}_k\left(\mathbf{W}\right) = \frac{\left|\mathbf{w}_k^H\mathbf{a}\left(\theta_k\right)\right|^2}{\mathbf{w}_k^H\mathbf{R}_n\mathbf{w}_k}\,. \tag{4.7}$$

Performances are evaluated in Section 4.4 in terms of average per-user capacity, defined as

$$C_{\mathrm{mean}} = \frac{1}{M}\sum_{k=1}^{M}\log_2\left(1+\mathrm{SINR}_k\left(\mathbf{W}\right)\right)\,. \tag{4.8}$$

When considering a non-ideal fronthaul transport and/or a beamforming split between analog and digital processing, the whole chain composed by analog combiner, fronthaul channel and digital beamformer needs to be taken into account into an equivalent spatial filter

$$\mathbf{W}_{eq} = \mathbf{B}\mathbf{H}_{fh}\mathbf{\Phi} \tag{4.9}$$

to be used instead of $\mathbf{W}$ in (4.7) and (4.8) for performance evaluation.

4.3 Beamforming Split

Spatial sparsity of the mmWave radio channel is the key feature that allows fronthaul compression through analog processing. MMSE beamforming is based on the spatial covariance $\mathbf{R}_x$ of the signals received at the antennas and $\mathbf{R}_x$, in the considered radio scenario, is reduced-rank as it contains only $L_{min} < N$ significant eigenvalues, which are related to the received rays. Therefore, at the RAU one could project the received signal $\mathbf{x}$ onto the first $L_{\min}$ eigenvectors of $\mathbf{R}_x$ and relay only these $L_{\min}$ streams towards the BBU, still achieving the ideal performance. However, analog beamforming is implemented by phase shifters, or delay elements, and therefore this technological choice imposes a phase-only processing.

4.3.1 Phase-only Approximation of Spatial Filter

Let us consider the approximation of a spatial filter $\mathbf{f}$ with a phase-only vector $\boldsymbol{\phi}$ given by the transformation $\mathcal{P}(\mathbf{f}) = \boldsymbol{\phi}$. Such transformation is defined as the maximization of the projection of $\boldsymbol{\phi}$ onto $\mathbf{f}$, that in turn is equivalent to the maximization of the inner product $\mathbf{f}^H\boldsymbol{\phi}$ since the amplitude of the entries of $\boldsymbol{\phi}$ is fixed. Considering the square value of the projection, the problem is equivalent to maximizing the quadratic form $\boldsymbol{\phi}^H\mathbf{F}\boldsymbol{\phi}$, where $\mathbf{F} = \mathbf{f}\,\mathbf{f}^H$:

$$\begin{aligned} \hat{\boldsymbol{\phi}} = \mathcal{P}(\mathbf{f}) = & \arg\max_{\boldsymbol{\phi}} \boldsymbol{\phi}^H\mathbf{F}\boldsymbol{\phi} \\ & \text{s.t.} \quad \boldsymbol{\phi}_i = \exp(j\boldsymbol{\alpha}_i) \end{aligned} \tag{4.10}$$

Solution to problem (4.10) is $\boldsymbol{\phi}_i = \exp(j\angle\mathbf{f}_i)$, where $\angle\mathbf{f}_i$ denotes the phase of the i-th element of vector $\mathbf{f}$. A sample result is shown in Fig. 4.3, where the considered scenario contains one user of interest ($M = 1$) and one interferer that is located at the same distance from the array with DoAs $\theta_{UE} = 0$ and $\theta_I = 20\,\text{deg}$, respectively. The black solid line is the gain versus DoA of the MMSE filter, while the blue dashed line represents the gain of the phase-only approximation of the MMSE beamformer. It is clear from Fig. 4.3 that the phase-only representation of the MMSE beamformer, whilst preserving the main lobes, fails in providing adequate interference rejection. The red dash-dotted line, on the other hand, gives a better approximation of the interference rejection of the ideal MMSE beamformer. It represents the result of the hybrid beamforming described in the following Section 4.3.2.

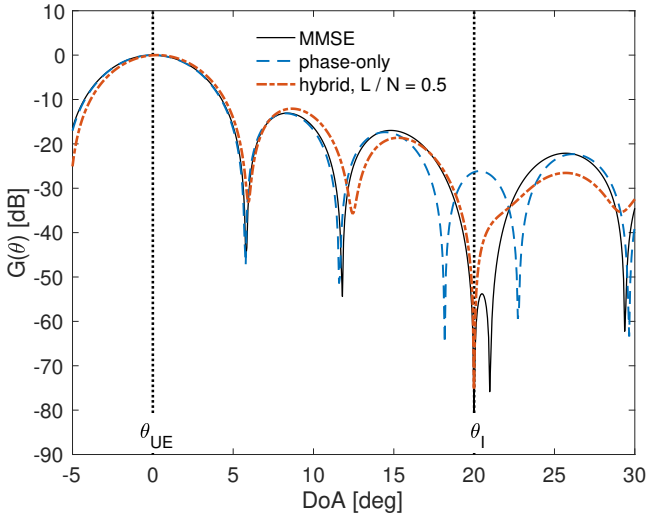

Figure 4.3: Gain versus θ for the MMSE beamformer (solid line), for its phase-only approximation (dashed line) and for the hybrid solution with $L = N/2$ (dash-dot line).

4.3.2 Hybrid Beamforming

The proposed hybrid beamforming consists of implementing at the RAU an analog processing, represented by matrix $\mathbf{\Phi} = \begin{bmatrix} \boldsymbol{\phi}_1 & \boldsymbol{\phi}_2 & \cdots & \boldsymbol{\phi}_L \end{bmatrix}^H$, which gives the projection of the received signal $\mathbf{x}$ onto the phase-only approximation through $\mathcal{P}(\cdot)$ from (4.10) of the first $L < N$ eigenvectors of the covariance matrix $\mathbf{R}_x$. MMSE beamforming is then completed at the BBU by a second (digital) beamformer $\mathbf{B}$. Let us consider the eigenvalue decomposition of $\mathbf{R}_x$ as

$$\mathbf{R}_x = \mathbf{U}\mathbf{\Lambda}\mathbf{U}^H , \tag{4.11}$$

in which $\mathbf{\Lambda} = \text{diag}(\lambda_1, \ldots, \lambda_N)$ collects the eigenvalues of the covariance $\mathbf{R}_x$, ordered by decreasing absolute value, and the matrix $\mathbf{U} = \begin{bmatrix} \mathbf{u}_1 & \mathbf{u}_2 & \cdots & \mathbf{u}_N \end{bmatrix}$ gathers the corresponding eigenvectors. The analog beamformer $\mathbf{\Phi}$ is such that

$$\boldsymbol{\phi}_\ell = \mathcal{P}(\mathbf{u}_\ell) \qquad \ell \in [1, L] . \tag{4.12}$$

In designing the MMSE digital beamformer $\mathbf{B}$, an equivalent channel $\mathbf{H}' = \mathbf{\Phi}\,\mathbf{A}(\boldsymbol{\theta})$ needs to be considered for the users. The covariance of the signal received at the BBU is then

$$\mathbf{R}'_x = \mathbf{\Phi}\mathbf{R}_x\mathbf{\Phi}^H \tag{4.13}$$

and MMSE beamforming is completed by

$$\mathbf{B} = \mathbf{A}^H(\boldsymbol{\theta})\,\boldsymbol{\Phi}^H \mathbf{R}'^{-1}_x\,. \tag{4.14}$$

Due to the unavoidable misalignment between the eigenvectors of $\mathbf{R}_x$ and their phase-only approximation (4.12), projection onto the subspace spanned by the phase approximation of the first $L_{\min}$ eigenvectors cannot capture all the useful information content of the signal, and projection onto a higher-dimensional subspace is needed. It is shown in Section 4.4 that, although only with $L = N$ streams perfect users' separation can be performed, negligible performance degradation is introduced by the proposed hybrid MMSE beamforming.

4.4 Simulation Settings and Results

A sample scenario is considered here for numerical evaluation of the proposed hybrid beamforming technique, in which $M = 3$ users are in the coverage area of the considered array, together with $M_I = 2$ interferers. All the $M + M_I$ sources are supposed to be at the same distance from the array and their angular position is shown in Fig. 4.4, where the polar representation of MMSE beamforming gain for the users of interest is given, together with the DoAs of the interferers, for $N = 20$ antennas at the RAU. In such reference

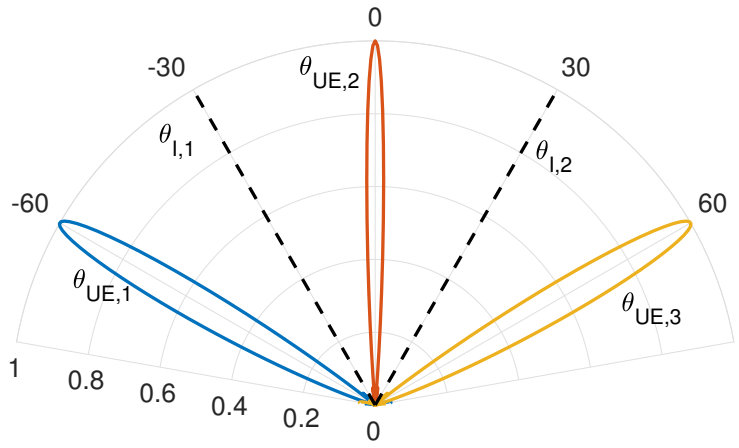

Figure 4.4: Sample scenario, polar representation of MMSE beamforming gain versus θ for $N = 20$ antennas at the array.

scenario, where the rank of channel $\mathbf{H}_r$ is $L_{\min} = M + M_I = 5$, the average per-user capacity is evaluated for different number of antennas N and for

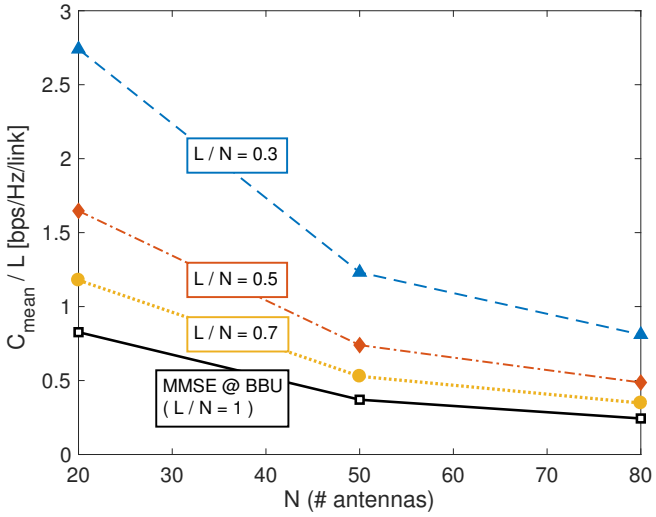

Figure 4.5: Average per-user capacity [bps/Hz] normalized with respect to the number L of fronthaul links versus N (SNR $= 40\,\mathrm{dB}$).

different number of fronthaul links L, parametrized by the L/N ratio which indicates the fronthaul compression and hardware simplification achieved.

An air-link SNR $= 40$ dB is considered here and, due to the clear spatial separation between targets and interferers, the experienced SINR at the decision variable $\hat{s}_k$ for each user of interest depends on the beamforming gain and it is approximately $\mathrm{SINR}_{\mathrm{dB},k} = 40 + 10\log_{10} N$. The corresponding average per-user capacity is $C_{\mathrm{mean}} \approx \log_2\left(N \cdot 10^4\right)$ consistently with the results presented in this section.

The performance of hybrid beamforming is evaluated in terms of average per-user capacity, normalized with respect to the number L of employed fronthaul links ($\overline{C} = C_{\mathrm{mean}}/L$) to consider the cost of fronthauling and BBU hardware into the chosen performance metric. The normalized average per-user capacity is shown in Fig. 4.5 versus the number of antennas at the RAU and for different values of the L/N ratio to highlight the gain obtained when few fronthaul links are employed (i.e., $L \ll N$).

On the other hand, a small value for the compression ratio L/N implies the introduction of a performance degradation due to incomplete description of the antenna signal when it is projected onto the phase-only basis provided by $\mathbf{\Phi}$. Such degradation introduced by hybrid beamforming is evaluated in terms of percentage loss in average per-user capacity for the reference scenario. In Fig. 4.6a the percentage loss is shown versus the L/N ratio for $N \in \{20, 50, 80\}$ showing no degradation (but also no fronthaul/hardware

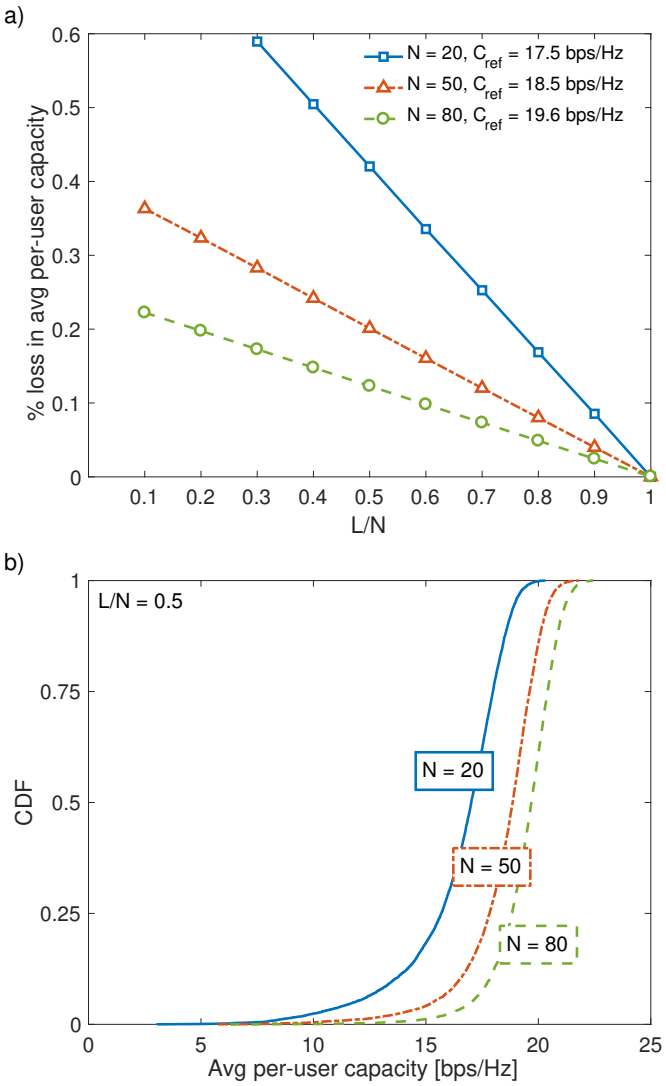

Figure 4.6: a) Loss in average per-user capacity for hybrid beamforming with respect to digital beamforming versus L/N ratio for different numbers of antennas (N). b) CDF of the average per-user capacity for half the optical links compared to N and varying N (SNR = 40 dB). C_{ref} indicates the average per-user capacity for $L = N$.

compression) at $L/N = 1$. The cumulative distribution function (CDF) of the average per-user capacity is shown in Fig. 4.6b for $L/N = 0.5$: since the left tails are fatter than the right tails, the probability distribution of C_{mean} presents negative skewness, more evident for low number of antennas.

4.5 Concluding Remarks

Beamforming split between analog RF processing at the antenna site and digital baseband processing at the BBU has been proposed for A-RoF analog fronthauling as a means to reduce the number of required fronthaul links and of analog-digital converters at the BBU for energy and cost effectiveness. The phase-only approximation of the spatial filter has been considered and its effectiveness has been tested. The proposed hybrid analog-digital MMSE beamforming leverages on the spatial sparsity of the mmWave radio channel and it is based on the phase-only approximation of the first L eigenvectors of the covariance matrix of the signal received by the antenna array. Its performance is compared to that of reference digital beamforming performed at the RAU varying the number of antennas and the number of analog streams relayed towards the BBU showing negligible losses and improved fronthaul efficiency for an example radio scenario. Broadband analog beamforming at the RAU is enabled by optical beamforming and it is left as topic for future research.

Chapter 5

Adaptive Hybrid Beamforming in Analog Fronthauling

Contributions

The concept of joint hybrid beamforming for the millimeter waves and analog fronthauling is developed starting from Chapter 4. In this chapter analog broadband processing at the remote antenna unit is based on optical ring resonators to build delay lines, and digital narrowband processing at the baseband unit completes the beamforming. Tunability of the delay response is considered with reference to the specifications of the 5G new radio. Typical tunability of optical devices is proved to introduce a significant performance degradation due to transient in the delay response of optical delay lines. Suitable scheduling of mobile users and digital precompensation are shown to effectively counteract the negative effect of the transient in delay response.

Organization

This chapter is organized as follows: hybrid beamforming is introduced in Section 5.1, where the call for adaptive response of the beamformer is introduced. Section 5.2 introduces the system model describing the radio scenario and the hybrid beamforming architecture. Hybrid beamformer design is dealt with in Section 5.3 and Section 5.4 revises the properties of OSP delay lines based on ring resonators, and describes the specific architecture used in this Chapter. Numerical performance evaluation is in Section 5.5, with a focus on the performance degradation introduced by reconfiguration of optical beamforming and on countermeasures. Conclusions are drawn in Section 5.6.

5.1 Introduction

In the context of mmWaves radio access, hybrid beamforming is mandatory to deal with the large bandwidths and the massive antenna arrays at hand. In particular, the integration of optical analog fronthauling and hybrid beamforming (BF) is appealing since optical analog signal processing can provide a wideband processing stage at the remote antenna unit (RAU), paired with narrowband digital processing at the BBU: analog signal processing and forwarding is performed at the RAU, which is connected through analog FH to the BBU where analog/digital conversion is performed, together with digital signal processing. In this work hybrid BF (HBF) with analog optical signal processing at the RAU and A-RoF FH is considered: optical signal processing (OSP) allows to build compact delay lines that in turns empower the wideband analog beamforming [21,57] that avoids the beam squint issue incurred when using RF phase shifters for analog processing. An algorithm based on the matching-pursuit paradigm for the design of the hybrid beamformer is proposed and validated, both for a fully connected architecture and for subarray processing.

Static configurations at RAU are widely demonstrated in literature [21, 57,58], but practical beamformers need to be reconfigured with a temporal dynamic that depends on the wireless channel or multiuser scheduling and this requirement can be faster than the adaptation rate of optical circuits. In particular, tunability of OSP-based analog BF is investigated here by taking into account 5G NR specifications [59], and assuming a joint space-time-frequency multiplexing of radio signals to/from multiple distinct users. Since slow tunability response of the optical components yields to performance degradation for typical 5G dynamics, different approaches to solve this issue are proposed from a system-level point of view.

It is to be noticed that the analysis is general for a digital fronthauling architecture, where optical signal processing at the RAU is paired with a CPRI interface. In this case the RAU includes the analog/digital converters from the BBU with some architectural overhead for the additional electro/optic conversions.

5.2 System Model

The FH system is based on A-RoF with ORR delay lines providing the capabilities to employ the analog beamforming at the RAU. Referring to uplink, the RF signal at each antenna element is converted to the optical domain (either employing multiple directly-modulated lasers or one continuous-

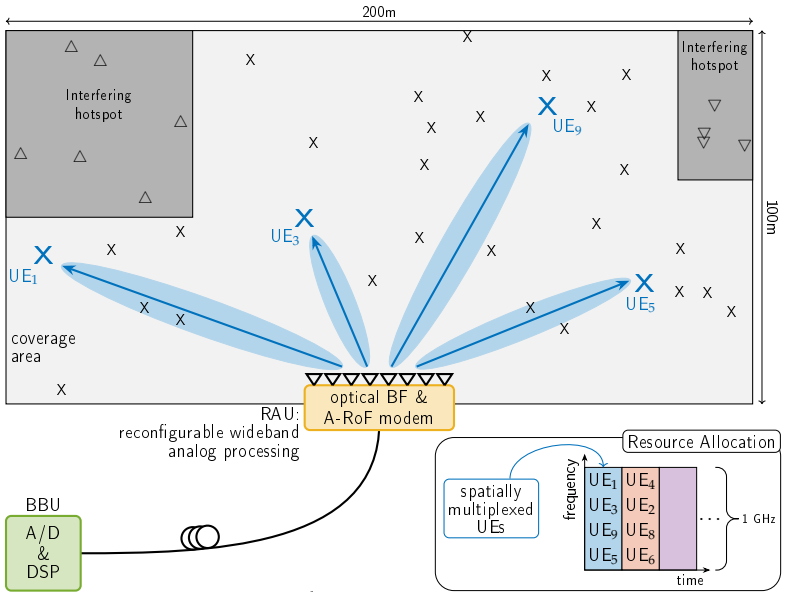

Figure 5.1: Coverage area geometry for the proposed system.

waveform optical source paired with multiple Mach-Zehnder modulators, see, e.g., [60]) and processed via OSP to obtain the spatially compressed FH signal that is transmitted towards the BBU. In particular, optical ring resonators are used to provide true time delay elements for all-optics delay-and-sum beamforming at RAU. Spatial filtering is then completed at the BBU by means of digital processing.

5G NR specifications [59] – valid for the $1 - 100$ GHz radio frequency spectrum – are taken into account: the Orthogonal Frequency Division Multiplexing (OFDM) radio signals present a 60-kHz subcarrier spacing corresponding to a symbol duration of $17.84\,\mu$s, and each time slot can include either 7 or 14 OFDM symbols, corresponding to a duration of 125 or 250 μs respectively. User density up to 1 device/m^2 is the target for 5G, here a less extreme scenario is considered, with $S = 504$ users on a $\sim 17000\,\mathrm{m}^2$ area shaped as in Fig. 5.1.

The system considered here is for broadband radio access signals: UEs are distributed within a coverage area as in Fig. 5.1, and they transmit RF signals within a bandwidth $B_w = 1$ GHz centered in $f_{RF} = 30$ GHz. Even if typical mmWave array at RAU is planar (or cylindric), the arrangement here is for uniform linear array (ULA) with N antennas spaced $d = \lambda_{min}/2$ apart to ensure correct spatial sampling of any signal of interest ($\lambda_{min} = 3 \cdot 10^8 / (f_{RF} + B_w/2)$).

It is assumed here that the system serves a pool of S single-antenna users

over a sparse directional channel [18], with joint time-frequency-space multiplexing on the air link. In particular, the whole 1-GHz bandwidth is assigned to all the users to provide a worst-case scenario in which all the UEs allocated within the same time slot are space-multiplexed by multi-beamforming and interfere with each other. The UEs served in the same resource block (RB) are M out of S, and are angularly (i.e., spatially) separated for the beamforming capability. A spatial scheduling policy needs then to be established to select those M UEs out of S to be minimally mutual interfering within the RB. In this work a sectorial approach is used to separate the S UEs into groups of M: the coverage area is divided into M angular sectors so that the number of users in each sector is the same, and one UE from each sector is allocated to each time slot following an increasing DoA ordering within each sector as specified in the following. The S DoAs are ordered and separated into M equinumerous segments of S/M UEs each (i.e., $\theta_1 < \theta_2 < \cdots < \theta_{S/M}$ form the first subset, $\theta_{S/M+1} < \cdots < \theta_{2S/M}$ form the second subset etc.) and the k-th UEs of the M segments are assigned to the k-th RB (time slot in this case). This is to guarantee both a good angular separation between spatially multiplexed UEs served in the same RB and a limited change in analog beamforming when switching from a RB to the next, as specified in Section 5.5.3.

ORR delay lines are employed for analog spatial filtering at the RAU to transform the N antenna signals into $L < N$ FH signals in uplink (UL), and viceversa in downlink (DL). As detailed in Section 5.4, ORRs have delay responses that are periodic in frequency, with period determined by the optical size of each ring (i.e., the physical dimensions and the refractive index) and typically referred to as free spectral range (FSR). A 60-GHz FSR is chosen for the compactness of the optical delay lines and to guarantee the flexibility in designing the A-RoF link since it matches the central frequency of the RF signal as in Fig. 5.2. In Fig. 5.2 optical double sideband modulation (ODSM) is considered [10], but the reasoning can easily be adapted to other A-RoF techniques. The fronthaul link is ideal so that no additional noise enters the system and there is no mutual interference among the L fronthaul channels.

5.2.1 Signal and Processing Description

The proposed architecture is represented in Fig. 5.3 and the corresponding linear system model for a narrowband description is detailed in Fig. 5.4 for the downlink (a) and uplink (b). Analog broadband processing at the RAU provides a spatial compression $N \to L$ ($\mathbf{W}_{RF}$, for UL) or decompres-

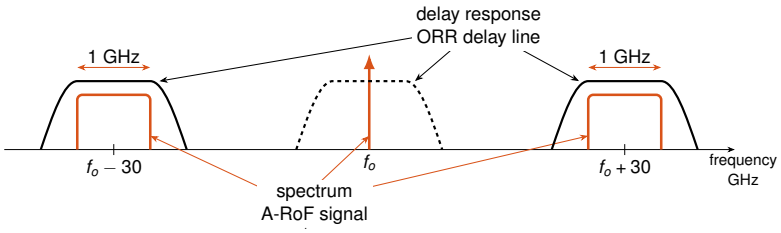

Figure 5.2: A-RoF fronthaul signal spectrum (red, solid line) and ORRs delay response (black, solid line for FSR = 60 GHz, also dashed line if FSR = 30 GHz).

sion $L \to N$ ($\mathbf{F}_{RF}$, for DL) of the whole RF signal. At the BBU, narrowband digital processing ($\mathbf{W}_{BB}$ for UL and $\mathbf{F}_{BB}$ for DL) performs spatial filtering on sub-bands of the radio signal of interest as shown in Fig. 5.3b. The fundamental principle exploited here is that analog signal processing is tailored to the spatial structure of the radio channel, while frequency dependence is addressed by digital signal processing at the BBU. In particular, analog spatial filtering design consists in designing a set of delay values $\boldsymbol{\tau}$, and the corresponding analog beamformers $\mathbf{W}_{RF}(f|\boldsymbol{\tau})$ and $\mathbf{F}_{RF}(f|\boldsymbol{\tau})$ are characterized by a frequency independent spatial response. Digital spatial filtering at the BBU, on the other hand, is independently designed and performed on each frequency sub-band by $\mathbf{W}_{BB}(f)$ and $\mathbf{F}_{BB}(f)$.

Uplink is considered to provide a characterization of the signals involved, but extension to downlink is straightforward. Each UE on the scene transmits a signal $s_m(t) = \sum_{k=1}^{N_f} s_{mk}(t)\, e^{j\omega_k t}$ with a multicarrier structure (e.g., OFDM as in 5G NR) composed of N_f subcarriers. The mmWave radio channel between the UE and the n-th antenna of the array is described by P direction of arrivals (DoAs) impinging the ULA at the RAU.

Under the assumption of frequency-independent propagation paths (or DoAs) and delays, the signal received at the n-th antenna is

$$x_n(t) = \sum_{m=1}^{M} \left(\sum_{p=1}^{P} h_{mp} s_m \left(t - \tau_{mpn}^{(r)} \right) \right) , \tag{5.1}$$

where h_{mp} accounts for path loss and possible fading, $\tau_{mpn}^{(r)}$ is the propagation delay for the p-th propagation path from the m-th UE. Broadband processing at the RAU gives the ℓ-th ($\ell = 1, 2, \ldots, L$) FH signal as linear combination

$$y_\ell(t) = \sum_{n=1}^{N} w_{RF,\ell n} x_n (t - \tau_{\ell n}) , \tag{5.2}$$

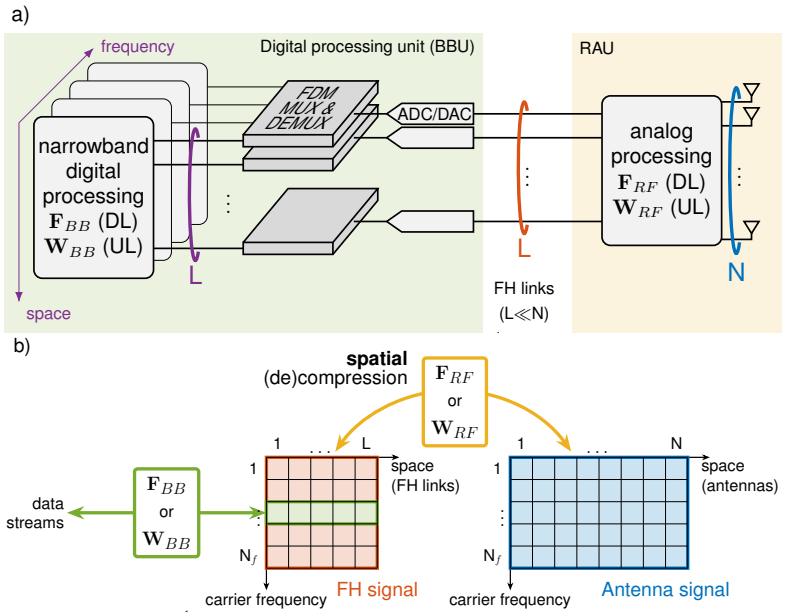

Figure 5.3: System architecture: (a) wideband analog processing at RAU and narrowband digital processing at BBU, (b) representation of signals and processing in space-frequency domain.

where $w_{RF,\ell n}$ is a set of weights designed accounting for the amplitude response that depends on the specific architectural choices, and $\tau_{\ell n}$ is the corresponding delay. Both $w_{RF,\ell n}$ and $\tau_{\ell n}$ are frequency-dependent design parameters, as specified in Section 5.4 for optical processing. After Fourier transform, (5.2) can be written in vector-matrix notation as

$$\mathbf{y}(f) = \mathbf{W}_{RF}(f|\boldsymbol{\tau})\,\mathbf{x}(f)\ , \tag{5.3}$$

where $\mathbf{y}(f) = [y_1(f), \ldots, y_L(f)]^T$ collects the f-th subcarrier of the L FH signals, $\mathbf{x}(f) = [x_1(f), \ldots, x_N(f)]^T$ the N antenna signals and the elements of $\mathbf{W}_{RF}(f|\boldsymbol{\tau}) \in \mathbb{C}^{L\times N}$ are $[W_{RF}(f|\boldsymbol{\tau})]_{\ell,n} = w_{RF,\ell n} e^{-j2\pi f \tau_{\ell n}}$. At the BBU, the FH signal $\mathbf{y}(f)$ is further processed by the digital beamformer $\mathbf{W}_{BB}(f)$ to obtain the M UEs' signals:

$$\hat{\mathbf{s}}(f) = \mathbf{W}_{BB}(f)\,\mathbf{y}(f) = \mathbf{W}_{BB}(f)\,\mathbf{W}_{RF}(f|\boldsymbol{\tau})\,\mathbf{x}(f)\ . \tag{5.4}$$

As customary for narrowband model, the frequency dependence is omitted for sake of notation simplicity so that for model in (5.3), (5.4) is $\mathbf{s} \in \mathbb{C}^{M\times 1}$, $\mathbf{x} \in \mathbb{C}^{N\times 1}$, $\mathbf{y} \in \mathbb{C}^{L\times 1}$ and $\hat{\mathbf{s}} \in \mathbb{C}^{M\times 1}$ and $\mathbf{W}_{RF}$, $\mathbf{F}_{RF}$, $\mathbf{W}_{BB}$ and $\mathbf{F}_{BB}$ are the analog and digital spatial filtering for the uplink and downlink (Fig. 5.4).

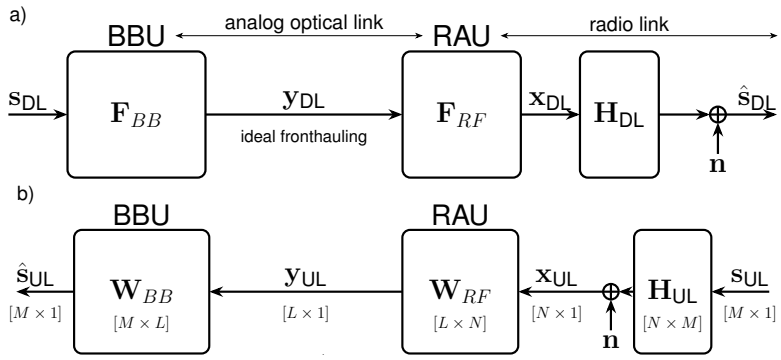

Figure 5.4: System model for the downlink (a) and uplink (b).

Here $\mathbf{s}_{UL} \in \mathbb{C}^{M\times 1}$ collects the M signals generated by the M UEs with power σ_s^2 and assumed to be $\mathbf{s}_{UL} \sim \mathcal{CN}\left(0, \sigma_s^2 \mathbf{I}\right)$, the signal at the RAU is $\mathbf{x}_{UL} = \mathbf{H}_{UL}\mathbf{s}_{UL} + \mathbf{n}$, where $\mathbf{H}_{UL} \in \mathbb{C}^{N\times M}$ is the uplink radio channel and $\mathbf{n} \sim \mathcal{CN}\left(0, \mathbf{R}_n\right)$ is the noise plus interference vector spatially structured according to the DoA pattern of the interferers. The antenna signal $\mathbf{x}_{UL}$ is then processed in the analog domain by $\mathbf{W}_{RF}$, which is the broadband analog beamformer that that yields the fronthaul signal

$$\mathbf{y}_{UL} = \mathbf{W}_{RF}\mathbf{x}_{UL} \tag{5.5}$$

At the BBU the FH signal is then converted to digital and processed by subcarrier-dependent $\mathbf{W}_{BB} \in \mathbb{C}^{M\times L}$ to obtain the estimate $\hat{\mathbf{s}}_{UL} \in \mathbb{C}^{M\times 1}$ of the uplink data streams on the specific subcarrier:

$$\hat{\mathbf{s}}_{UL} = \mathbf{W}_{BB}\mathbf{W}_{RF}\left[\mathbf{H}_{UL}\mathbf{s}_{UL} + \mathbf{n}\right] . \tag{5.6}$$

The directional sparse radio channel $\mathbf{H}_{UL}$ is modeled with $P = 1$ ray per UE, and it depends on the radio frequency f and on users' DoAs $\theta_1, \ldots, \theta_M$

$$\mathbf{H}_{UL} = \left[\begin{array}{ccc} \beta_1 \mathbf{a}\left(f, \theta_1\right) & \ldots & \beta_M \mathbf{a}\left(f, \theta_M\right) \end{array} \right] , \tag{5.7}$$

where β_m accounts for path loss and random fading (recall that all the UEs have the same power σ_s^2) and

$$\mathbf{a}\left(f, \theta_m\right) = \left[\begin{array}{cccc} 1 & e^{j2\pi f d/c_0 \sin(\theta_m)} & \ldots & e^{j2\pi f d/c_0 (N-1)\sin(\theta_m)} \end{array} \right]^T$$

is the ULA array response vector for the DoA θ_m at frequency f, with $c_0 = 3 \cdot 10^8$ m/s.

5.2.2 Performance Metrics

Hybrid beamforming design in Section 5.3 aims at optimizing $\mathbf{W}_{RF}$ and $\mathbf{W}_{BB}$. The performance metric upon which the optimization is based is the signal to interference plus noise ratio (SINR) at the decision variable $\hat{\mathbf{s}}_m$ for the m-th user, that depends on the subcarrier and on the delay set $\boldsymbol{\tau}$ as:

$$\mathrm{SINR}_m\left(f,\boldsymbol{\tau}\right)=\frac{\sigma_s^2\mathbf{w}_m^T\left(f,\boldsymbol{\tau}\right)\mathbf{h}_m\left(f\right)\mathbf{h}_m^H\left(f\right)\mathbf{w}_m^*\left(f,\boldsymbol{\tau}\right)}{\mathbf{w}_m^T\left(f,\boldsymbol{\tau}\right)\mathbf{R}_i\left(f\right)\mathbf{w}_m^*\left(f,\boldsymbol{\tau}\right)}\,, \tag{5.8}$$

where $\mathbf{w}_m^T\left(f,\boldsymbol{\tau}\right)$ is the m-th row of the compound beamformer $\mathbf{W}\left(f,\boldsymbol{\tau}\right)=\mathbf{W}_{BB}\left(f\right)\mathbf{W}_{RF}\left(f|\boldsymbol{\tau}\right)$ (i.e., the beamformer to estimate the signal at frequency f coming from the m-th user), $\mathbf{h}_m\left(f\right)=\beta_m\mathbf{a}\left(f,\theta_m\right)$ is the frequency-dependent radio channel between the m-th single-antenna user and the array, and $\mathbf{R}_i\left(f\right)=\mathbf{R}_n\left(f\right)+\sum_{j=1,j\neq m}^{M}\sigma_{s,j}^2\mathbf{h}_j\left(f\right)\mathbf{h}_j^H\left(f\right)$ is the interference (plus noise $\mathbf{R}_n\left(f\right)$) spatial autocorrelation at frequency f. Performances are also evaluated in terms of average per-user bit rate

$$C_{\mathrm{mean}}\left(f,\boldsymbol{\tau}\right)=\frac{1}{M}\sum_{m=1}^{M}\log_2\left(1+\mathrm{SINR}_m\left(f,\boldsymbol{\tau}\right)\right)\,, \tag{5.9}$$

or, equivalently, in terms of sum rate.

Also, the decorrelation of the estimated data streams $\hat{\mathbf{s}}$ is considered in HBF design, and evaluated as the diagonality of the spatial covariance $\mathbf{R}_{\hat{s}}$. Diagonality is evaluated as the 2-norm of a matrix having the extra-diagonal elements of $\mathbf{R}_{\hat{s}}$ and zeros on the main diagonal.

5.2.3 Design of the Delay Lines

Within HBF design, the choice of $\mathbf{W}_{RF}$ consists in defining a set of delay values, provided by a set of ORR delay lines. As specified in Section 5.4, the delay response of an ORR delay line is a non-linear, and not easily tractable, function of a set of optical phase shifts that are the design parameters. The excessive computational cost makes it unfeasible to compute such design parameters at each re-configuration of the beamformer. To have a realistic system, the selectable delay values are then quantized and delay line design is performed offline. In this way the configurations corresponding to the quantized delay values can be saved in a look-up table at the RAU.

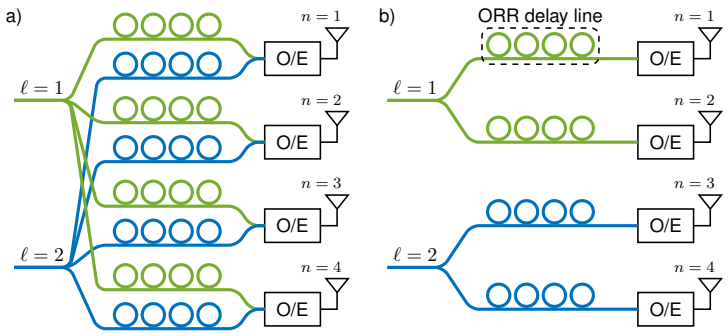

Figure 5.5: Analog OSP layout for (a) fully connected architecture and (b) subarray processing..

5.2.4 Optical Delay Matrix Topology

In the design of $\mathbf{W}_{RF}$, both fully and partially connected array processing architectures at the RAU are taken into account as depicted in Fig. 5.5 for a simple architecture with $N = 4$ antenna elements and $L = 2$ FH links. In case of fully connected array processing at the RAU (Fig. 5.5a), each of the N antennas is connected to L delay lines, so that a $L \times N$ delay matrix is needed. When considering subarray processing in Fig. 5.5b, on the other hand, subarrays are disjoint sets of adjacent N/L antennas of the array, and each of them is connected to only one FH channel, so that each antenna is equipped with one delay line for a total of N delay lines. The analog beamforming matrix $\mathbf{W}_{RF}$ is then block-partitioned in the latter case, thus adding a constraint to the design optimization problem.

Even if tree topologies are typically used for optical delay-and-sum beamforming with ORR delay lines [21], the topologies in Fig. 5.5, although employing a higher number of ORRs, give better flexibility in designing $\mathbf{W}_{RF}$ and allow to independently configure each delay line as detailed later.

Multiplexing of the L fronthaul channels over fiber is not covered here, but it needs to be noticed that an all-analog FH with subarray processing at the analog beamformer may offer simpler solutions. Since in a fully connected analog beamformer all the optical signals generated at the N antennas need to be mixed together, all these optical signals need to be compatible (e.g., same frequency domain, same mode of light, same polarization characteristics) and multiplexing of the L FH signals could be performed (e.g., by employing multicore fibers [61], or time division multiplexing in case of digital CPRI-like FH). On the other hand, when considering subarray processing, the optical signal generated by each laser is related to one FH link only, meaning that some more efficient multiplexing techniques can be em-

ployed, such as frequency division multiplexing (FDM) by downconverting the mmWave radio signal to different intermediate frequencies before modulation of the optical carrier, or spatial techniques such as mode division multiplexing (MDM) [32].

5.3 Hybrid Beamforming Design

Hybrid beamforming leverages on the spatial sparsity of radio signals at the mmWave frequencies and this means that few direction of arrival (DoAs) and directions of departure (DoDs) fully characterize the spatial structure of the radio channel $\mathbf{H}_{UL}$, $\mathbf{H}_{DL}$ (i.e., $P = 1, 2$ in (5.1)). Standard sparse representation algorithms [62] could be used to select L DoAs for analog BF, and disjointly design the analog and digital processing according to [63]. However, such approach is based on a complete (albeit compressed) spatial representation of the radio environment, and it is not practical as it requires the knowledge of either the radio signal $\mathbf{x}$ received at the antenna array (involving digitalization of the antenna signal, which is what is avoided here through HBF) or the DoAs of both users and interferers (e.g., UEs connected to a neighboring non-coordinated cell).

A joint design of the digital and analog processing is proposed here, inspired by the matching pursuit paradigm and based on a limited dictionary of analog beamformers with the knowledge of the spatial correlation $\mathbf{R}_y$ of the L-dimensional fronthaul signals. A dictionary $\mathbf{D} \in \mathbb{C}^{Q \times N}$ collects all the Q possible analog beamforming to be performed at the RAU, among which L spatial filters are chosen to build $\mathbf{W}_{RF}$.

Uplink-downlink duality [64] allows to assume (in absence of power constraints) that beamformers and precoders have the same structure: $\mathbf{W}_{BB} = \mathbf{F}_{BB}^T$ and $\mathbf{W}_{RF} = \mathbf{F}_{RF}^T$.

5.3.1 Dictionary D Building

Since the mmWave radio channel can be effectively modeled as directional, a wise choice for the dictionary $\mathbf{D} = [\mathbf{d}_1, \mathbf{d}_2, \ldots, \mathbf{d}_Q]^T$ is a collection of Q beamsteering vectors towards Q directions. The q-th atom of the dictionary is $\mathbf{d}_q = \exp\left(-j2\pi f_{RF}\boldsymbol{\tau}_q\right)$, where the exponential acts as an element-wise delay that is defined, up to a constant, as

$$\boldsymbol{\tau}_q = d/c_0 \cdot \sin\left(\theta_q\right) \cdot [0, 1, \ldots, N-1]^T \quad , \tag{5.10}$$

and analog BF design is performed at the central frequency f_{RF}. In this way, defining the dictionary for analog beamforming reduces to choosing Q

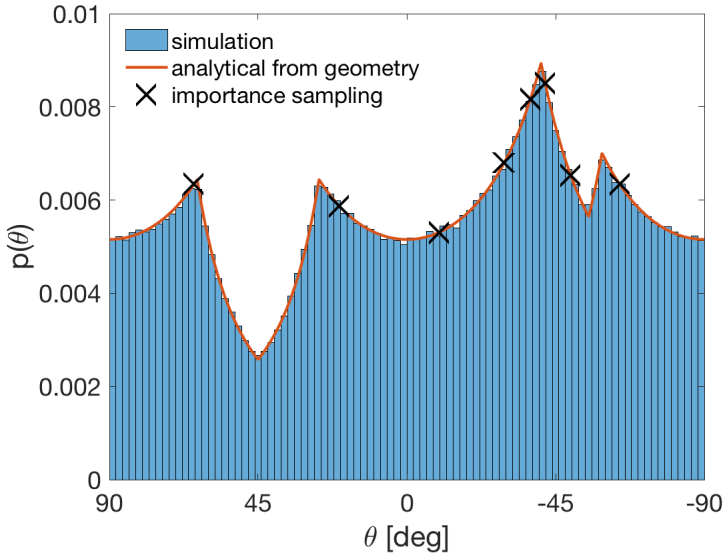

Figure 5.6: Probability density function of UE's DoA (θ), for uniform distribution of UEs in geometry of Fig. 5.1. Markers indicate the selected DoAs for $\mathbf{D}$ with $Q = 8$.

directions to sample the coverage area of the array, and the choice of Q implies a trade-off between the accuracy in sampling of the radio environment and the computational cost of the design algorithm.

The Q directions are chosen via importance sampling from the probability distribution function p_θ of the angular position of a UE with respect to the array that depends on propagation and UE deployments. Assuming here a uniform distribution of UE position within the coverage area of Fig. 5.1, p_θ with $Q = 8$ selected samples is shown in Fig. 5.6.

Remark: The distribution function p_θ can be estimated from historic data by using pattern analysis and machine learning methods, and distribution can be progressively refined based on the dictionary employed. This degree of adaptation is not exploited here.

5.3.2 Digital Beamformer Design

Digital spatial processing at the BBU is designed according to the minimum mean square error (MMSE) paradigm for the overall channel matrix seen at the BBU after analog beamforming (again referring to the uplink for one subcarrier):

$$\mathbf{H}'(f) = \mathbf{W}_{RF}(f|\boldsymbol{\tau})\,\mathbf{H}(f) \tag{5.11}$$

and the spatial autocorrelation of the fronthaul signal is $\mathbf{R}_y(f) = \mathrm{E}\left[\mathbf{y}(f)\,\mathbf{y}^H(f)\right]$. The digital MMSE beamformer is then

$$\mathbf{W}_{BB}(f) = \mathbf{A}^H(f, \boldsymbol{\theta})\,\mathbf{W}_{RF}^H(f|\boldsymbol{\tau})\,\mathbf{R}_y^{-1}(f)\ , \tag{5.12}$$

where $\mathbf{R}_y(f)$ is evaluated at the BBU.

5.3.3 Joint Analog-Digital BF Design

Given a dictionary $\mathbf{D} \in \mathbb{C}^{Q\times N}$ containing all the Q possible analog beamforming to be performed at the RAU, hybrid beamforming design consists in selecting L rows of $\mathbf{D}$ ($\mathbf{W}_{RF} = \mathbf{D}_\Omega$ where Ω is an L-dimensional subset of the Q rows of $\mathbf{D}$) and designing a suitable digital processing $\mathbf{W}_{BB}$ as in Section 5.3.2. An exhaustive search to define the optimal set Ω is unfeasible as the computational cost grows as $\binom{Q}{L}$. An efficient alternative, although suboptimal, is to successively select one dictionary atom $\mathbf{d}_q^T$ at a time as suggested by the matching-pursuit paradigm and specified in the following.

The proposed hybrid beamforming design algorithm gives indeed a suboptimal solution to the problem, but guarantees a substantial reduction of computational cost that grows as $L \cdot Q$. The steps of the design algorithm are summarized in Alg. 2. If $L = M$, $\mathbf{W}_{RF}$ provides beamsteering towards the M DoAs in the dictionary closest to the DoAs of the served users. If $L > M$, the hybrid beamforming is obtained iteratively adding a row to the analog BF matrix and choosing the row (i.e., the atom $\mathbf{d}_q^T$ of the dictionary) that maximizes either the average SINR for the M UEs or the incorrelation of $\hat{\mathbf{s}}$ (Section 5.2.2). Hybrid beamforming design is performed at f_{RF}, so that the broadband processing $\overline{\mathbf{W}}_{RF}(\boldsymbol{\tau})$ and the narrowband processing $\overline{\mathbf{W}}_{BB}(f_{RF})$ referred to the central frequency are obtained. In a second step, digital beamformers $\overline{\mathbf{W}}_{BB}(f)$ are computed independently for all subcarriers $f = 1, 2, \ldots, N_f$.

Algorithm 2 MP-inspired hybrid BF design.

- Input: DoAs of the users of interest $\boldsymbol{\theta}$, dictionary of analog beamformers $\mathbf{D}$
- quantize $\boldsymbol{\theta}$ w.r.t. the Q directions of $\mathbf{D}$ to obtain $\bar{\boldsymbol{\theta}}$
- initialization: $\mathbf{W}_{RF}^{(M)} = \mathbf{A}^H\left(\bar{\boldsymbol{\theta}}\right)$
- **for** $\ell = M+1 : L$
  - **for** $q = 1 : Q$
    - $\mathbf{W}_{RF}^{(\ell,q)} = \begin{bmatrix} \mathbf{W}_{RF}^{(\ell-1)} \\ \mathbf{d}_q^T \end{bmatrix}$
    - evaluate $\mathbf{R}_y^{(\ell,q)}$, spatial autocorrelation of FH signal
    - $\mathbf{W}_{BB}^{(\ell,q)} = \left(\mathbf{W}_{RF}^{(\ell,q)}\mathbf{A}\left(\boldsymbol{\theta}\right)\right)^H \left(\mathbf{R}_y^{(\ell,q)}\right)^{-1}$
    - evaluate $\mathrm{SINR}\left(\ell, q\right)$ at decision variable
    - evaluate incorrelation $r\left(\ell, q\right)$ of $\hat{\boldsymbol{s}}$
  - **end for**
  - select $\mathbf{d}_{\bar{q},\ell}^T$ as the dictionary element that maximizes $\mathrm{SINR}\left(\ell, q\right)$ or $r\left(\ell, q\right)$
  - $\mathbf{W}_{RF}^{(\ell)} = \begin{bmatrix} \mathbf{W}_{RF}^{(\ell-1)} \\ \mathbf{d}_{\bar{q},\ell}^T \end{bmatrix}$,
  - $\mathbf{W}_{BB}^{(\ell)} = \left(\mathbf{W}_{RF}^{(\ell)}\mathbf{A}\left(\boldsymbol{\theta}\right)\right)^H \mathbf{R}_y^{-1}$
- **end for**
- Output: $\overline{\mathbf{W}}_{RF} = \mathbf{W}_{RF}^{(L)}$, $\overline{\mathbf{W}}_{BB} = \mathbf{W}_{BB}^{(L)}$
  $\overline{\mathbf{W}}_{RF}$ defines the optimum delay set $\overline{\boldsymbol{\tau}}$

The optimal analog processing $\overline{\mathbf{W}}_{RF}$ in turns defines the optimal set of delay values $\overline{\boldsymbol{\tau}}$ that are required to the ORRs delay lines, and it is updated according to the dynamics of the radio channel and of the time multiplexing scheme. In this case, the radio channel is assumed to be static within the time frame so that the delay profiles are updated as required by time multiplexing.

Remark: Signaling to configure $\mathbf{W}_{RF}$ consists in transmitting the value of the L angles selected within the Q of the dictionary. The association between the angles and the corresponding delay profiles (quantized as hinted in Section 5.2.3) can be stored in a look-up table at the RAU.

5.4 OSP Tunable Delay Lines

Optical signal processing designs integrated optical filters where time is discretized by the delays of optical devices so that optical signals are conveniently described by their $\mathcal{Z}$-transform. [65]. OSP is conceptually based on coupling between adjacent waveguides (acting as signals' sum) and on different propagation delays. The OSP filtering structures consist in generalized interferometers in which the light is split into a number of different paths, delayed in different ways and recombined to give the output signal. The two elementary devices are optical ring resonators (ORRs) and Mach-Zehnder interferometers (MZI), and the tunability of the optical filter response is guaranteed by optical phase shifters. For instance, a symmetric MZI with tunable phase shift on one of the two arms results in a tunable coupler. Tunability of phase shifters is based on the thermo-optic effect (local heating of the waveguide modulates the refractive index) and this is the method considered here. Alternative tuning methods such as free-carrier injection involves increased losses [66] and electro-optic phase shifters [67–69], as well as stress-optic actuators [70] can be faster, but bulkier. Some basics of OSP are reviewed herein to address the slow tunability of analog beamformers $\mathbf{W}_{RF}$ or $\mathbf{F}_{RF}$ to varying users' allocation within different RBs.

5.4.1 ORR Delay Line

The optical carrier is modulated by the RF signal, this propagates through a waveguide and is then converted back to the electrical domain by a photodetector. The effective time delay experienced by the RF signal is the group delay of the optical waveguide. Such group delay can be controlled by placing an ORR parallel to the waveguide as in Fig. 5.7. The transfer function of the optical architecture in Fig. 5.7 is known and largely experimented [65,71–73]:

$$G(z) = \frac{Y(z)}{X(z)} = \frac{c - \gamma e^{-j\phi} z^{-1}}{1 - c\gamma e^{-j\phi} z^{-1}} \tag{5.13}$$

where γ accounts for the round-trip losses (i.e., the optical signal attenuation after completing one round through the ring), ϕ is the phase shift imposed on the ring to control the resonance frequency and $c = \sqrt{1-\kappa} = \sin(\psi/2)$.

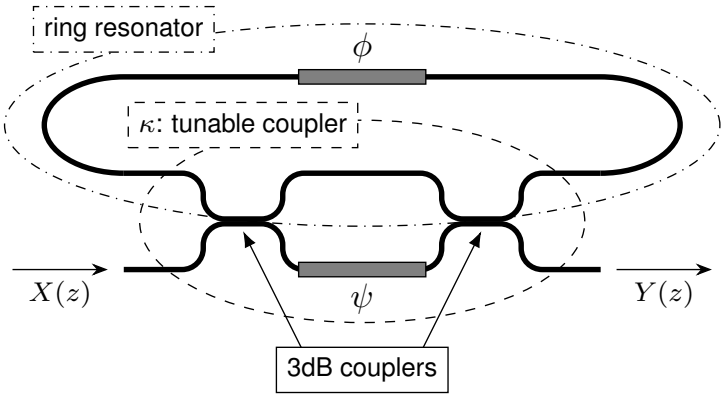

Figure 5.7: Layout of a tunable ORR.

The phase term ψ controls the power coupling ratio κ between the straight waveguide and the ring. The unit delay expressed by z^{-1} depends on the optical length of the ring and it is $T = L_r \cdot n/c_0$, where L_r is the physical length of the ring, $c_0 = 3 \cdot 10^8\,\mathrm{m/s}$ and n is the refractive index of the waveguide. The unit delay T defines the free spectral range $\mathrm{FSR} = 1/T$ which is the periodicity in the frequency domain due to the discrete-time nature of the system according to the ring-length.

The transfer function (5.13) gives a group delay response which is

$$\begin{aligned}\tau(\omega) =& -\frac{\partial \angle G(\omega)}{\partial \omega} T \\ =& \frac{\gamma(\gamma - c\cos(\omega+\phi))}{c^2 - 2c\gamma\cos(\omega+\phi) + \gamma^2} T \\ & - \frac{c\gamma(c\gamma - \cos(\omega+\phi))}{c^2\gamma^2 - 2c\gamma\cos(\omega+\phi) + 1} T\,,\end{aligned} \tag{5.14}$$

and the theoretical behavior (5.14) is well supported by experimental evidence [57,74]. The resulting bell-shaped delay response is centered at $\omega = -\phi$, and higher values of coupling κ give a smoother curve with a lower peak value at the resonance frequency, while lower values give a sharper curve with higher peaks. The amplitude response, on the other hand, shows unit gain at frequencies far away from the resonance and a slight attenuation in correspondence with the delay peak. Such attenuation depends on the loss coefficient γ and is related to the delay response itself (higher in-band delays correspond to higher in-band attenuation):

$$|G(\omega)|^2 = \frac{c^2 + \gamma^2 - 2c\gamma\cos(\omega+\phi)}{1 + c^2\gamma^2 - 2c^2\gamma^2\cos(\omega+\phi)}\,. \tag{5.15}$$

By cascading K ORR delay elements as the one in Fig. 5.7 (so that the output of the k-th element is the input of the $(k+1)$-th, $X_{k+1}(z) = Y_k(z)$ as in Fig. 5.8a, inset), the resulting response is $G_K(z) = \prod_{k=1}^{K} G_k(z)$, which means that the delay responses sum up to give the overall delay response $\tau_K(\omega) = \sum_{k=1}^{K} \tau_k(\omega)$.

The delay response is optically narrowband, but still wideband for the RF signal and it can be tailored to the RF signal at hand via tuning the phase shifts $\{\phi_k\}_{k=1}^{K}$ and $\{\psi_k\}_{k=1}^{K}$. In particular, it is possible to obtain a higher delay at the desired resonance frequency and/or a larger bandwidth in which the delay response is approximately flat and the overall design results in a trade-off between in-band delay, bandwidth, delay ripple and number of rings (i.e., optical architecture complexity). Once the number of employed rings is fixed, high delay values can be ensured with low ripple over narrower bandwidths with respect to low in-band delays. Since the expression for $\tau_K(\omega)$ is analytically intractable, a straightforward design approach to comply with analog beamformers $\overline{\mathbf{W}}_{RF}$ (or $\overline{\mathbf{F}}_{RF}$) specifications does not exist. In this work the error between the desired delay values $\overline{\boldsymbol{\tau}}$ and the analytic delay response obtained within a specified bandwidth is minimized to design the optical parameters. Such minimization takes into account symmetry considerations regarding the delay response in (5.14): the phase terms $\{\phi_k\}_{k=1}^{K}$ are placed symmetrically around the central resonance frequency (e.g., $\omega_0 = 0$) and also the coupling ratios determined by $\{\psi_k\}_{k=1}^{K}$ are symmetrical ($\kappa_1 = \kappa_K$, $\kappa_2 = \kappa_{K-1}$ and so on).

5.4.2 Delay Line Tunability

Delay line tunability refers to the control of phase terms $\{\phi_k\}_{k=1}^{K}$ and $\{\psi_k\}_{k=1}^{K}$ to attain RB dependent time-varying delays. Even if the control of the delay lines can be carried out by other technologies, the usage of thermo-optic tunable shifters is opportunistically preferred within the scientific community [75] and this motivates this choice in the analysis that follows. Nevertheless, the conceptual steps herein followed can be extended to other technologies, if necessary.

Delay line tunability is through thermo-optic tunable phase shifters that rely on the thermo-optic effect to produce a local modulation of the refractive index of the waveguide, and hence a phase shift in the optical signal. The first-order transient in temperature have time constants in the order of the microseconds [75,76]. The linear relationship between phase shift $\Delta\varphi$ and temperature change ΔT [66]: $\Delta\varphi = \frac{2\pi L_h}{\lambda_0}\frac{dn}{dT}\Delta T$, makes the phase deviation follow the same transient (here L_h is the heater length, λ_0 is the free-space

Material	**Losses [dB/cm]**	$\boldsymbol{n}$	$\boldsymbol{dn/dT}$ **@300**$\boldsymbol{K}$
Doped silica	$0.03 \div 0.07$	$\simeq 1.5$	$\simeq 10^{-5}$
$LiNbO_3$	$\simeq 0.1$	$\simeq 2.2$	$\simeq 10^{-5}$
InGaAsP	< 0.2	$3.1 \div 3.7$	$\simeq 2 \times 10^{-4}$
Polymers	$0.06 \div 0.43$	$1.3 \div 1.6$	$(-1 \div -4) \times 10^{-4}$
Silicon	< 1	$\simeq 3.5$	1.86×10^{-4}

Table 5.1: Indicative values for common waveguide materials [65].

optical wavelength, and dn/dT is the thermo-optic coefficient). An exponential transient with $1.5\,\mu$s time constant is assumed here both for cooling and heating.

5.4.3 Waveguide Materials

Several different materials are used to build optical waveguides, and their characteristics of interest are summarized in Table 5.1. Physical characteristics of the waveguide influence the overall response as described in the following. The ring length L_r and the waveguide refractive index n define the unit delay $T = L_r \cdot n/c_0$ and the corresponding FSR $= 1/T$. In this context, λ-independent refractive index is considered, and losses are accounted for by parameter γ (typical losses are $< 0.1\,$dB/cm for conventional doped silica waveguides). The thermo-optic coefficient dn/dT indicates the tunability as described in Section 5.4.2: high values of dn/dT allows to build faster and/or smaller phase shifters.

With reference to the quantities considered in Table 5.1, low losses are required to limit in-band attenuation, high refractive index is needed to build smaller rings and high thermo-optic coefficient allows for fast and compact thermo-optic phase shifters. From these considerations Indium Gallium Arsenide Phosphide (InGaAsP) is considered here for analog beamforming as it is a favorable mixture of limited losses, high refractive index and high thermo-optic coefficient. Furthermore, being it already used for lasers and photodetectors, it allows for an integrated and compact circuit for joint electro-optical conversion and optical signal processing.

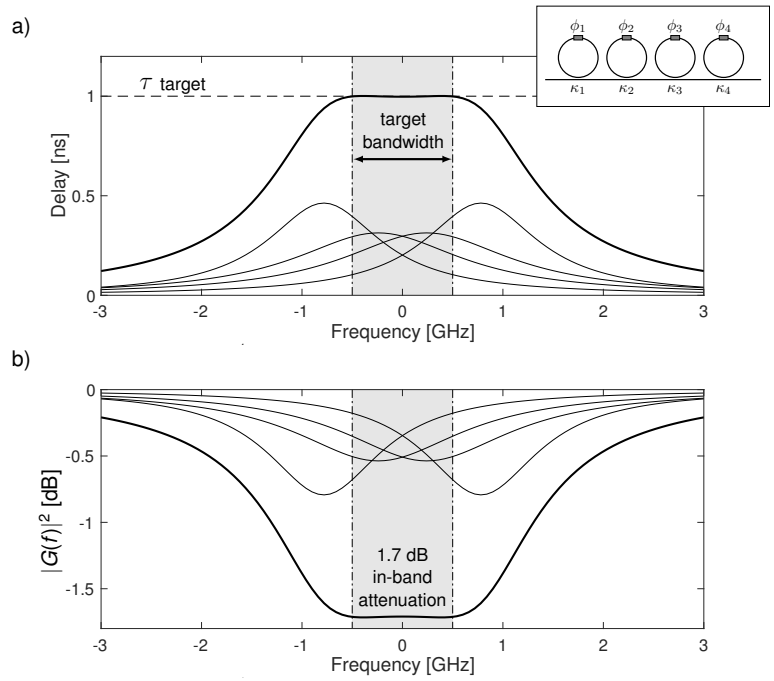

Figure 5.8: 4-ORRs delay line: (a) delay response (inset: 4-ORRs delay line architecture) and (b) amplitude response for the single ORRs (thin lines) and for the overall system (thick lines).

5.4.4 4-ORR Tunable Delay Line

Let us now consider the design of the ORR delay lines, which consists in choosing the number of ring resonators per delay line, the FSR and the waveguide material. For $f_{RF} = 30$ GHz, FSR = 60 GHz is chosen here for compactness, and the selected material is InGaAsP as explained in Section 5.4.3 (in particular, 0.1 dB/cm losses and $n = 3.5$ are considered). In these settings, the unit delay is $T \simeq 16.66$ ps, the length of the ring is $L_r \simeq 1.4$ mm and the corresponding round-trip loss coefficient is $\gamma \simeq 0.9967$.

A set of delay lines composed of $K = 4$ cascaded ORRs as in Fig. **??**a (inset) is considered here and the maximum delay required along the array in analog BF depends on the size of the array and on the coverage area. In the settings of Section 5.2, and considering $N = 64$ antennas at the array,

$$\tau_{max} = (N-1)\sin(\theta_{max})\,\lambda_{min}/2c \simeq 1\text{ ns} \quad . \tag{5.16}$$

The design of the delay lines is then a set of quantized delay values within the interval $\tau \in (0,\ 1)$ ns with $2^{N_{bit}}$ levels and $N_{bit} = 6$. Fig. **??** shows the delay and amplitude responses (in Fig. **??**a and **??**b respectively) for a 1-ns delay over a 1-GHz bandwidth as design specifications. The achieved in-band delay

ripple, defined as $\delta\tau_{\max} = \max_{\omega\in\Omega_B} |\tau(\omega) - \tau_B|$ (where Ω_B is the frequency band of interest and τ_B the target in-band delay), is $\delta\tau_{\max} \simeq 3\,\text{ps}$.

Once again, FSR should be a submultiple of 60 GHz for the delay line response to match the spectrum of the modulated optical signal. A choice of lower value of FSR would imply larger rings, but also a higher unit delay, meaning that it is possible to employ less rings (i.e., lower complexity) for similar performance.

5.5 Numerical Analysis

The proposed architecture and HBF design are evaluated numerically, with the reference settings of Section 5.2 and summarized here. In particular, $S = 504$ UEs are served, uniformly distributed within the $17000\,\text{m}^2$-area of Fig. 5.1. All the UEs occupy the whole 1-GHz system bandwidth, and multiplexing is in the space-time dimensions. The radio channel is characterized by $P = 1$ propagation path (i.e., one DoA) per UE, and the DoA is frequency-independent.

Benchmark for HBF performance is MMSE fully digital beamforming ($\mathbf{F}_{RF} = \mathbf{W}_{RF} = \mathbf{I}$ and $L = N$) as detailed in Section 5.5.1. Section 5.5.2 is the static performance of the system without any transient in optical delay lines tuning, that is analyzed later in Section 5.5.3.

5.5.1 Benchmark Digital MMSE Beamforming

Ideally, with reference to uplink and to one sub-carrier, digital beamforming should act directly on the signals received by the antennas, to yield

$$\hat{\mathbf{s}}(f) = \mathbf{W}_{ideal}(f)\,\mathbf{x}(f) \tag{5.17}$$

where $\mathbf{W}_{ideal}(f) = [\mathbf{w}_1(f), \ldots, \mathbf{w}_M(f)]^T$ is the beamforming matrix and $\mathbf{w}_m^T(f)$ is the spatial filter for the m-th user at sub-carrier frequency f. Linear MMSE beamforming is considered here to separate the M uplink signals [56]. Assuming known channels for all the users according to (5.7), the MMSE beamformer can be written (up to a scale factor) as

$$\mathbf{W}_{ideal}(f) = \mathbf{A}^H(f, \boldsymbol{\theta})\mathbf{R}_x^{-1}(f)\ , \tag{5.18}$$

where $\mathbf{R}_x(f) = \text{E}\left[\mathbf{x}(f)\,\mathbf{x}^H(f)\right]$ is the covariance matrix for the overall signal $\mathbf{x}$. Such ideal all-digital spatial processing is considered as the optimum benchmark.

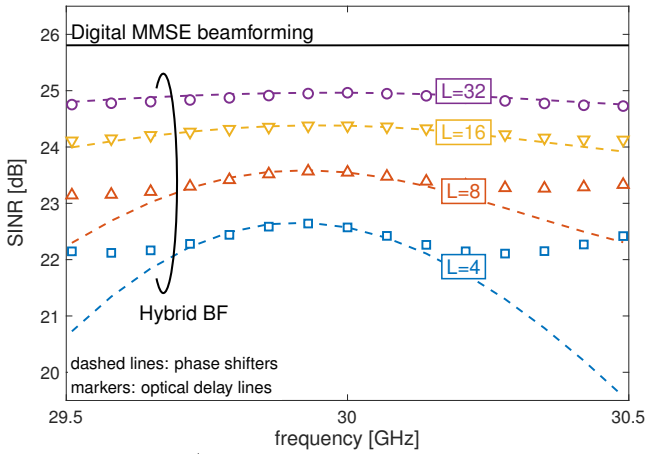

Figure 5.9: Average SINR vs frequency by analog BF with phase shifters (dashed lines) or delay lines (markers) designed at $f_{RF} = 30\,\text{GHz}$ for $L = 4$ (blue), 8 (red), 16 (yellow) or 32 (purple). $N = 64$ antennas at the RAU array, $M = 4$ UEs served in each time slot from a pool of $S = 504$ UEs on the scene, noise power corresponding to SNR $= 10\,\text{dB}$ referred to the average received power and fully connected architecture, $Q = 64$..

5.5.2 Static Performance of Hybrid BF

The reason for using delay lines in analog beamforming is the possibility to deal with broadband signals without the undesirable beam squint when using narrowband phase-shift-based analog BF. System performance when employing either delay lines of phase shifters instead of delays is in Fig. 5.9: HBF design as in Section 5.3.3 selects the L DoAs for analog beamforming. The corresponding phase shifts computed for $f_{RF} = 30$ GHz are applied to all the subcarriers (analog processing with phase shifters, dashed lines) or the corresponding delay values are considered (analog processing with delay lines, markers). Beam squint, albeit partially compensated by digital narrowband processing for each sub-carrier, affects the system performance (here evaluated in terms of average SINR at the decision variable) at the band edge. Increasing the number of FH links L (i.e., worsening the system in terms of complexity, spectral efficiency and energy consumption/dissipation control) the SINR attains the digital MMSE beamforming bound with lower edge-band distortion (dashed lines). True time delay circuits have a very small beam-squint with flat SINR within the signal bandwidth, where the flatness is strictly related to those of the delay response $\tau(\omega)$ of the delay lines, computed as in Section 5.4 for the quantized delay values.

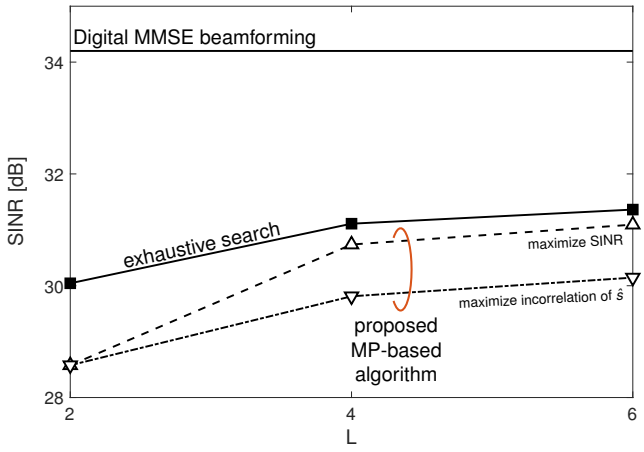

Figure 5.10: Average SINR varying L, compared to benchmark all-digital MMSE beamforming, considering exhaustive search to select the best dictionary elements (solid line, squared filled markers) and the proposed algorithm (empty markers) either maximizing the SINR at the decision variable (dashed line, upward triangles) or maximizing diagonality of $\mathbf{R}_{\hat{s}}$ (dash-dotted line, downward triangles). $N = 64$ antennas at the RAU array, $M = 2$ UEs served in each time slot, $Q = 32$ and SNR $= 20$ dB referred to the average received power, fully connected architecture.

The effectiveness of the HBF search algorithm (Section 5.3.3) is in Fig. 5.10 by comparing the average SINR within signal bandwidth with the exhaustive-search algorithm that chooses the best beamforming $\mathbf{W}_{RF}$ (and the consequent $\mathbf{W}_{BB}$) among all the possible choices of L elements of the dictionary. The scenario is simple to avoid unbearable computations for exhaustive search: $M = 2$ UEs are served in each RB, $N = 64$ antennas at the RAU, dictionary size $Q = 32$, SNR $= 20$ dB and a fully connected architecture performs analog processing at the RAU. The proposed HBF design algorithm is then shown to provide performance similar to that of the optimal exhaustive search when maximizing SINR, at a fraction of the cost. In the remaider of the Chapter, the max-SINR approach is considered for HBF design.

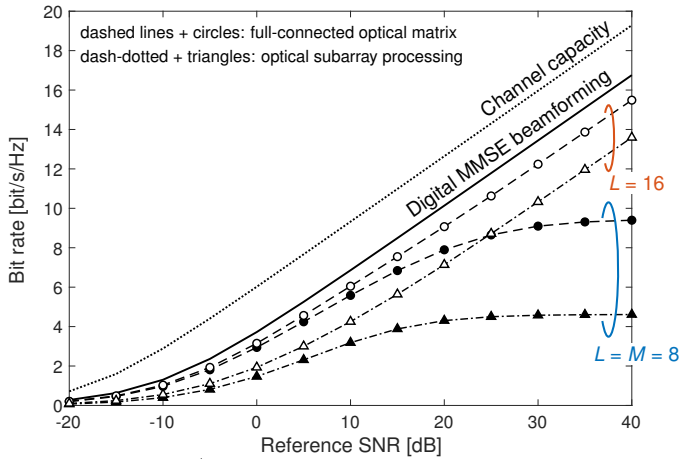

Figure 5.11: Average capacity of the UE-BBU links versus air-link SNR (referred to the average received power) for $L = 8$ (full markers) and $L = 16$ (empty markers) in case of full-connected optical architecture (dashed lines, circles) and optical subarray processing (dash-dotted lines, triangles). $N = 64$ antennas at the RAU array, $M = 8$ UEs served in each time slot from a pool of $S = 504$ UEs on the scene, $Q = 64$.

Fig. 5.11 shows the system performance evaluated in terms of achievable spectral efficiency within the system bandwidth. The average spectral efficiency of the UEs-BBU connections is for varying SNR on the air link (referred to the average received power at the array) when serving $M = 8$ UEs within the same RB. Analysis in Fig. 5.11 compares different numbers of RF chains / FH links ($L = M = 8$ and $L = 16$) and different architectural choices: a fully connected analog BF (i.e., employing a total of $N \times L$ delay lines at the RAU) or subarray processing (i.e., N delay lines). The size of the analog beamforming dictionary is here $Q = 64$.

The achievable spectral efficiency is also analyzed when varying the size Q of the dictionary for analog beamforming in Fig. 5.12a, with SNR $= 20\,\text{dB}$, $M = 8$ UEs/RB and $L \in \{8, 16, 32\}$. The corresponding computational complexity in designing the hybrid beamformer is in Fig. 5.12b for $L = 16$ and $L = 32$, where computational cost counts the number of times an analog and digital beamformer are built and SINR is evaluated according to Alg. 2.

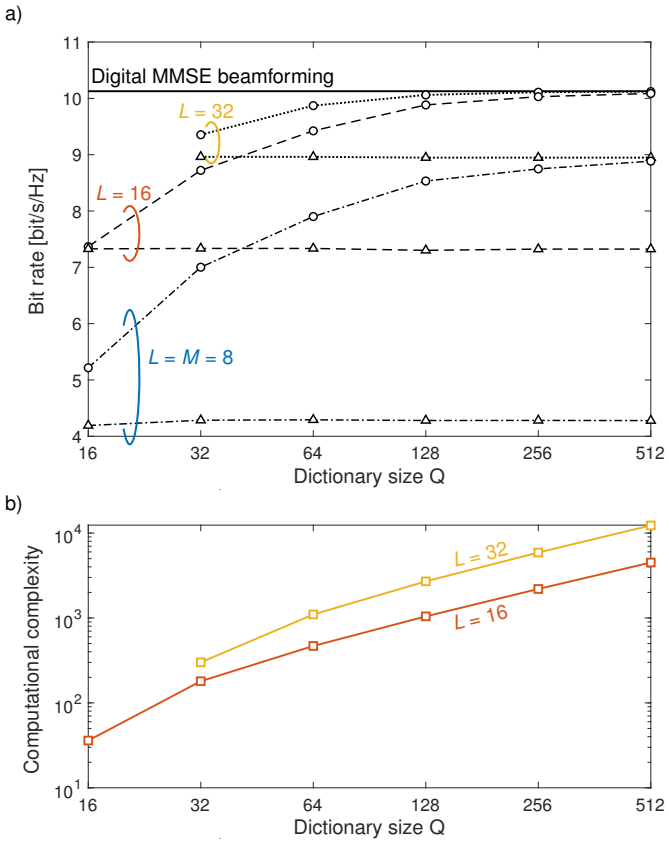

Figure 5.12: Average capacity of the UE-BBU links versus dictionary size Q (a) and the corresponding computational complexity (b). Average capacity is for a fully connected architecture (circle markers) and for subarray processing (triangles), with $L = 8$ (dash-dotted lines), $L = 16$ (dashed lines) or $L = 32$ (dotted lines), compared to benchmark digital MMSE beamforming (solid line). Computational complexity (b) is assessed for $L = 16$ and $L = 32$. $N = 64$ antennas at the RAU array, $M = 8$ UEs served in each time slot from a pool of $S = 504$ UEs on the scene, noise power at the RAU antennas corresponding to SNR $= 20\,\mathrm{dB}$ referred to the average received power.

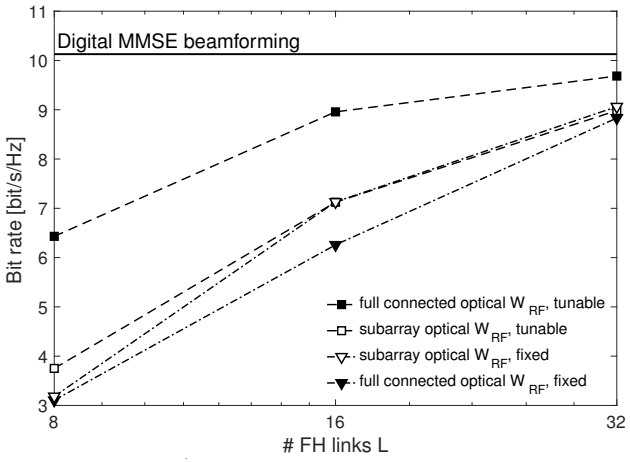

Figure 5.13: Average capacity of the UE-BBU links versus number of FH links L for adaptive (dashed lines, squares) or fixed (dash-dotted lines, triangles) analog beamforming with both fully connected optical architecture (full markers) or optical subarray processing (empty markers). SNR = 20 dB, $M = 8$ UEs/RB, $Q = 64$ for adaptive analog BF.

The effectiveness of tunable analog beamforming with respect to a fixed-beams approach is assessed in Fig. 5.13, where the average bit rate of the UE-BBU links is evaluated for varying number of fronthaul links L for a fully connected optical architecture and for optical subarray processing. For the fixed-beams approach, the L selected DoAs for analog beamforming are those that are best suited to the users' distribution, i.e., those selected for building a dictionary of size L as in Section 5.3.1. In accordance with Fig. 5.12a, subarray processing yields no substantial advantages in using an tunable analog processing. Indeed, the L selected directions for fixed analog beamforming are those selected to build a dictionary of size L, and subarray processing show no dependency on dictionary size. On the other hand, especially at low values of L, the adaptive setup provides remarkable gains in a fully connected architecture. Following this reasoning, transient performance is evaluated only for fully connected analog beamformers in Section 5.5.3.

5.5.3 Transient of Hybrid BF

The first-order gradient in optical phase shifts described in Section 5.4.2 is considered in the time evolution of the delay profile $\tau(\omega)$ in (5.14) when a step in heating power is given as input to tune the delay line. The delay evolution at the central frequency is illustrated in Fig. 5.14 for $\tau_0 = 0.08\,\text{ns}$ and $\tau_1 \in (0.08\,\text{ns}, 0.9\,\text{ns})$.

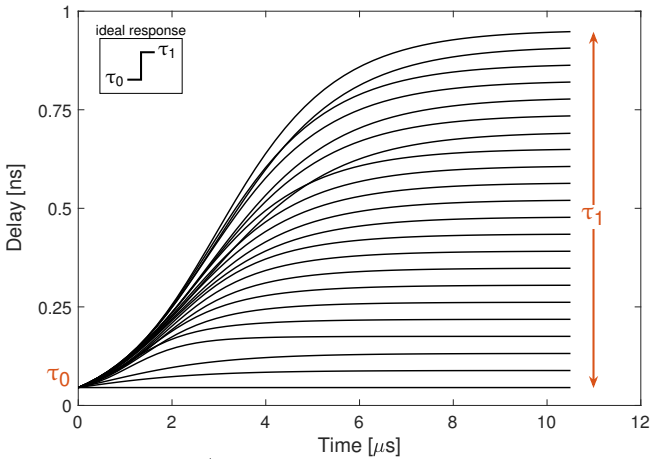

Figure 5.14: Time evolution of the delay response of 4-ORR delay lines at f_0 caused by a step in heating power at the thermo-optic phase shifters.

The impact of such transient in the tuning of optical delay lines is considered, and the digital compensation of it is also evaluated. The evolution model of the delay profile is known, which means that the actual temporal evolution of the mismatch of the analog beamformer $\mathbf{W}_{RF}(t)$ can be determined off-line (e.g., possibly by calibration procedures) and a suitable time-varying digital filter $\mathbf{W}_{BB}(t)$ can be used, designed as in (5.12), to compensate the resulting mismatched $\overline{\mathbf{W}}_{RF}$ thanks to the much faster tunability of digital filters. This digital compensation of the analog BF transient is assumed here to be perfect, i.e., to perfectly match the evolution of the delay profile.

The average SINR transient within the first symbol of each NR OFDM time slot is considered here for a sample configuration of the 5G NR (17.84 μs symbol duration): in Fig. 5.15 such transient is evaluated for $M = 8$ UEs/RB and $L = 8$ (Fig. 5.15a) or $L = 16$ (Fig. 5.15b) with or without digital compensation of the transient in the response of the analog beamformer and with the scheduling algorithm proposed in Section 5.2 as opposed to a first-come-first-served (FCFS) policy in which the M UEs in each resource block are drawn from a uniform distribution over the coverage area. Fig. 5.15 proves that, for $L = M$, the proposed UEs scheduling, albeit primitive, is enough to compensate for the transient capacity loss as explained in the following. On the other hand, if $L > M$, digital compensation is mandatory to avoid intolerable loss of the capability to transparently use the first OFDM symbol for synchronization or channel estimation of the air-link as typical.

Considering the proposed sectorial scheduling, it is to be noticed in Fig.

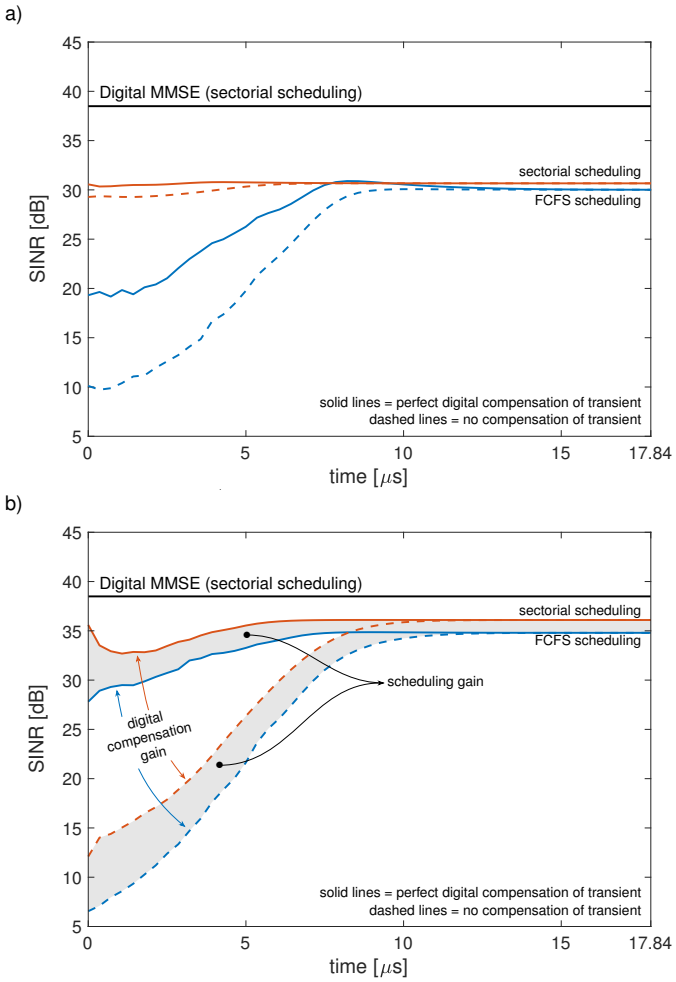

Figure 5.15: SINR at the decision variable within the first symbol interval: $M = 8$ UEs/RB and $L = 8$ (a) or $L = 16$ (b). $N = 64$, SNR $= 20$ dB, $\tau = 1.5\,\mu$s and fully connected optical architecture.

5.15 that, without the digital compensation, system performance is affected by the transient in a much more profound way when $L = 16$ (red, dashed lines in Fig. 5.15). This is due to the scheduling and to the design algorithm for the hybrid beamformer: if $L = M$, the selected DoAs for analog beamforming are those of the M UEs. Pairwise, the UEs served in adjacent time slots present similar angular position and the update of the analog BF requires minor adjustments, system performance is almost not affected. On the other hand, when $L > M$, further $M - L$ DoAs are selected by the HBF design algorithm. Such DoAs are selected to provide a richer description of the radio environment, thus depending also on the position of uncoordinated

interfering UEs served by adjacent hotspots. The position of the uncoordinated interferers active in different time slots is an uncorrelated process, meaning that the selected DoAs for analog BF is an uncorrelated process as well. Greater adjustments in the delay profiles are then required and the impact of finite tuning time of the optical processing causes significant performance degradation.

5.6 Concluding Remarks

A radio access architecture merging the advantages of analog fronthauling and hybrid beamforming is proposed, based on true time delay elements built with photonic devices. The use of delay lines is paramount for broadband processing, and an optical hardware solution based on the use of optical ring resonators is considered. An algorithm for HBF design based on the matching-pursuit paradigm is introduced and applied to a realistic scenario. The effectiveness of the proposed algorithm is proven by comparison with an exhaustive search approach, showing similar performance but at a fraction of the computational cost. Both a partially and a fully connected optical architectures are taken into account for the analog beamformer at the RAU, resulting either in a lower cost or in a much better spectral efficiency respectively.

When considering optical subarray processing, static analog BF guarantees the same performance of adaptive analog BF, much lower hardware complexity is involved and more efficient multiplexing of the FH signals is enabled. On the other hand, a fully connected optical architecture requires adaptive analog beamforming to exhibit its potential for much better performance, thus requiring an increase in complexity and the need to address hardware tunability. Thermo-optic tunable delay lines are considered for cost effectiveness and reduced dimensions, and the resulting performance transient is evaluated. A technology-aware scheduling and digital beamforming are proposed and demonstrated to be a valid strategy for reducing the performance degradation related to tunability transient at the early part of the frame, and this is of utmost importance in fast varying radio resource allocations among many users.

Chapter 6

Joint Intensity-Polarization Modulation

Contributions

In this Chapter, binary polarization shift keying (2-PolSK) is proposed to provide a cost-effective signaling channel between RAUs and BBUs, transparent with respect to the FH link and involving a minimal increase in complexity. Experimental validation is performed with A-RoF transport of a LTE-like OFDM signal through the IM/DD fronthauling, and a binary stream at 1.5 Mbit/s on the 2-PolSK channel.

Organization

The proposed joint intensity-polarization modulation of optical signals is introduced in Section 6.1, and an ideal description of the optical architecture and of the signals involved is in Sections 6.2 and 6.3. The experimental setup is described in Section 6.4, and results are in Section 6.5. Concluding remarks are drawn in Section 6.6.

6.1 Introduction

As seen in Chapter 5, adaptive processing at the RAU is mandatory to take full advantage of wideband hybrid beamforming. There is then the necessity of a control channel between the BBU and the RAU, possibly involving a minimal increase in complexity and without the introduction of additional impairments on the FH transmission, to exchange signaling messages (e.g., the focus DoAs $\boldsymbol{\theta}$ for the analog beamformer). With reference to the architecture of Chapter 5, as specified in Section 5.3, the signaling channel should

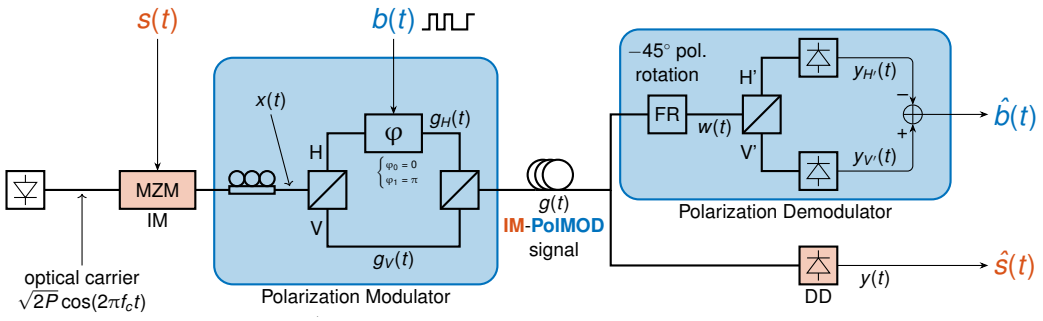

Figure 6.1: Joint intensity-polarization mo-demodulation scheme. The components for the IM/DD channel are in red, those for the parallel 2-PolSK channel are in blue.

transport $r_b = L \cdot \log_2 Q / T_{slot}$ bit/s, where L is the number of FH links, Q the dictionary size for analog BF and T_{slot} the duration of the TDM slot. Assuming $L = 16$, a 8-bit DoA quantization for the analog BF ($Q = 256$) and a 125-μs time slot according to 5G NR, $r_b = 16 \cdot \log_2 256/125\mu s \simeq 1$Mbit/s.

Aim of this Chapter is to propose and experimentally validate the use of binary polarization shift keying (2-PolSK) to provide a signaling channel on top of intensity modulation/direct detection (IM/DD) fronthauling as in Fig. 6.1. A-RoF IM/DD is considered here, with the transmission of a LTE-like OFDM signal, but the same principle can be straightforwardly applied to digital FH as well.

6.2 Joint Intensity-Polarization Modulation

The polarization dimension of light has been exploited over the years to achieve either PolSK [23] or polarization division multiplexing (PDM) [77]. PolSK is based on the control of the state of polarization (SOP) of the transmitted lightwave, and it was proposed and investigated from the late-80s to the mid-90s, but lately dismissed due to the emergence of more efficient optical modulation formats such as intensity modulation. PDM, on the other hand, relies on the modulation of two orthogonally-polarized lightwaves to provide a 2x multiplexing gain, at the expense of some increase in complexity to cancel the interference arising from non-ideal behaviors.

2-PolSK is proposed here to provide a control channel, parallel to the A-RoF fronthauling and minimally interfering with it. In this way the digital signaling channel between BBU and RAU is completely disjointed from the FH itself and can be separately managed. The proposed architecture is in Fig. 6.1, and let us define a reference system for the linear SOPs such that

all the three employed polarization beam splitters (PBS) are aligned to the horizontal and vertical axes of the arbitrary reference system.

Any SOP is uniquely defined by a set of coordinates, called Stokes parameters S_1, S_2 and S_3, in a 3-dimensional space. Once normalized by the total power of the lightwave, the three Stokes parameters describe the so-called Poincaré sphere. In PolSK, the constellation points are defined on such sphere. In the binary PolSK employed here, however, only linear polarization states are assumed (at least ideally) so to reduce the complexity of the 2-PolSK modulator and demodulator. Any linear SOP is defined by the S_1 and S_2 parameters alone ($S_3 = 0$), and ideally the binary modulation adopted in this Chapter rely on the transmission of a linearly polarized lightwave with $S_2 = \pm 1$ and $S_1 = 0$ so that in principle estimation of the S_2 parameter at the receiver is enough to estimate the digital stream.

The FH signal $s(t)$ to/from the mobile users modulates the intensity of the linearly polarized laser source, e.g., through a Mach-Zehnder Modulator (MZM). The IM optical signal $x(t)$, linearly polarized at 45° with respect to the SOP reference system, is decomposed in its horizontal and vertical components by a first PBS. One of the two components is phase-modulated with a binary phase shift $\varphi \in \{0, \pi\}$ corresponding to the binary signaling $b(t)$. As a result, after recombination of the two components, the optical signal $g(t)$ is either linearly polarized as $x(t)$ (if $\varphi = 0$) or its SOP is rotated by 90° (if $\varphi = \pi$). After propagation, direct detection (DD) is almost polarization-agnostic and gives an electrical signal $y(t)$ proportional to the received energy (i.e., as if there were no PolSK) that is then used to retrieve the estimate $\hat{s}(t)$ of the FH signal $s(t)$. The 2-PolSK receiver is, in principle, based on the estimation of one single Stoke parameter, specifically S_2, of the received signal via DD as in [24]. The S_2 parameter is defined as the difference in received energy along the 45° and 135° linear polarization states: a Faraday rotator is then employed at the receiver to align the SOP of the propagated signal $g(t)$ with the axes of the receiver PBS, and the difference between the two electric signals obtained through direct detection on the H' and V' paths gives the S_2 parameter which in turn provides the estimate $\hat{b}(t)$ of the digital stream $b(t)$.

6.3 Signals Description

It is assumed here that the IM signal $x(t)$ is obtained via external modulation of a continuous-waveform laser source as in Fig. 6.1. In general, direct modulation of the laser source is possible, and it requires only minor adjustments of the following dissertation, where an ideal signal description

is provided, in order to highlight the principles of the proposed system.

6.3.1 IM Signal $x(t)$

The IM signal $x(t)$ is

$$x(t) = \cos\left[\frac{\pi}{2}\frac{s(t) + V_{bias}}{V_\pi}\right]\sqrt{2P}\cos(2\pi f_c t) \ , \tag{6.1}$$

where $s(t)$ is the driving electrical signal (e.g., the RF signal in A-RoF), V_{bias} and V_π characterize the MZM (bias and switching voltages respectively), and P is the power of the laser signal at frequency f_c fed at the input of the MZM. The optical signal $x(t)$ is linearly polarized at 45° with respect to an arbitrary reference system (linear polarization can be achieved, e.g., using a laser diode as optical source).

6.3.2 IM–2-PolSK Signal $g(t)$

The original RoF signal $x(t)$ is fed to the polarization modulator, which consists in a polarization beam splitter (PBS), a differential phase shifter and a combiner. The PBS separates the vertical and horizontal polarized components (with respect to the previously defined arbitrary reference system) of the 45°-linearly polarized input signal, so that the two components are:

$$x_H(t) = x_V(t) = \frac{\sqrt{2}}{2}x(t) \ . \tag{6.2}$$

After phase shift, the H and V components of the polarization-modulated RoF signal are:

$$g_V(t) = x_V(t) = \frac{\sqrt{2}}{2}x(t) \tag{6.3}$$

and

$$g_H(t) = e^{j\varphi}x_H(t) = \pm\frac{\sqrt{2}}{2}x(t) \tag{6.4}$$

in the two cases of $\varphi = 0$ and $\varphi = \pi$. In this way, the obtained signal $g(t)$ is linearly polarized either at 45° ($\varphi = 0$) or at 135° ($\varphi = \pi$).

6.3.3 Received RoF Signal

After propagation, the optical signal is received by a photodiode that provides polarization-agnostic direct detection: the resulting electrical signal $y(t)$ is proportional to the received optical power,

$$y(t) \propto |g(t)|^2 \ . \tag{6.5}$$

Given the orthogonality of H and V components, $y(t) \propto |g_H(t)|^2 + |g_V(t)|^2 = |x(t)|^2$, meaning that the received signal is ideally the same of a standard IM/DD communication system. The received signal is then [78]:

$$y(t) \propto 1 + \cos\left(\frac{\pi V_{bias}}{V_\pi}\right) - \pi \frac{s(t)}{V_\pi} \sin\left(\frac{\pi V_{bias}}{V_\pi}\right), \tag{6.6}$$

and from that the information carried by $s(t)$ is straightforwardly extracted.

6.3.4 Received 2-PolSK Stream

To retrieve the parallel stream $b(t)$, the transmitted SOP needs to be estimated at the receiver side: this can be done by reading the received power along the two possible linear SOPs. To do that, a PBS aligned to the 45°-135° axes is used to separate the two components (called H' and V') and the difference in received power along H' and V' gives the S_2 parameter on which the binary information is encoded. This can be achieved equivalently with a Faraday rotator giving a 45° polarization rotation followed by a PBS aligned with the defined reference system as in Fig. 6.1. The received power on the horizontal path is

$$\begin{aligned} y_{H'}(t) = |w_{H'}(t)|^2 &= \left|\frac{\sqrt{2}}{2} g_H(t) + \frac{\sqrt{2}}{2} g_V(t)\right|^2 \\ &= |\pm x(t) + x(t)|^2 \\ &= \begin{cases} |x(t)|^2 & \text{if } \varphi = 0 \\ 0 & \text{if } \varphi = \pi \end{cases} \end{aligned}, \tag{6.7}$$

and on the vertical path it is:

$$\begin{aligned} y_{V'}(t) = |w_{V'}(t)|^2 &= \left|-\frac{\sqrt{2}}{2} g_H(t) + \frac{\sqrt{2}}{2} g_V(t)\right|^2 \\ &= |\mp x(t) + x(t)|^2 \\ &= \begin{cases} 0 & \text{if } \varphi = 0 \\ |x(t)|^2 & \text{if } \varphi = \pi \end{cases} \end{aligned}, \tag{6.8}$$

The difference between the received power along the 45° and the 135° linear polarization states gives the S_2 Stoke parameter of the received optical signal:

$$\hat{S}_2 = y_{H'} - y_{V'} = \begin{cases} |x(t)|^2 & \text{if } \varphi = 0 \\ -|x(t)|^2 & \text{if } \varphi = \pi \end{cases} \tag{6.9}$$

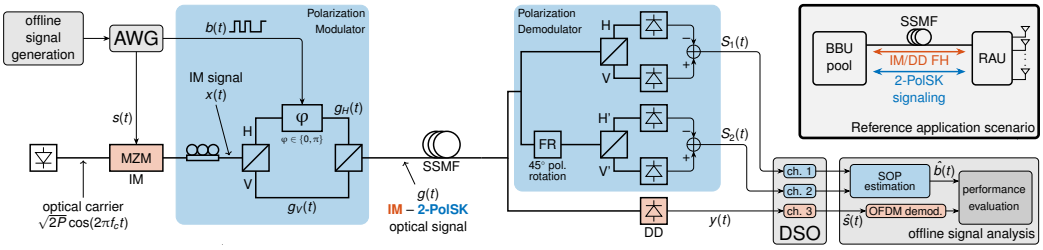

Figure 6.2: Joint intensity-polarization mo-demodulation scheme. The components for the IM/DD channel are in red, those for the parallel 2-PolSK channel are in blue.

The above discussion is valid for an ideal case in which the SOP is not altered in any way during propagation, and perfect devices are employed both at the polarization modulator and demodulator: it is possible that the received lightwave presents a generic elliptical SOP. To give robustness to the SOP estimation, it is then preferable to add the estimation of at least the S_1 parameter of the received lightwave. In this way, any linear SOP can be identified (please notice that the presence of a circularly polarized component results in a reduction of signal power on the 2-PolSK signal).

6.4 Experimental Setup

The experimental setup is intended to provide a proof-of-concept of the proposed system, and it is in Fig. 6.2. Estimation of the S_1 parameter (defined as the difference in received energy along the horizontal and vertical linear polarization states) of the received optical signal is added for robustness against rotation of the binary constellation, which can be caused by propagation, by different path lengths for the H and V paths and/or by imperfect phase shift at the modulator.

The OFDM signal (LTE-like, 20-MHz bandwidth, 64-QAM on each subcarrier) driving the MZM, as well as the binary stream controlling the 2-PolSK, are generated adopting offline processing (Matlab code) and using a Tektronix arbitrary waveform generator (AWG) with 9.6-GHz electrical bandwidth working at 3 GS/s. The bias voltage of the MZM is set to $V_{bias} = 3.5\,V$.

The bit stream transmitted along the PolSK channel is obtained by Manchester encoding of the 1.5-Mbit/s binary signal with a clock signal at 3 MHz. Each semi-period of the clock signal is called chip and 4 chips correspond to one bit duration. Manchester encoding is used to mitigate the effects of the high-pass characteristics of the driver that is needed to interface

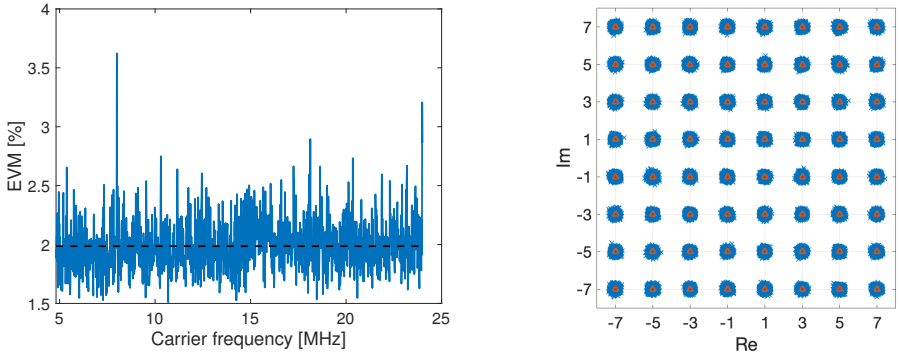

Figure 6.3: EVM versus carrier frequency (left) and total received constellation (right). $V_{bias} = 3.5\,\mathrm{V}$, $P_{rx} = -12\,\mathrm{dBm}$, 25-km fiber link, joint IM–2-PolSK transmission.

the phase modulator within the polarization modulator ($V_\pi = 7V$) with the AWG ($V_{p2p} = 1V$), and to properly track the observed constellation rotation as detailed in Section 6.5. Beside that, Manchester encoding can also be envisioned to provide a timing reference to the RAU, superimposed to the binary signaling. The transmitted signals correspond to the duration of 10 OFDM symbols (i.e., 666.66 μs): 10 symbols and 1000 bits are transmitted on the OFDM and 2-PolSK channels respectively. The analyzed received signals from which system performance is assessed correspond to approximately 100 copies of the transmitted signals.

6.5 Experimental Results

After demodulation of the OFDM signal from $y(t)$ in (6.6), system performance is evaluated in terms of error vector magnitude (EVM) on each subcarrier, shown in Fig. 6.3 for a 25-km fiber link and received optical power $P_{rx} = -12$ dBm together with the received symbols on all the subcarriers. Results in average EVM versus received optical power are in Fig. 6.4, showing little EVM degradation when the 2-PolSK channel is active. Such limited degradation is consistent with the additional attenuation, by approximately 9 dB, introduced by the 2-PolSK module.

At the receiver side, the SOP is estimated for every chip and Manchester decoding yields the received bit stream. The received SOPs corresponding to the chip values ± 1 are not constant, as can be seen in Fig. 6.5: the 2-PolSK constellation rotation is a low-pass process with $\sim$1-MHz bandwidth. Manchester encoding with a 3-MHz clock allows then to properly sample

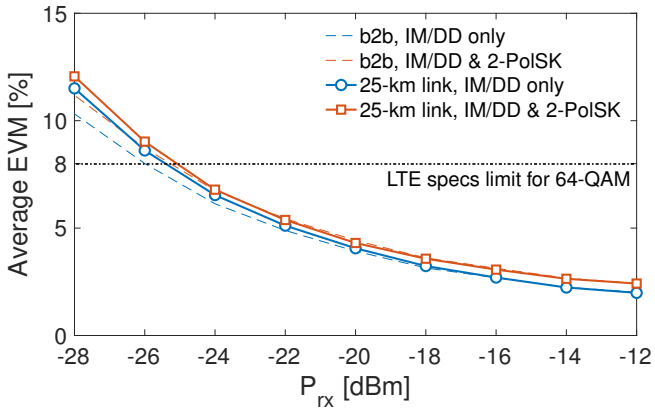

Figure 6.4: Average EVM versus received optical power, with (red lines) or without (blue lines) polarization modulation, back-to-back (dashed lines) or with 25-km fiber link (solid lines). $V_{bias} = 3.5\,\mathrm{V}$.

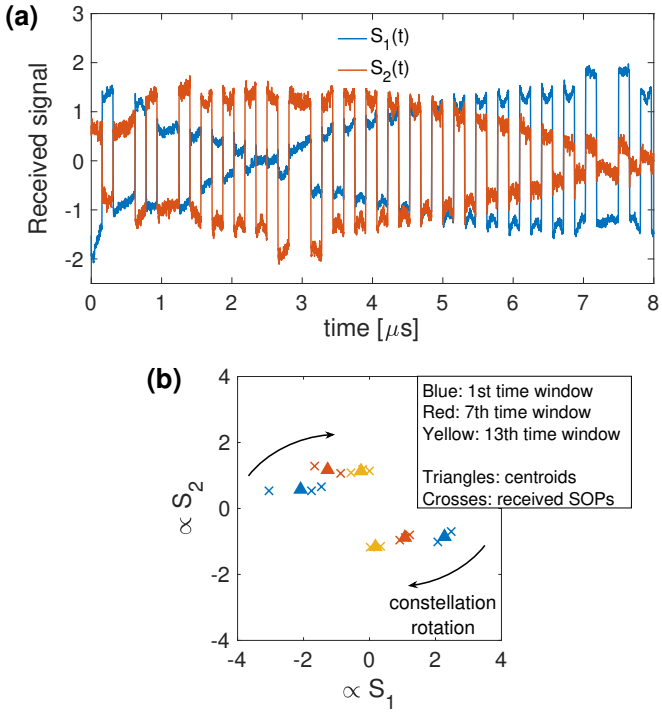

Figure 6.5: Received signal along the S_1 and S_2 receiver paths (a) along with the received SOPs and inferred constellation points for 6-chips windows (b). 25-km fiber link, $P_{rx} = -12\,\mathrm{dBm}$.

and track such SOP rotation. The approach to demodulate the binary signal

is the following: $S_1(t)$ and $S_2(t)$ are averaged within each chip duration to estimate the corresponding (S_1, S_2) point; and within a moving window of 3 chips, the 3 corresponding points on the S_1S_2 plane are clustered around two centroids that are considered to be the constellation points for that window. Since no error is observed in the analyzed received bits ($> 10^5$), system performance for the 2-PolSK channel is assessed in terms of SNR at the decision variable (i.e., the chip values) in Fig. 6.6b, both in b2b and with a 25-km link, either with or without IM/DD modulation of the optical carrier. The obtained SNR values correspond to extremely low error probability for a binary modulation, and would then allow for a higher order PolSK. The effect of IM/DD transmission is to add a noise component to $S_1(t)$ and $S_2(t)$, proportional to the OFDM signal $s(t)$ but limited if not negligible in its impact on the SNR curves of Fig. 6.6 due to averaging of $S_1(t)$ and $S_2(t)$ within the chips.

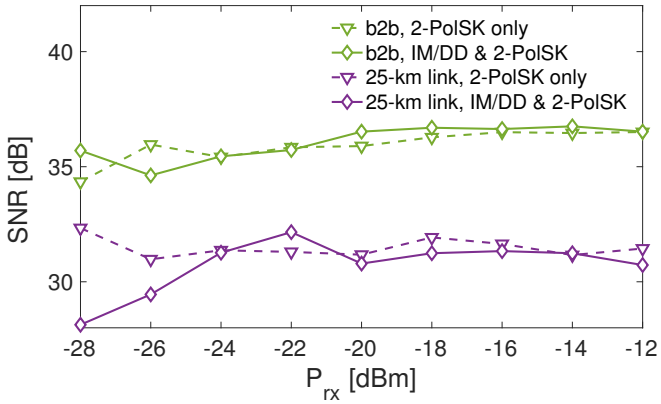

Figure 6.6: Performance evaluation for 2-PolSK signal: SNR at the decision variable (chip) vs received optical power.

6.6 Concluding Remarks

A joint intensity-polarization modulation is proposed to provide a control channel parallel to the A-RoF fronthauling. The 2-PolSK channel is physically separated from the IM/DD, so that its use requires only to add the polarization modulator and demodulator modules, without further update of the FH hardware or software and guaranteeing the cost-effectiveness of this solution. Experimental validation shows a negligible performance degradation of the IM/DD link related to the attenuation introduced by the polarization modulator, thus proving the feasibility of the proposed architecture. The 2-PolSK transmission results to be extremely reliable, offering the possibility of a more complex polarization modulation, i.e., higher bit rates on the PolSK channel.

Chapter 7

Jitter Analysis of Precise Sigma-Delta PWM

Contributions

This Chapter deals with a precise pulse width modulation based on the concept of sigma-delta modulation. In particular, the analysis is on the effect of timing jitter in pulse width modulation. The proposed precise PWM based on the noise-shaping characteristics of $\Sigma\Delta$ loops is shown to be robust against timing inaccuracies.

Organization

The $\Sigma\Delta$-PWM is in Section 7.2. The impact of clock jitter on the system is discussed in Section 7.3 and numerically evaluated in Section 7.4, with a realistic statistical model for clock jitter. Conclusions are in Section 7.5.

7.1 Introduction

Pulse width modulation (PWM) is a modulation technique that maps the amplitude of a signal onto the duration of fixed-amplitude rectangular pulses, which is widely used in the fields of active control [79] and switch mode power amplifiers (class-D and class-E) mainly for energy efficiency that can be greater than 90% [80].

PWM was originally proposed as modulation scheme for communication systems, and in particular PWM is appropriate for those systems impaired by saturation and linearity issues that make amplitude modulation techniques unfeasible, or excessively inefficient. An example application of PWM to

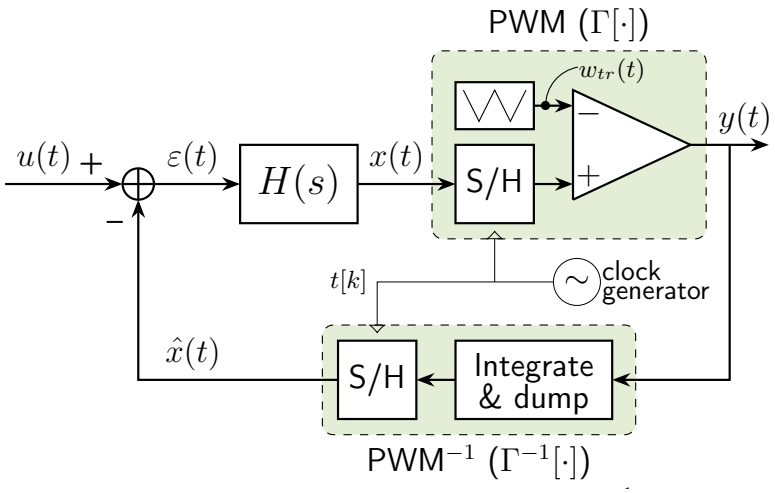

Figure 7.1: Block diagram of continuous-time ΣΔ-PWM.

communication systems is optical PWM, in which the PW-modulated signal drives the optical carrier: PWM was proposed in [15,81] as a novel concept for a functional split to remotize the antenna systems in future generation (5G) radio access network (RAN) deployments, thus enabling the centralized RAN [7]. In particular, the closed-loop PWM architecture called ΣΔ-PWM, further analyzed in this Chapter, was introduced in [81] specifically for optical communication. Recently, PWM has also been considered for visible light communication (VLC) [82], which is an enabling technology for Internet-of-Things (IoT) deployments [83].

Precise and robust PWM is crucial when considering, e.g., control of critical tasks, transmission of low-SNR signals or high-fidelity audio applications of class-D amplifiers (CDAs), where distortion (plus noise) is required to be approximately 70 dB below the signal [84]. Beyond typical audio applications, the use of CDAs has been proposed for power line communication (PLC) [85], thus facing larger signal bandwidth up to 500 kHz. The accuracy requirements on the PWM representation are extremely challenging at high switching frequencies (i.e., at large signal bandwidth), especially in the generation of the reference waveform. In these cases, with reference to class-D amplification, the closed loop used to stabilize the amplifier gain may not be enough to compensate for PWM inaccuracies, hence the need for precise PW modulation inside the loop [85].

Precise PWM is provided by the ΣΔ-PWM, originally proposed in [81] and analyzed here for the effects of clock inaccuracies. The ΣΔ-PWM architecture is represented in Fig. 7.1, and it is based on the noise-shaping concept of ΣΔ modulation that is widely adopted for high-resolution ana-

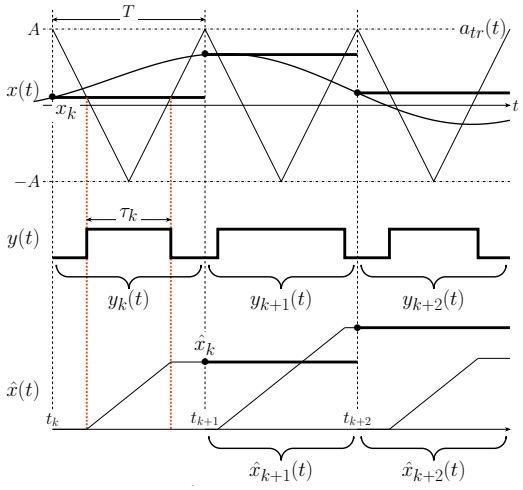

Figure 7.2: Example of signals in the continuous-time ΣΔ PWM.

log/digital conversion in oversampled ΣΔ-ADCs [86]. Its major benefit is the noise shaping capability, which depends on the oversampling ratio and on the loop filter $H(s)$. The PW modulator is a non-linearity in the forward path that encodes the filtered error signal $x(t)$ onto the output $y(t)$, and its inverse (PWM^{-1}) gives a feedback signal $\hat{x}(t)$ of appropriate form. In ΣΔ-ADC the nonlinearities are the internal low-resolution analog-to-digital (ADC) and digital-to-analog (DAC) converters, respectively, and conceptually pairing ΣΔ-PWM with ΣΔ-ADC is beneficial for analytic treatment even if their output signals are totally different.

PWM and ΣΔ modulation have been associated in the past (e.g., [87, 88]) to exploit some features of pulse-duration modulation to solve some issues in analog/digital conversion, or to use ΣΔ-ADC for high-precision digital conversion before digital PWM. Conversely, in the all-analog system described in this Chapter no digitization is involved: the interest is to exploit the ΣΔ theory to obtain an accurate PW representation of analog signals with a closed-loop system to mitigate PWM errors. The design/analysis tools for continuous-time (CT) ΣΔ-ADC can be readily adapted to the proposed ΣΔ-PWM.

7.2 Continuous-Time Sigma-Delta PWM

The ΣΔ-PWM in Fig. 7.1 is conceived as a ΣΔ loop where PW modulation and demodulation are performed on forward and feedback paths, respectively. There are two main approaches to both PW modulation and

demodulation [39]: uniform or natural sampling in PW modulation, and low-pass filtering (LPF) or integrate&dump (I&D) in PW demodulation to provide pulse-width to amplitude conversion (PWM^{-1}). Distortion-free modemodulation is obtained either through uniform sampling PWM and I&D demodulation, or with natural sampling PWM paired with LPF [16,39]. The choice of the specific PW (de)modulation to be used in the $\Sigma\Delta$-PWM loop is a free design parameter, uniform sampling and I&D are the configurations adopted throughout the Chapter for analytical convenience, for conceptual equivalence with $\Sigma\Delta$-ADC, and for power efficiency [89].

The signals involved in the $\Sigma\Delta$-PWM of Fig. 7.1 are represented in Fig. 7.2. The prediction error $\varepsilon(t)$ is filtered by $H(s)$ to give $x(t)$, which is then encoded into a PWM waveform $y(t)$ after sampling-and-hold (S/H) so that the continuous-time signal $y(t)$ carries information about the (discrete-time) PW. This is obtained as $\tau_k = \Gamma[x_k]$ through the comparison of the sampled-and-held signal with a triangular wave of period T and amplitude A as in Fig. 7.2:

$$y(t) = \sum_{k=-\infty}^{+\infty} y_k(t) = \sum_{k=-\infty}^{+\infty} \text{rect}\left(\frac{t - t_k - T/2}{\tau_k}\right) \tag{7.1}$$

where $y_k(t)$ is the width-modulated pulse at the k-th time interval, $t_k = kT$, T is the sampling period and the ideal amplitude-duration mapping is

$$\tau_k = \Gamma[x_k] = \left(\frac{x_k}{A} + 1\right)\frac{T}{2}\,, \tag{7.2}$$

as can be obtained from Fig. 7.2. The filtered error signal $x(t)$ is uniformly sampled at a frequency $f_s = 1/T = \text{OSR} \cdot 2B$ chosen according to the signal bandwidth B and to the oversampling ratio $\text{OSR} = f_s/2B \geq 1$. PW demodulation on the feedback branch estimates $\hat{x}(t)$ to be subtracted to the input signal $u(t)$. The PWM signal $y(t)$ is demodulated by an integrator that is periodically reset at the end of each sampling period T and maintained by a S/H circuit: $\hat{x}(t) = \sum_{k=-\infty}^{+\infty} \hat{x}_k(t)$ is a sequence of non-return-to-zero (NRZ) waveforms

$$\hat{x}\,(t) = \sum_{k=-\infty}^{+\infty} \Gamma^{-1}[\tau_{k-1}]\text{rect}\left(\frac{t - t_k - T/2}{T}\right)\,, \tag{7.3}$$

and, in the closed loop, $\hat{x}\,(t)$ acts as a feedback prediction of the input signal $u(t)$ after a delay of T.

Differently from $\Sigma\Delta$-ADC where the internal conversions (A/D and D/A) are ideally instantaneous, here PW-demodulation introduces a delay T and

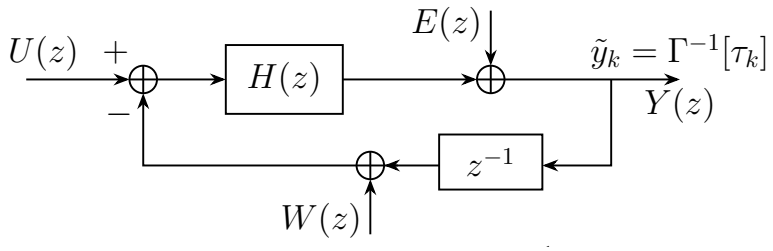

Figure 7.3: Linear model of ΣΔ-PWM.

the feedback signal takes the value $\hat{x}_k$ (estimate of the sample $x_k = x(kT)$) in the interval $t \in [(k+1)T, (k+2)T)$ as shown in Fig. 7.2 and this feedback delay needs to be taken into account in the design of the ΣΔ-PWM.

Overall, the effect of ΣΔ-PWM is that the continuous-time amplitude signal $u(t)$ is mapped onto $y(t)$, carrying information about the discrete-time duration signal $\tau[k]$. It is therefore non-trivial to precisely define the system transfer functions as information is encoded either on amplitude or on time duration of either continuous or discrete-time signals.

As in CT-ΣΔ-ADC, system analysis can be carried out in the discrete-time domain assuming that the input signal is sampled before entering the loop. Any DT-to-CT conversion can then be used to obtain the equivalent CT system [90]. In this Chapter, an amplitude equivalent of the output PW sequence $\tau[k]$ is obtained through ideal duration-to-amplitude mapping. This is to obtain the linearized discrete-time model of ΣΔ-PWM of Fig. 7.3 in which only discrete-time, amplitude signals are involved. The model includes the delay introduced by the feedback PW demodulator and the terms $E(z)$, $W(z)$ account for any imprecision (noise) introduced by the inner PW modulator and demodulator, respectively.

From this model, a system description in terms of signal and noise transfer functions can be obtained. The two transfer functions, respectively for input (signal transfer function, STF) and error (noise transfer function, NTF), are [90]:

$$\mathrm{STF}(z) = \frac{Y(z)}{U(z)} = \frac{H(z)}{1 + H(z)z^{-1}} \tag{7.4}$$

$$\mathrm{NTF}(z) = \frac{Y(z)}{E(z)} = \frac{1}{1 + H(z)z^{-1}} \tag{7.5}$$

where $E(z)$ is the $\mathcal{Z}$-transform of any PW error $e[k]$ introduced at the PWM. Please notice that, for the continuous-time system, the STF is a mixture of s-domain and z-domain transfer functions, omitted here for the sake of simplicity. The loop filter $H(z)$ is designed for noise reduction

(NTF), avoiding signal distortion (STF should be flat within signal bandwidth). For example, if $H(z)$ is chosen to be the first-order integrator $H_1(z) = 1/\left(1 - z^{-1}\right)$, then $\mathrm{NTF}_1(z) = 1 - z^{-1}$, and the subscript specifies the order of the loop. The noise shaping capability of the loop is apparent from the NTF, since in the frequency domain its square modulus is $|\mathrm{NTF}_1(f)|^2 = (2\sin(\pi f T))^2$. Higher-order noise shaping characteristics are obtained adding additional feedback paths and integrators. The NTF for an ℓ-th order loop is $\mathrm{NTF}_\ell(z) = (1 - z^{-1})^\ell$.

7.3 Clock Jitter In Sigma-Delta PWM

Time jitter is any deviation from true periodicity in clock signals, and it can be modeled as a stochastic time process $\delta t[k]$ additive to the sequence of sampling instants kT:

$$t[k] = kT + \delta t[k] \; . \tag{7.6}$$

In the $\Sigma\Delta$-PWM architecture at hand, the clocked components that are affected by timing jitter are both the PW modulator and demodulator as detailed in Sections 7.3.2 and 7.3.3. In particular, while the jitter error at the PWM is shaped by the system NTF, timing inaccuracies on the feedback demodulator introduce in-band noise. It is however to be noticed that, possibly, a practical implementation of the $\Sigma\Delta$-PWM would include natural sampling PWM paired with LPF demodulation, thus limiting the impact of jitter to the PWM inside the loop. In the following section the jitter-induced error at the PWM is labeled as $e\,[k]$ and its noise-shaped version at the output is $q[k]$. The jitter noise at the feedback PW demodulator is $w\,[k]$ and the overall noise component at the output of the $\Sigma\Delta$-PWM is $n\,[k] = q\,[k] + w\,[k]$ as detailed below.

7.3.1 Clock Jitter Model

Before any analysis, an accurate review of typical clock jitter is mandatory. Even if the assumption of white, Gaussian jitter noise $\delta t[k]$ is common [91], it does not consider the real nature of clock signals that are wide-sense stationary with a strong correlation among the samples $\delta t[k]$. Considering a first-order phase-locked loop (PLL) for timing generation, the power spectral density (PSD) $S_{\delta t}(\omega)$ of the jitter process can be modeled as Lorentzian [92]:

$$S_{\delta t}(\omega) = \frac{2\sigma_{\delta t}^2}{\omega_{\mathrm{PLL}}} \cdot \frac{\omega_{\mathrm{PLL}}^2}{\omega_{\mathrm{PLL}}^2 + \omega^2} \tag{7.7}$$

where $\sigma_{\delta t}$ is the root-mean-square value of the sequence $\delta t[k]$ and ω_{PLL} is the -3dB-bandwidth of the PLL. The model in (7.7) gives a -20 dB/dec slope outside the PLL bandwidth, while steeper slopes can be obtained using higher order PLLs.

7.3.2 PWM Errors from Timing Inaccuracies

Errors on the clock signal produce a distortion of the amplitude-to-width mapping (7.2) provided by the PW modulator via comparison with a triangular wave $a_{tr}(t)$. Let us assume that $a_{tr}(t)$ is generated by a square wave generator followed by an integrator: clock jitter affects the square wave only in the timing of its edges and not in its amplitudes, the slopes of the triangular wave are not affected. The sample value of the triangular wave at $t_n = nT/2$, nominally $\pm A$, is, in presence of clock jitter,

$$a_{tr}(t_n) = (-1)^n A + \frac{8A}{T} \sum_{i=-\infty}^{n} (-1)^i \delta t_i \tag{7.8}$$

where δt_i is the jitter process sampled at $t_i = i \cdot T/2$, corresponding to the edges of the square wave. The summation in (7.8) is the integral of a (discrete-time) signal obtained as modulation of a Nyquist-rate sinusoid with the jitter process. Integration in the time domain corresponds to a multiplication by $1/j2\pi f$ in frequency, and the summation in (7.8) is equivalent to sampling the signal after integration. Since the jitter process is narrowband, the multiplicative factor due to integration can be approximated as constant inside the band of interest and

$$a_{tr}(t_n) \simeq (-1)^n A + \frac{4A}{T} (-1)^n \delta t_n \tag{7.9}$$

where the scaling factor is $1/2$ since the sinusoid is at the Nyquist frequency. Ultimately, jitter generates an amplitude modulation of the triangular waveform: with the assumption of narrowband clock jitter, the amplitude of the reference triangular waveform at the k-th time period is $A_k = A + \delta A_k$ rather than A, where

$$\delta A_k \simeq \frac{4A}{T} \delta t_k \, . \tag{7.10}$$

The resulting distorted amplitude-duration mapping is

$$\tau_k = \left(\frac{x_k}{A_k} + 1 \right) \frac{T_k}{2} \tag{7.11}$$

where $T_k = T + \delta t_{k+1} - \delta t_k$ is the true duration of the sampling interval. Due to the narrow bandwidth of the jitter process δt, the perturbation of the sampling interval is negligible with respect to the amplitude modulation of the triangular waveform, so that $T_k \simeq T$. The duration error resulting from (7.11) with respect to the ideal PW τ'_k obtained from (7.2) is:

$$\Delta\tau_k = \tau_k - \tau'_k \simeq -\frac{x_k \delta A_k}{2A(A + \delta A_k)} T \,. \tag{7.12}$$

As stated in Section 7.2, we are analyzing the whole system as if the information content is always encoded onto amplitude values. The duration error is therefore considered by means of an equivalent amplitude error with respect to the ideal duration-to-amplitude mapping ($\hat{x}_k = (2A/T)\tau_k - A$):

$$e_k = \hat{x}_k - \hat{x}'_k = \Delta\tau_k \frac{2A}{T} \simeq -x_k \frac{\delta A_k}{A} \tag{7.13}$$

where $\hat{x}'_k$ is the amplitude corresponding to the ideal PW τ'_k and jitter is smaller than τ'_k, and thus $|\delta A_k| \ll A$. Notice that the error (7.13) depends on the sample x_k and on the amplitude fluctuation δA_k as in Fig. 7.4.

Again thanks to the narrowband characteristics of δt, the additive error in (7.13) is approximately a scaled version of $x[k]$. In terms of power spectral density, the scaling factor is given by the power of $\delta A\,[k]$: the resulting open-loop signal to (jitter) noise ratio $\gamma_{j,0}$, defined as the ratio between the power of $x\,[k]$ and of $e\,[k]$, is

$$\gamma_{j,0} \simeq \left[\frac{16}{T^2} \cdot \frac{1}{2\pi} \int_{-\pi}^{\pi} S_{\delta t}(\omega) d\omega \right]^{-1} \tag{7.14}$$

and $S_e\,(f) \simeq S_x\,(f) \cdot \gamma_{j,0}^{-1}$, where $S_x\,(f)$ is the PSD of $x\,[k]$.

The jitter-induced noise at the PWM is shaped by the NTF of the system: denoted as $S_e\,(f)$ the PSD of the error $e\,[k]$ at the PW modulator inside the loop and as $S_{q,\ell}\,(f)$ the PSD of the error at the output of a ℓ^{th}-order $\Sigma\Delta$-PWM, it is $S_{q,\ell}(f) = S_e(f) \cdot (2\sin(\pi f T))^{2\ell}$.

Let us define $\xi = \frac{\pi}{\mathrm{OSR}}$, and consider the SNR $\gamma_{j,\ell}$ at the output of an ℓ^{th}-order loop considering the jitter noise at the PWM only. For a 1^{st} order $\Sigma\Delta$-PWM, from integration of $S_{q,1}\,(f)$ within the signal bandwidth, it is approximately

$$\gamma_{j,1} = \gamma_{j,0} \cdot \left[2\,(1 - \mathrm{sinc}\,(\xi))\right]^{-1} \tag{7.15}$$

and similar expressions for higher order loops can be straightforwardly defined.

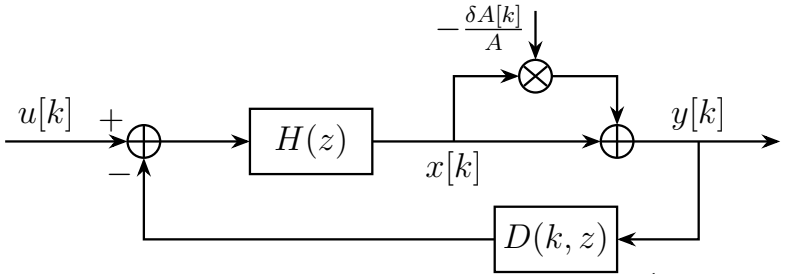

Figure 7.4: Complete jitter noise model for ΣΔ-PWM.

7.3.3 Jitter Effects on Feedback Demodulator

Let us now consider jitter noise at the feedback demodulator, which introduces a phase modulation of the feedback waveform. Such feedback signal $\hat{x}(t)$ is, in ΣΔ-PWM, conceptually similar to the one of ΣΔ-ADC as it is a sequence of NRZ waveforms. The analytical approach developed for feedback DAC jitter in CT ΣΔ-ADC can then be readily adapted here, and jitter noise at the feedback demodulator can be absorbed as an amplitude modulation of $\hat{x}(t)$, modeled as a signal-dependent additive noise [93]:

$$w_k = \frac{\delta t_k}{T} \cdot (y_k - y_{k-1}) \tag{7.16}$$

with the difference from ΣΔ-ADC that in ΣΔ-PWM the values of $y[k]$ are not quantized. Due to the low-pass characteristics of δt, the resulting error PSD $S_w(f)$ is a scaled version of the PSD of the signal derivative, where the scaling factor is given by the power of the jitter process. The noise component in (7.16) is seen at the output as filtered by the STF, hence $w[k]$ is an additive noise to the output signal $y[k]$, independent of the loop order.

The model in (7.16), albeit accurate in the statistical description of $w[k]$, does not consider negative values of $\delta t[k]$ and the resulting inter-sample interference from y_{k+1}. To take that into account, $w[k]$ is simulated in Section 7.4 by considering, instead of z^{-1}, a time-variant feedback filter $D(k,z)$:

$$\begin{aligned} D(k,z) = {} & |\delta t_{k+1}|\, h(-\delta t_{k+1}) \\ & + (1 - |\delta t_{k+1}|\, h(-\delta t_{k+1}) - |\delta t_k|\, h(\delta t_k))z^{-1} \\ & + |\delta t_k|\, h(\delta t_k) z^{-2} \end{aligned} \tag{7.17}$$

where $h(\cdot)$ is the Heaviside step function: the first and third terms (z^0 and z^{-2}) accounts for the inter-sample interference above mentioned, which occurs only when the actual transition times belong to the sampling interval,

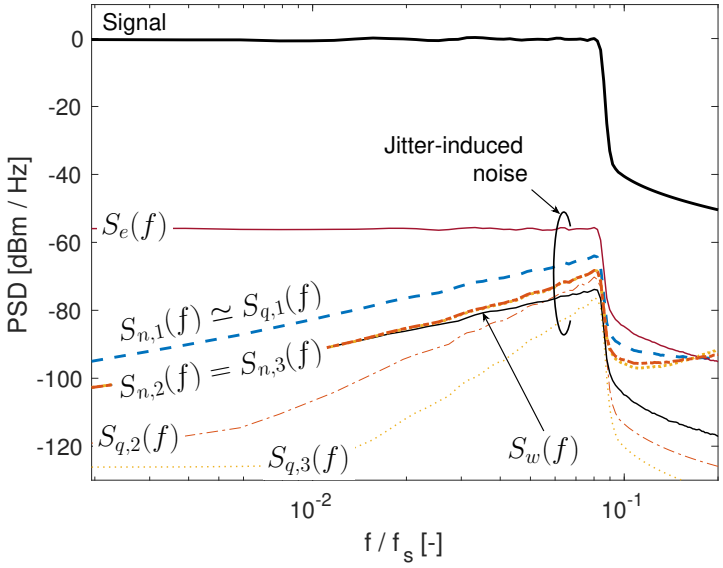

Figure 7.5: PSD of signal and of jitter-induced noise at the output of the ΣΔ-PWM. $S_{n,\ell}(f)$ indicates the overall noise at the output of the ΣΔ-PWM, $S_w(f)$ is the jitter noise due to the feedback PWM^{-1} alone, while $S_{q,\ell}(f)$ is the jitter noise introduced by the PWM and filtered by the loop. $\ell \in \{1, 2, 3\}$ is the order of the loop. $\sigma_{\delta t}/T = 10^{-3}$ and OSR $= 6$.

i.e., when $t_k = kT + \delta t_k > kT$ and/or $t_{k+1} = (k+1)T + \delta t_{k+1} < (k+1)T$. The overall jitter model for the ΣΔ-PWM is in Fig. 7.4, including the contributions of the PW modulator and demodulator.

7.4 Numerical Results

Let us consider the case of a baseband input signal $u(t)$, bandlimited to B and with constant PSD within its bandwidth. The system is affected by jitter noise, modeled as in Section 7.3.1 with realistic values for ω_{PLL} and $\sigma_{\delta t}$ taken from [94,95] considering a 100-MHz signal bandwidth: the normalized PLL bandwidth is $\omega_{\text{PLL}}/2\pi f_s = 10^{-4}$. Numerical simulations are performed to validate the analytical model for system design, and to evaluate the performance degradation introduced by clock jitter.

The PSDs of the signal and the jitter-induced error components are in Fig. 7.5. $S_e(f)$ is the PSD of the PWM error in (7.13) and $S_{q,\ell}(f)$ (for $\ell = 1, 2, 3$) is its noise-shaped version for 1^{st}, 2^{nd} and 3^{rd} order modulators with OSR $= 6$ and $\sigma_{\delta t}/T = 10^{-3}$. $S_w(f)$ is the jitter-induced noise PSD at

the feedback demodulator and $S_{n,\ell}(f)$ is the total noise PSD at the output of an ℓ-th order loop.

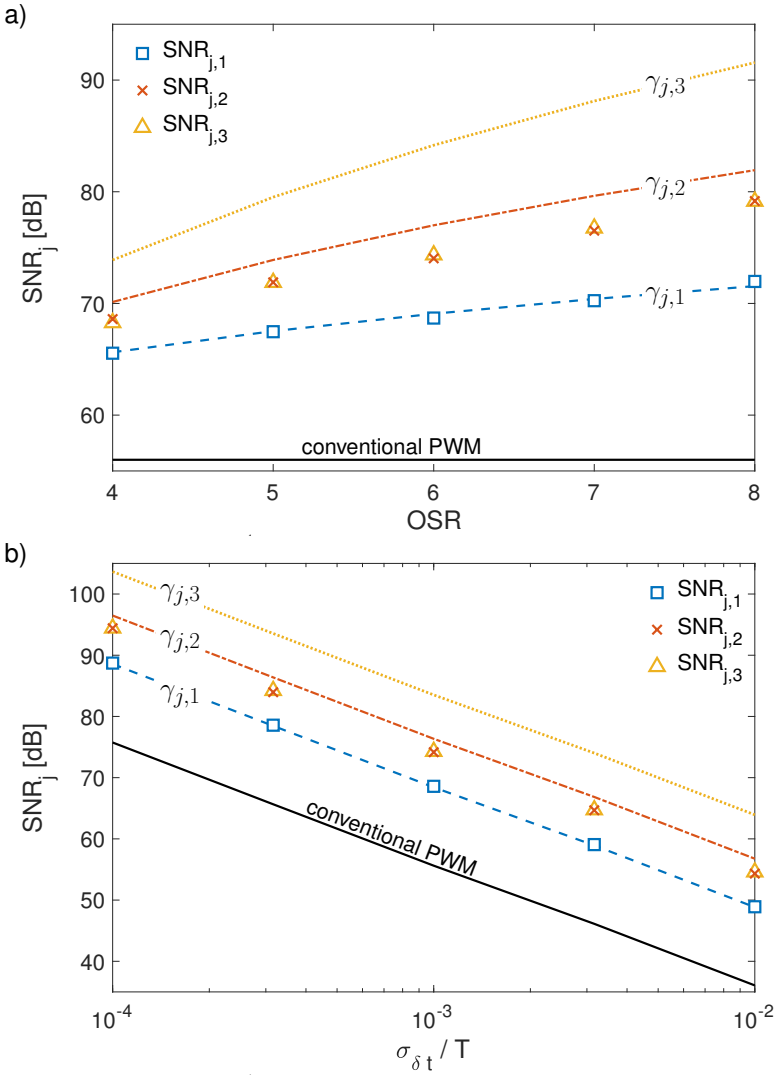

Figure 7.6: SNR_j vs OSR @ $\sigma_{\delta t} = 10^{-3}T$ (a) and SNR_j vs $\sigma_{\delta t}$ @ OSR $= 6$ (b): only jitter at the PW modulator (lines) and complete jitter model (markers) for 1^{st} (blue, dashed lines, square markers), 2^{nd} (red, dash-dots, crosses) and 3^{rd} order (yellow, dotted lines and triangles) loop, compared to the conventional PWM.

$S_e(f)$ is well approximated by a scaled version of the signal PSD: in the settings stated above, it results to be around 56 dB below the signal PSD, consistently with $\gamma_{j,0}$ in (7.14). Timing inaccuracies at the feedback PW demodulator give an output error which is, as expected, independent of the

loop order and shaped as the signal derivative. For a first-order loop the dominant noise component is related to the PW modulator, for higher order loops this component is attenuated enough for the feedback jitter component to prevail.

To have a more thorough analysis of system performance, the mean signal to (jitter) noise ratio ($\mathrm{SNR}_{j,\ell}$) within signal bandwidth is evaluated through numerical integration of the signal and error PSDs with the same input signal of Fig. 7.5. $\mathrm{SNR}_{j,\ell}$ is assessed for 1^{st}, 2^{nd} and 3^{rd} order loop versus OSR in Fig. 7.6a and versus clock precision ($\sigma_{\delta t}$) in Fig. 7.6b. The lines labeled with $\gamma_{j,\ell}$ represent the contribution of the jitter at the PW modulator alone, while the markers represent $\mathrm{SNR}_{j,\ell}$, which takes into account also the effect of jitter on the feedback demodulator.

The effect of clock inaccuracies on the feedback path almost vanishes the advantage of having $\Sigma\Delta$-PWM of order higher then two, due to the introduction of in-band noise. Ultimately, achieving the desired performance in terms of SNR_j is a matter of trade-off between architectural complexity ($\Sigma\Delta$ order, 1^{st} or 2^{nd}), sampling rate (OSR and signal bandwidth) and clock precision ($\sigma_{\delta t}$).

In a realistic scenario ($B = 100$ MHz, OSR $= 6$, $\sigma_{\delta t}/T = 10^{-3}$) $\mathrm{SNR}_j = 56$ dB for a conventional PW modulator, to be compared with $\mathrm{SNR}_{j,1} = 69$ dB, $\mathrm{SNR}_{j,2} = \mathrm{SNR}_{j,3} = 74$ dB of a first, second and third order $\Sigma\Delta$-PWM respectively.

7.5 Concluding Remarks

A closed-loop $\Sigma\Delta$-PWM has been proposed, relying on oversampling and on a noise-shaping feedback loop architecture to provide precise analog pulse width modulation. The $\Sigma\Delta$-PWM modulator guarantees improved robustness against jitter with respect to a conventional PW modulator, at the price of some increase in architectural complexity that in some settings can be tolerated in exchange for increasing power efficiency that can be evaluated (not covered here) for any specific circuit implementation. The gain with respect to conventional PWM is analytically derived, and the effectiveness of the $\Sigma\Delta$-PWM modulator is validated through numerical simulations: in reasonable settings the achieved SNR_j is well above 70 dB, compared to the 56 dB of the conventional PWM.

Chapter 8

Conclusions

The Thesis tackled several issues arising from the ongoing evolution of the radio access networks, dealing with analog fronthauling and efficient multiplexing of fronthaul signals, the split of hybrid beamforming for the millimeter waves radio access and broadband analog optical signal processing, and with signaling to enable the tuning of the analog beamformer.

In particular, optical analog pulse width modulation is proposed to achieve the combined advantages of a 2-levels fronthaul signal as in digital radio-over-fiber and of bandwidth-efficient analog communication. A reflective passive optical network is proposed for transmitting PWM signals, and experimental validation proves its effectiveness in the transport of RF signals with 100-MHz bandwidth through up to 20km of fiber link. Multilevel pulse width modulation allows to effectively transmit up to 16 aggregated 20-MHz LTE-like signals through a 7.5-km conventional PON link.

Mode division multiplexing provides an additional spatial dimension for multiplexing of optical fronthaul signals. All-optical passive multiplexers and demultiplexers, either based on photonic lanterns or on multiplane light converters, together with direct detection, provide a cost-effective mean for multimodal transmission. System performance is evaluated considering beamforming at the centralized baseband unit to spatially separate uplink signals coming from users on the scene. The arising intermodal interference on the fronthaul link is shown to be successfully managed by an appropriate association between the space-frequency resource of the radio channel (where the space dimension is defined by the antenna elements of the array) and those of the optical fronthaul (the space dimension being defined by the propagation mode).

When considering the millimeter wave spectrum above 28 GHz for the radio access networks, the mandatory hybrid beamforming processing is proposed to be efficiently split between analog filtering at the remote anten-

nas and digital beamforming at the centralized baseband unit, with analog fronthauling inbetween. This allows to unify the advantages of hybrid BF (energy efficiency and hardware complexity) and of analog FH (bandwidth efficiency), with further compression of the FH communication. Moreover, analog optical processing allows for wideband processing at the antenna units. Tunability of typical optical components is addressed in the context of 5G NR specifications: on the one hand adaptive optical analog beamforming is shown to be mandatory to approach the performance of benchmark all-digital processing, and on the other hand the necessity to compensate for limited tunability speed of optical components is highlighted. Solutions based on digital precompensation and appropriate users scheduling are proposed and validated.

The necessity of adaptive processing at the antenna units increases the complexity of the fronthaul connection between remote antennas and centralized baseband units, due to the need for a signaling channel. Binary polarization modulation is proposed for that, and experimental validation provides a proof-of-concept, with parallel transmission of a LTE-like 20-MHz signal via intensity modulation and of a 1.5-Mbit/s stream via binary polarization shift keying. Results show a negligible degradation in the performance of the IM/DD link carrying the fronthaul signal and a high reliability of the digital signaling.

Last but not least, a precise pulse width modulation based on the concept of sigma-delta modulation is proposed and analyzed for its robustness against clock jitter noise. Results show a gain in signal to (jitter) noise ratio by at least 15 dB with respect to the open-loop pulse width modulation, and the convenience of low pass filtering for pulse width demodulation in the feedback path for achieving even better performance.

Future Directions

Apart from the research interest, technological solutions need to face the reality of market, and in particular the reluctance of vendors to implement non-standard approaches. This is why I don't envision a massive use of analog fronthauling, but rather its application to proprietary solutions for specific target markets. As for the general market, it is my humble opinion that CPRI will evolve towards more efficient transmission schemes, probably based on Ethernet, to give vendors a standardized interface while improving spectrum efficiency on the fronthaul.

The same reasoning holds true for optical signal processing and its application to broadband hybrid beamforming. For a general-purpose vendor, the

advantages of optical signal processing, i.e., the broadband processing, are easily outmatched by the cost of hardware and of development of the system. On the other hand, optical signal processing in analog beamforming is interesting for targeting non-yet-envisioned extremely high-bandwidth communication systems, beyond the 400-MHz channels included in 5G NR. A good example would be a multi-operator network infrastructure, and given the present way of developing operator-specific infrastructure, this makes optical signal processing a research subject for which the market is still not ready. Another point is that optical signal processing for analog beamforming inevitably calls for interdisciplinary knowledge of optical and wireless environments.

Advanced PWM systems for transport of wideband RF signals require an excessive electronics bandwidth, especially at the comparator between signal and triangular reference. It is still open, however, the possibility of application of the precise PWM to more narrowband contexts, such as audio applications.

Bibliography

[1] C. Mobile, "C-RAN: the road towards green RAN," *White Paper*, 2011.

[2] A. Checko et al., "Cloud RAN for Mobile Networks – A Technology Overview," in *IEEE Communications Surveys & Tutorials*, vol. 17, March 2015.

[3] "OBSAI Specification," 2013. Available at www.obsai.com.

[4] "CPRI Specifications V.6.1 (2014-07-01)," September 2014.

[5] A. Pizzinat, P. Chanclou, F. Saliou, and T. Diallo, "Things You Should Know About Fronthaul," *Journal of Lightwave Technology*, vol. 33, no. 5, pp. 1077–1083, 2015.

[6] P. Chanclou et al., "Optical Fiber Solution for Mobile Fronthaul to Achieve Cloud Radio Access Network," in *IEEE FNMS*, (Lisboa), July 2013.

[7] P. Rost *et al.*, "Cloud Technologies for Flexible 5G Radio Access Networks," *IEEE Commun. Mag.*, vol. 52, no. 5, pp. 68–76, 2014.

[8] "eCPRI Specification V1.0 (2017-08-22)," August 2017.

[9] D. Wake *et al.*, "Radio over fiber for mobile communications," in *MWP 2004*, pp. 157–160, IEEE, 2004.

[10] D.Wake *et al.*, "Radio Over Fiber Link Design for Next Generation Wireless Systems," *IEEE/OSA J. Lightw. Technol.*, vol. 28, no. 16, pp. 2456–2464, 2010.

[11] N. J. Gomes *et al.*, "The New Flexible Mobile Fronthaul: Digital or Analog, or Both?," in *ICTON 2016*, pp. 1–4, IEEE, 2016.

[12] T. Kanesan et al., "Impact of optical modulators in LTE RoF system with nonlinear compensator for enhanced power budget," in *OFC*, 2013.

[13] A. Van De Grijp et al., "Novel electro-optical feedback technique for noise and distorsion reduction in high-quality analogue optical transmission of video signals," *Electronics Letters*, vol. 17, no. 11, pp. 361–362, 1981.

[14] B. Wilson and Z. Gassemlooy, "Optical fiber transmission of multiplexed video signals using pulse-width modulation," *Journal of Optoelectronics*, vol. 4, no. 1, pp. 3–17, 1989.

[15] L. Combi *et al.*, "Pulse-Width optical modulation for CRAN fronthauling," in *IEEE GLOBECOM Workshops*, (San Diego), Dec. 2015.

[16] Z. Song and D. V. Sarwate, "The frequency spectrum of pulse width modulated signals," *Signal Processing*, vol. 83, no. 10, pp. 2227–2258, 2003.

[17] Y. Chen *et al.*, "Cost effective wavelength reused MDM system for bidirectional mobile fronthaul," *Optics Express*, vol. 24, no. 20, pp. 22413–22422, 2016.

[18] T. S. Rappaport *et al.*, "Millimeter Wave Mobile Communications for 5G Cellular: It Will Work!," *IEEE Access*, vol. 1, pp. 335–349, 2013.

[19] R. W. Heath *et al.*, "An Overview of Signal Processing Techniques for Millimeter Wave MIMO Systems," *IEEE J. Sel. Topics Signal Process.*, vol. 10, no. 3, pp. 436–453, 2016.

[20] O. El Ayach *et al.*, "Spatially Sparse Precoding in Millimeter Wave MIMO Systems," *IEEE Trans. Wireless Commun.*, vol. 13, no. 3, pp. 1499–1513, 2014.

[21] A. Meijerink *et al.*, "Novel Ring Resonator-Based Integrated Photonic Beamformer for Broadband Phased Array Receive Antennas Part I: Design and Performance Analysis," *IEEE/OSA J. Lightw. Technol.*, vol. 28, no. 1, pp. 3–18, 2010.

[22] D. W. Prather *et al.*, "Optically Upconverted, Spatially Coherent Phased-Array-Antenna Feed Networks for Beam-Space MIMO in 5G Cellular Communications," *IEEE Trans. Antennas Propag.*, vol. 65, no. 12, pp. 6432–6443, 2017.

[23] S. Benedetto and P. Poggiolini, "Theory of Polarization Shift Keying Modulation," *IEEE Transactions on Communications*, vol. 40, no. 4, pp. 708–721, 1992.

[24] S. Benedetto, R. Gaudino, and P. Poggiolini, "Direct detection of optical digital transmission based on polarization shift keying modulation," *IEEE Journal on Selected areas in Communications*, vol. 13, no. 3, pp. 531–542, 1995.

[25] L. Combi, A. Gatto, M. Martinelli, P. Parolari, and U. Spagnolini, "PWM fronthauling in reflective PON," in *2016 European Conference on Networks and Communications (EuCNC)*, pp. 260–264, IEEE, 2016.

[26] A. Gatto, P. Boffi, L. Combi, P. Parolari, U. Spagnolini, R. Brenot, and M. Martinelli, "LTE-A mobile fronthaul exploiting pulse-width modulation in a RSOA-based WDM PON," in *Optical Fiber Communication Conference*, pp. W3C–6, Optical Society of America, 2016.

[27] P. Parolari, A. Gatto, L. Combi, U. Spagnolini, R. Brenot, M. Martinelli, *et al.*, "Pulse width modulation for fronthaul in a broadband-seeded RSOA WDM PON," *IEEE Photon. Technol. Lett.*, vol. 28, no. 15, pp. 1625–1628, 2016.

[28] P. Parolari, A. Gatto, L. Combi, P. Boffi, U. Spagnolini, R. Brenot, and M. Martinelli, "Externally-seeded WDM PON for next generation mobile access based on pulse-width modulation," in *Transparent Optical Networks (ICTON), 2016 18th International Conference on*, pp. 1–4, IEEE, 2016.

[29] P. Parolari, A. Gatto, L. Combi, P. Boffi, M. Martinelli, and U. Spagnolini, "Multilevel pulse width modulation fibre optic transmission for next generation mobile fronthaul," in *ECOC 2016; 42nd European Conference on Optical Communication; Proceedings of*, pp. 1–3, VDE, 2016.

[30] A. Gatto, P. Parolari, L. Combi, U. Spagnolini, R. Brenot, and M. Martinelli, "Fronthaul based on pulse-width modulation in RSOA WDM PONS with broadband and coherent seeds," *Journal of Optical Communications and Networking*, vol. 8, no. 11, pp. B55–B60, 2016.

[31] P. Parolari, A. Gatto, L. Combi, R. Sacchi, R. Giacometti, A. Lena, C. Canziani, and U. Spagnolini, "LTE transmission exploiting pulse width modulation in fibre optic links," in *Transparent Optical Networks (ICTON), 2017 19th International Conference on*, pp. 1–4, IEEE, 2017.

[32] L. Combi *et al.*, "Radio-over-Modes for C-RAN Architecture with Smart Optical Resources Assignment," in *IEEE ICC*, May 2017.

[33] A. Matera, L. Combi, S. H. R. Naqvi, and U. Spagnolini, "Space-frequency to space-frequency for MIMO radio over copper," in *Communications (ICC), 2017 IEEE International Conference on*, pp. 1–6, IEEE, 2017.

[34] L. Combi and U. Spagnolini, "Hybrid beamforming in RoF fronthauling for millimeter-wave radio," in *Networks and Communications (EuCNC), 2017 European Conference on*, pp. 1–5, IEEE, 2017.

[35] L. Combi and U. Spagnolini, "Thermo-Optical Tunable Filtering for Adaptive Hybrid Beamforming in Massive Antenna Arrays," *IEEE Trans. Comm. (submitted to)*.

[36] L. Combi, J. M. Fabrega, M. S. Moreolo, and U. Spagnolini, "Joint Intensity-Polarization Modulation for Signaling in C-RAN Analog Fronthauling," in *IEEE/OSA OFC 2019 (submitted to)*.

[37] L. Combi and U. Spagnolini, "Sigma-Delta Pulse Width Modulator: Jitter Analysis," in *PIMRC 2018*, IEEE, 2018.

[38] J. Bartelt et al., "Fronthaul and Backhaul Requirements of Flexibly Centralized Radio Access Networks," *IEEE Wireless Communications*, Oct. 2015.

[39] H. S. Black, *Modulation theory*. Van Nostrand, 1953.

[40] Chenhui Ye et. al., "A Bidirectional 60-GHz Wireless-Over-Fiber Transport System With Centralized Local Oscillator Service Delivered to Mobile Terminals and Base Stations," *IEEE Photonics Technology Letters*, vol. 24, pp. 1984 – 1987, Nov. 2012.

[41] Evolved Universal Terrestrial Radio Access, "Base Station (BS) Radio Transmission and Reception (Release 10), 3GPP TS 36.104,"

[42] L. Marazzi et al., "Relative intensity noise suppression in reflective SOAs," *Optics Communications*, vol. 318, pp. 186–188, 2014.

[43] J. Gambini and U. Spagnolini, "Wireless over cable for femtocell systems," *IEEE Communications Magazine*, vol. 51, pp. 178–185, May 2013.

[44] H. S. Chung et al., "Design of RoF based Mobile Fronthaul Link with Multi-IF Carrier for LTE/LTE-A Signal Transmission," in *IEEE APMP*, 2014.

[45] S. Berdagué and P. Facq, "Mode division multiplexing in optical fibers," *Applied optics*, vol. 21, no. 11, pp. 1950–1955, 1982.

[46] N. K. Fontaine *et al.*, "30x30 MIMO transmission over 15 spatial modes," in *Optical Fiber Communication Conference Post Deadline Papers*, p. Th5C.1, Optical Society of America, 2015.

[47] N. K. Fontaine *et al.*, "Evaluation of photonic lanterns for lossless mode-multiplexing," in *European Conference and Exhibition on Optical Communication*, pp. Th–2, Optical Society of America, 2012.

[48] J.-F. Morizur *et al.*, "Efficient and mode-selective spatial multiplexer based on multi-plane light conversion," in *Optical Fiber Communication Conference*, pp. W1A–4, Optical Society of America, 2015.

[49] P. Sillard, "Few-mode fibers for space division multiplexing," in *Optical Fiber Communication Conference*, pp. Th1J–1, Optical Society of America, 2016.

[50] D. Yu *et al.*, "Mode-dependent characterization of photonic lanterns," *Optics letters*, vol. 41, no. 10, pp. 2302–2305, 2016.

[51] Velazquez-Benitez *et al.*, "Scaling the fabrication of higher order photonic lanterns using microstructured preforms," 2015.

[52] G. Labroille *et al.*, "Mode selective 10-mode multiplexer based on multi-plane light conversion," in *Optical Fiber Communication Conference*, Optical Society of America, 2016.

[53] S. J. Russell *et al.*, *Artificial intelligence: a modern approach*, vol. 2. Prentice hall Upper Saddle River, 2003.

[54] A. Matera and U. Spagnolini, "Analog MIMO-RoC Downlink with SF2SF," *IEEE Wireless Communications Letters*, pp. 1–1, 2018.

[55] M. K. Samimi *et al.*, "28 ghz millimeter-wave ultrawideband small-scale fading models in wireless channels," in *Vehicular Technology Conference (VTC Spring), 2016 IEEE 83rd*, pp. 1–6, IEEE, 2016.

[56] J. Li *et al.*, *Robust adaptive beamforming*, vol. 88. John Wiley & Sons, 2005.

[57] Y. Liu *et al.*, "Tuning Optimization of Ring Resonator Delays for Integrated Optical Beam Forming Networks," *J. Lightw. Technol.*, vol. 35, no. 22, pp. 4954–4960, 2017.

[58] V. C. Duarte *et al.*, "Photonic true-time-delay beamformer for a phased array antenna receiver based on self-heterodyne detection," *IEEE/OSA J. Lightw. Technol.*, vol. 34, no. 23, pp. 5566–5575, 2016.

[59] A. A. Zaidi *et al.*, "Designing for the future, the 5G NR physical layer," *Ericsson Technology Review*, June 2017.

[60] H. Al-Raweshidy *et al.*, *Radio over Fiber Technologies for Mobile Communications Networks*. Artech House, 2002.

[61] B. Zhu *et al.*, "Seven-core multicore fiber transmissions for passive optical network," *Optics Express*, vol. 18, no. 11, pp. 11117–11122, 2010.

[62] M. Elad, *Sparse and Redundant Representations: From Theory to Applications in Signal and Image Processing*. Springer, 2010.

[63] J.-S. Sheu, "Hybrid Digital and Analogue Beamforming Design for Millimeter Wave Relaying Systems," *J. Commun. and Networks*, vol. 19, no. 5, pp. 461–469, 2017.

[64] H. Boche *et al.*, "A General Duality Theory for Uplink and Downlink Beamforming," in *IEEE VTC*, May 2002.

[65] C. Madsen *et al.*, *Optical Filter Design and Analysis: A Signal Processing Approach*. Wiley, 1999.

[66] N. C. Harris *et al.*, "Efficient, compact and low loss thermo-optic phase shifter in silicon," *Opt. Express*, vol. 22, no. 9, pp. 10487–10493, 2014.

[67] M. Xin *et al.*, "A high speed electro-optic phase shifter based on a polymer-infiltrated P-S-N diode capacitor," *Opt. Express*, vol. 19, no. 15, pp. 14354–14369, 2011.

[68] S. Liu *et al.*, "High speed ultra-broadband amplitude modulators with ultrahigh extinction >65 db," *Opt. Express*, vol. 25, no. 10, pp. 11254–11264, 2017.

[69] A. Liu *et al.*, "A high-speed silicon optical modulator based on a metal-oxide-semiconductor capacitor," *Nature*, vol. 427, 2004.

[70] J. P. Epping, D. Marchenko, A. Leinse, R. Mateman, M. Hoekman, L. Wevers, E. J. Klein, C. G. Roeloffzen, M. Dekkers, and R. G. Heideman, "Ultra-low-power stress-optics modulator for microwave photonics," in *Integrated Optics: Devices, Materials, and Technologies XXI*, vol. 10106, p. 101060F, International Society for Optics and Photonics, 2017.

[71] G. Lenz *et al.*, "Optical Delay Lines Based on Optical Filters," *IEEE J. Quantum Electron.*, vol. 37, no. 4, pp. 525–532, 2001.

[72] J. E. Heebner *et al.*, "Optical Transmission Characteristics of Fiber Ring Resonators," *IEEE J. Quantum Electron.*, vol. 40, no. 6, pp. 726–730, 2004.

[73] M. S. Rasras *et al.*, "Integrated Resonance-Enhanced Variable Optical Delay Lines," *IEEE Photon.Technol. Lett.*, vol. 17, no. 4, pp. 834–836, 2005.

[74] L. Zhuang *et al.*, "Novel ring resonator-based integrated photonic beamformer for broadband phased array receive antennas - Part II: Experimental prototype," *IEEE/OSA J. Lightw. Technol.*, vol. 28, no. 1, pp. 19–31, 2010.

[75] M. R. Watts *et al.*, "Adiabatic thermo-optic mach–zehnder switch," *Optics Letters*, vol. 38, no. 5, pp. 733–735, 2013.

[76] W. M. Green *et al.*, "Hybrid InGaAsP-InP Mach-Zehnder Racetrack Resonator for Thermooptic Switching and Coupling Control," *Opt. Express*, vol. 13, no. 5, pp. 1651–1659, 2005.

[77] D. Richardson, J. Fini, and L. Nelson, "Space-division multiplexing in optical fibres," *Nature Photonics*, vol. 7, no. 5, p. 354, 2013.

[78] J. Leibrich, A. Ali, H. Paul, W. Rosenkranz, and K.-D. Kammeyer, "Impact of Modulator Bias on the OSNR Requirement of Direct-Detection Optical OFDM," *IEEE Photonics Technology Letters*, vol. 21, no. 15, pp. 1033–1035, 2009.

[79] J. Holtz, "Pulsewidth Modulation - A Survey," *IEEE Trans. Ind. Electron.*, vol. 39, no. 5, pp. 410–420, 1992.

[80] C. Pascual *et al.*, "High-Fidelity PWM Inverter for Digital Audio Amplification: Spectral Analysis, Real-Time DSP Implementation, and Result," *IEEE Trans. Power Electron.*, vol. 18, no. 1, pp. 473–485, 2003.

[81] L. Combi and U. Spagnolini, "Sigma-Delta PWM waveforms for optical front-hauling," in *IEEE ICNC*, (Kauai), Feb. 2016.

[82] A. F. Hussein *et al.*, "Visible Light Communications: Toward Multi-Service Waveforms," in *IEEE CCNC*, pp. 1–6, IEEE, 2018.

[83] E. Borgia, "The Internet of Things vision: Key features, applications and open issues," *Computer Communications*, vol. 54, pp. 1–31, 2014.

[84] L. Guo *et al.*, "A 101 dB PSRR, 0.0027% THD+ N and 94% power-efficiency filterless Class D amplifier," *IEEE J. Solid-State Circuits*, vol. 49, no. 11, pp. 2608–2617, 2014.

[85] J. Lu *et al.*, "A CMOS Class-D Line Driver Employing a Phase-Locked Loop Based PWM Generator," *IEEE J. Solid-State Circuits*, vol. 49, no. 3, pp. 729–739, 2014.

[86] P. M. Aziz *et al.*, "An Overview of Sigma-Delta Converters," *IEEE Signal Process. Mag.*, vol. 13, no. 1, pp. 61–84, 1996.

[87] E. Roza, "Analog-to-Digital Conversion via Duty-Cycle Modulation," *IEEE Trans. Circuits Syst. II: Analog Digit. Signal Process.*, vol. 44, no. 11, pp. 907–914, 1997.

[88] Y.-R. Jo *et al.*, "A Low-Noise and Area-Efficient PWM-$\Delta\Sigma$ ADC Using a Single-Slope Quantizer for CMOS Image Sensors," *IEEE Trans. Electron Devices*, vol. 63, no. 1, pp. 168–173, 2016.

[89] R. Polster *et al.*, "A Novel Optical Integrate and Dump Receiver for Clocking Signals," in *NEWCAS*, pp. 1–4, IEEE, 2015.

[90] R. Schreier and G. C. Temes, *Understanding Delta-Sigma Data Converters*. Wiley-Interscience, 2005.

[91] J. A. Cherry and W. M. Snelgrove, "Loop Delay and Jitter in Continuous-Time Delta Sigma Modulators," in *Proc. ISCAS*, pp. 596–599, IEEE, 1998.

[92] M. Clara and N. Da Dalt, "Jitter Noise of Sampled Multitone Signals," *IEEE Trans. Circuits Syst. II: Exp. Briefs*, vol. 58, no. 10, pp. 652–656, 2011.

[93] J. A. Cherry and W. M. Snelgrove, "Clock Jitter and Quantizer Metastability in Continuous-Time Sigma-Delta Modulators," *IEEE Trans. Circuits Syst. II: Analog Digit. Signal Process.*, vol. 46, no. 6, pp. 661 – 676, 1999.

[94] Texas Instruments, "LMK03806 Ultra Low Jitter Clock Generator." Datasheet SNAS522H, Sept. 2011 [revised Aug. 2012].

[95] H. Werker *et al.*, "A 10-GB/s SONET-compliant CMOS transceiver with low crosstalk and intrinsic jitter," *IEEE J. Solid-State Circuits*, vol. 39, no. 12, pp. 2349–2358, 2004.